Doctoral Dissertation
Doctoral Program in Metrology (35th Cycle)

Hybrid Metrology for the Development of Self-Assembled Metamaterials

By

Irdi Murataj

******

Supervisor:
Dr. Federico Ferrarese Lupi

Doctoral Examination Committee:
Dr. Burkhard Beckhoff, Referee, PTB, Berlin, Germany
Dr. Pawel W. Majewski, Referee, University of Warsaw, Poland

Politecnico di Torino
January 10, 2022

Declaration

I hereby declare that, the contents and organization of this dissertation constitute my own original work and does not compromise in any way the rights of third parties, including those relating to the security of personal data.

Irdi Murataj

January 10, 2022

* This dissertation is presented in partial fulfillment of the requirements for **Ph.D. degree** in the Graduate School of Politecnico di Torino (ScuDo).

I would like to dedicate this thesis to my loving family

Acknowledgment

I would like to express my deep gratitude to my supervisor Dr. Federico Ferrarese Lupi for the encouragement and useful critics during this work. I am extremely thankful and indebted for the valuable guidance given to me during the PhD project.

I would also like to acknowledge Prof. Fabrizio C. Pirri, Dr. Luca Boarino and Dr. Natascia De Leo for their support during the work.

I would like to express my deep gratitude to all the people from Istituto Nazionale di ricerca Metrologica (INRiM), in particular Dr. Eleonora Cara and Dr. Angelo Angelini. Thank you very much for your collaboration and support during all my PhD work. It was a pleasure to work with all of you.

I would like to express my deep gratitude also to Dr. Burkhard Beckhoff and his group for hosting me during the research activity at the PTB Bessy II X-Ray Spectroscopy group in Berlin. Special thanks to Dr. Yves Kayser and Dr. Philipp Hönicke for sharing with me their expertise during the fruitful discussions, the guidance, the enthusiastic encouragement and for all the support during my research activity abroad.

A special thank also to Prof. Francesc Perez-Murano, Dr. Miguel Zabala, Dr. Marta Fernández Regúlez from the Institute of Microelectronics of Barcelona IMB-CNM (CSIC) for the support and for sharing with me his expertise in the NFFA European project.

Preface

With the revision of the International System of Units (SI), as approved by the General Conference on Weights and Measures (Conférence générale des poids et mesures [CGPM]) in 2019, units are defined based on fixed, with an exact value, fundamental physical constants. This opened new possibilities for the direct realization of the SI units for any experiment that correlates a measurable quantity to a fundamental constant of nature. In this framework, the recent advances in the generation and manipulation of individual photons have become of great interest for their employment as a primary traceable route to the SI. This is particularly true for emerging quantum technologies, where sources that generate single photons at a known rate can be exploited on the *mise en pratique* for the practical realization of candela (cd) in the SI, as reported by the Consultative Committee for Photometry and Radiometry (CCPR). In this context, nanoplasmonic structures such as hyperbolic metamaterials (HMMs), play a key role on the development of single-photon sources that operate at room temperature, guaranteeing efficient directional and broadband single-photon spontaneous emission enhancement. To date, the intrinsic constrains imposed by conventional lithographic and material deposition/growth techniques, limit the fabrication of HMMs in terms of configurations and compositions, with consequent restrictions on the resulting optical properties. In this work, the development of a new lithographic technique, based on self-assembly (SA) of block copolymers (BCPs), is proposed as a suitable fabrication route for the realization of HMMs, with in-plane optical axis, that operate in Vis frequencies. The novelty of this research activity relies on the employment of a dewetting process of BCP/homopolymer blend thin films over topographically defined patterns. The combination of bottom-up BCP nanopatterning and top-down optical lithography leads to ordered periodic lamellar nanostructures, in a hierarchical configuration, representing ideal platforms for the subsequent pattern transfer into hybrid Au/air HMMs. The hyperbolic behavior of the proposed material is supported by a strong reduction in the fluorescence lifetime dynamics of defects in nanodiamonds placed on top of

the HMM, along with a computed Purcell factor as high as 32 at 580 nm. However, due to the great sensibility of the optical properties of HMMs to their dimensional and compositional parameters, even slight variations in terms of nanofeature's height or refractive index determine a significant modulation of the photon emission enhancement. With the aim to optimize the optical performances, it is therefore crucial to establish a relationship of materials' functionality over their geometric and compositional parameters. This can be achieved by implementing, in a hybrid metrology approach, different analytical techniques to gain a comprehensive characterization of such nanostructures. This measurement strategy requires therefore the fabrication of materials that could be employed as model systems for a reliable interpretation and correlation of materials' functionality to their underpinning physical and chemical properties. Novel synthetic methods, based on the selective infiltration and growth of metal oxides, such as the sequential infiltration synthesis (SIS), are developed in order to provide the degree of control on the material fabrication, needed to meet the best conditions for enhanced optical performances. Then, an analytical strategy based on a hybrid metrology approach is applied to reveal dimensional and analytical information on such nanomaterials. The implementation of synchrotron-based traceable X-ray techniques with scanning probe and electron microscopies, along with a good knowledge of the relationship of each targeted measurand to the specific physical or chemical quantities of interest, allows for mutual validation and more complete, coherent description of complex samples.

Contents

List of Figures

List of Tables

Chapter 1

Hyperbolic Metamaterials by Block Copolymer Self-Assembly

Related publications:

[1] *Ferrarese Lupi, F., Murataj, I., Celegato, F., Angelini, A., Frascella, F., Chiarcos, R., Antonioli, D., Gianotti, V., Tiberto, P., Pirri, F. C., Boarino, L., & Laus, M. (2020). Tailored and Guided Dewetting of Block Copolymer/Homopolymer Blends. Macromolecules, 53(16), 7207-7217.*

[2] *Murataj, I., Channab, M., Cara, E., Pirri, C. F., Boarino, L., Angelini, A., & Ferrarese Lupi, F. (2021). Hyperbolic metamaterials via hierarchical block copolymer nanostructures. Advanced Optical Materials, 9(7), 2001933.*

This chapter is intended to cover the fabrication of hyperbolic metamaterials with in-plane optical axis by means of bottom-up approach based on self-assembly process, for the enhancement of photon emission of single-photon sources. In particular, this chapter provides a general introduction to metamaterials is given in section 1.1. Specific insights on hyperbolic metamaterials are provided in section 1.2, focusing on their fundamentals, the current state of the art on the fabrication of such materials and their relative main photonic features. The novelty of this research activity relies on the development of a new fabrication approach based on self-assembly of block copolymers that overcomes the intrinsic limitations imposed by conventional fabrication techniques, providing a greater control on the resulting material properties, described in section 1.3. The details of all methods and technologies exploited during the PhD project, from the fabrication

and material characterization to the optical characterization techniques are provided in section 1.4. Section 1.5 summarizes the results of this PhD project covering the optimization of block copolymer self-assembly process into hierarchical features, subsequently used as effective platforms for the nanofabrication of hyperbolic metamaterials with in-plane optical axis. The optical properties of the so obtained materials are assessed by means of fluorescence lifetime dynamic measurements, showing hyperbolic behavior in the Vis wavelength regime, supported by numerical modelling.

1.1 Metamaterials

The general term *metamaterial* is referred to artificially designed materials constituted by alternated metal-dielectric building blocks defined as meta-atoms [3]. In these artificial materials, the sub-wavelength typical dimensions of the constituent meta-atoms ($d << \lambda$) rise unusual optical properties that could not otherwise be found in naturally occurring materials. In the last decades, the significant research attention towards metamaterials was generated by the ability to specifically engineer their effective optical properties. Metamaterials offer a great flexibility in terms of meta-atoms' typical dimensions and compositions with direct implication, in a broad frequency range, into sensing [4,5], waveguiding [6] and imaging [7]. One peculiar class of metamaterials is represented by highly anisotropic metamaterials that display a hyperbolic dispersion. The specific interest of the research community to the so-called hyperbolic metamaterials (HMMs) arises from their distinctive optical properties for electromagnetic space engineering [8], light propagation [9] and strong enhancement of spontaneous emission [10], opening therefore the possibility for their exploitation into the development of quantum communication and quantum processing technologies.

1.2 Hyperbolic metamaterials

Hyperbolic metamaterials (HMMs) are optical artificial materials with the unique property of anisotropy given by the simultaneous presence of the major components of the permittivity tensor that hold different signs, rising unusual and novel optical phenomena. Highly localized bulk plasmon polaritons and surface waves with large wavevectors can be supported by the HMMs, crucial for various applications in sensing, imaging, nano-guiding and enhancement of spontaneous emission of single-photon sources. So far, HHMs have been subject of a lot of

interest in the scientific community in the last years, however the increasing demand for ever smaller and more powerful devices with added functionalities requires the integration of HMM into more complex structures. This demands therefore, the development of novel fabrication routes that go beyond the intrinsic limitations of conventional nanofabrication techniques in order to tailor the material properties.

In this chapter, the main properties related to the HMMs will be discussed with a focus on the fundamentals underpinning their extraordinary optical responses and the current state-of-art on the fabrication of such materials. A novel synthetic approach will be demonstrated by employing self-assembling materials, as block copolymers, to fabricate HMMs with in-plane optical axis at nanometric dimensions responsible for the enhancement of the spontaneous emission of single-photon sources in visible wavelengths.

1.2.1 Fundamentals

HMMs derive their name from their isofrequency surface topology [11] determined by the diagonal components of the permittivity tensors that simultaneously hold different signs. For a uniaxial medium, the dielectric tensor is

$$\bar{\bar{\varepsilon}} = \begin{bmatrix} \varepsilon_{xx} & 0 & 0 \\ 0 & \varepsilon_{yy} & 0 \\ 0 & 0 & \varepsilon_{zz} \end{bmatrix} \tag{1.1}$$

with in-plane components $\varepsilon_{xx} = \varepsilon_{yy}$ and out of plane component ε_{zz}.

For most natural occurring materials (Figure 1a), the permittivity components are all positive, resulting therefore in an isofrequency surface of linearly dispersed and isotropic propagating wave with spherical shape which is given by the equation:

$$\frac{k_x^2 + k_y^2}{\varepsilon_{zz}} + \frac{k_z^2}{\varepsilon_{xx}} = \frac{\omega^2}{c^2} \tag{1.2}$$

where ω is the radiation frequency and c is the free-space light velocity.

When one or two of the diagonal components of the permittivity tensor hold an opposite sign the isofrequency surface opens into a hyperboloid shape. This phenomenon does not naturally occur at optical frequencies but can be designed using nanostructured materials that show a different behavior as a metal or a dielectric in different direction.

One of the most important characteristics of HMMs is related to propagation of large magnitude wavevectors. Large wavevector waves are evanescent in vacuum with an exponential decay. The open hyperboloid shape of the isofrequency surface of HMMs allows the propagation of wavevectors with idealistically infinitely large magnitude [12,13]. This determines the absence of evanescent waves in this medium which rises several different applications in which hyperbolic media can be exploited [14,15]. The dual behavior of HMMs as metallic in one direction and insulating in the other, requires that both metals and dielectrics must be employed as building blocks on the fabrication of such materials. The high-k propagating waves supported by the HMMs originate by the metallic building block that is responsible for the hyperbolic dispersion. The high-k waves are created by the light-matter coupling as a consequence of the polaritonic properties of the metal of choice. More specifically, phonon-polaritonic and plasmon-polaritonic metals are required on the fabrication of metamaterials with hyperbolic dispersion. The near-field coupling of surface plasmon polaritons (SPPs) at the interface of each metal-dielectric structure, results in high-k modes that represent the Bloch modes of the metal-dielectric superlattice.

The HMMs can be classified into two types that identify their properties depending on the signs of the components of the permittivity tensor parallel ($\varepsilon_{\|}$) and perpendicular ($\varepsilon_{\perp}$) to the optical axis:

1. Type I: $\varepsilon_{\|} < 0$ and $\varepsilon_{\perp} > 0$,

2. Type II: $\varepsilon_{\|} > 0$ and $\varepsilon_{\perp} < 0$.

The major difference between Type I and type II HMMs is that the isofrequency surfaces are two or one sheeted hyperboloidal shapes, respectively. In Type I HMMs the dispersion band has a two-fold hyperboloid shape (Figure 1b), typical for metallic nanowires inside dielectric templates. On the other hand, in case of Type II HMMs, the dispersion has a one-fold hyperboloid shape (Figure

1c), typical for metal-dielectric multilayer structures. Moreover, Type II HMMs show a higher reflectivity since they are more metallic than Type I HMMs [16].

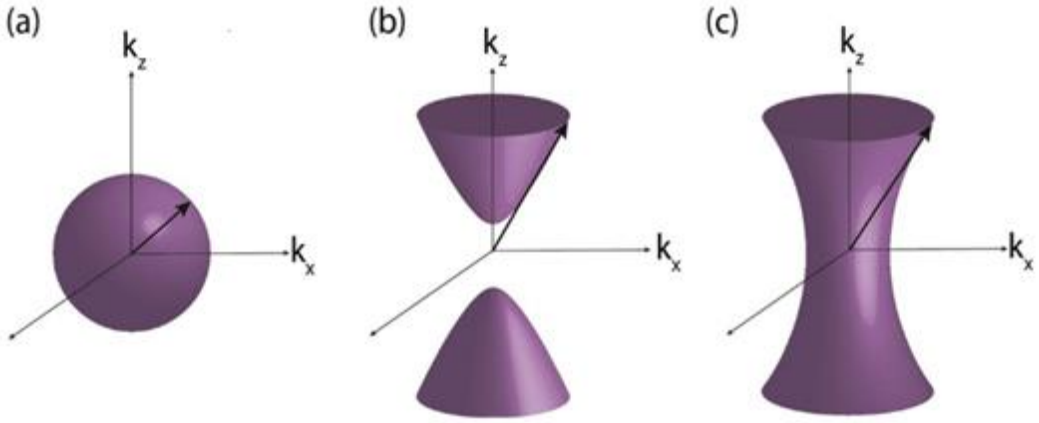

Figure 1: (a) Isofrequency surface for an isotropic dielectric (spherical shape), (b) two-sheeted hyperboloidal isofrequency surface for Type I HMM ($\varepsilon_{\parallel} < 0$ and $\varepsilon_{\perp} > 0$,) and (c) one-sheeted hyperboloidal isofrequency surface for Type II HMM ($\varepsilon_{\parallel} > 0$ and $\varepsilon_{\perp} < 0$). Adapted from [17].

1.2.2 Hyperbolic metamaterials platforms

The overall advancement on the fabrication techniques for complex and multicomponent materials at micro and nanoscale level provides great flexibility in the design and realization of HMMs with tailored optical properties [8,18]. In the last decades, the fabrication of HMMs relied into two main structural configurations: (a) multilayered configuration of metal films separated by dielectric layers [19] (Figure 2a) and (b) metallic nanowires hosted in dielectric templates [20] (Figure 2b).

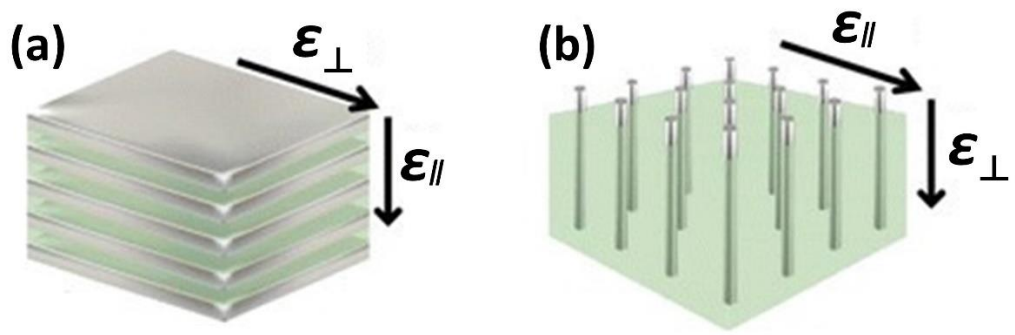

Figure 2: (a) HMM in multilayer configuration consisting of alternating metallic and dielectric layers and (b) nanowire configuration consisting of metallic nanowires hosted in a dielectric template. Adapted from [17].

Metamaterials in which the metal and dielectric dimensions are much smaller than the wavelength of the incident beam ($d << \lambda$), can be described exploiting the effective medium approximation (EMA) in order to simplify the estimation of their optical behavior (*e.g.* transmission and reflection spectra). In this kind of description, the HMM is observed and considered as a homogeneous medium with averaged permittivity values along the directions perpendicular and tangential to the optical axis. For HMMs in multilayered configurations the effective parallel and perpendicular permittivities ($\varepsilon_{\parallel}^{eff}$ and $\varepsilon_{\perp}^{eff}$) are expressed in the form of:

$$\varepsilon_{\parallel}^{eff} = \frac{\varepsilon_m \cdot \varepsilon_d}{f_d \cdot \varepsilon_m + f_m \cdot \varepsilon_d}, \tag{1.3}$$

$$\varepsilon_{\perp}^{eff} = f_m \cdot \varepsilon_m + f_d \cdot \varepsilon_d, \tag{1.4}$$

where ε_m, ε_d are the permittivities of metal and dielectric layers, and f_m, fd are the fractions of metal and dielectric in the multilayer, respectively. Eq. (1.3) and (1.4) clearly suggest that the effective permittivities of the overall metamaterial can be tuned by adjusting the combination of different metals (ε_m) and dielectrics (ε_d) and their respective volume fractions (f_m and f_d) with direct consequences on the resulting optical properties.

The implementation of EMA is quite straightforward for multilayer and nanowire structures but unfortunately, there are several limitations to consider on

the HMM building block dimensions, number of periods and range of angles of incidence. All these parameters can determine a cutoff for large-*k* modes sustained by the HMM [16,21,22] and limit the range of applicability of this approximation. Moreover, the dispersion starts to significantly deviate from the EMA prediction for very large wavevectors [23].

Multilayer HMMs have been subject of extensive studies thanks to the relative easiness on their fabrication which is based predominantly on the deposition and growth of alternating metallic and dielectric layers. The fabrication of multilayer HMMs took advantage of the great technological advancements on deposition technologies that guarantee minor deviations on the layer thickness and on low surface roughness that might be responsible for light scattering and material loss issue [24–26]. The most common material deposition techniques *e.g.* sputtering, evaporation, physical and chemical vapor deposition (PVD, CVD) and atomic layer deposition (ALD), offer a wide choice of plasmonic metals and dielectrics with high refractive indexes that can be exploited to fabricate metamaterial with hyperbolic behavior in different wavelengths ranges.

Gold or silver, in combination with alumina have been deposited by electron beam evaporation in layer thicknesses of 22 nm and 40 nm, representing the ideal metal-dielectric platform for the fabrication of HHMs that show hyperbolic behavior at ultraviolet (UV) frequencies [16,27]. To extend the design of HMMs to visible wavelengths however, high refractive index dielectrics such as TiO_2, SiO_2 or SiN are needed [28,29] using reactive sputtering or by pulsed laser deposition methods to maintain the stoichiometry [30] (Figure 3).

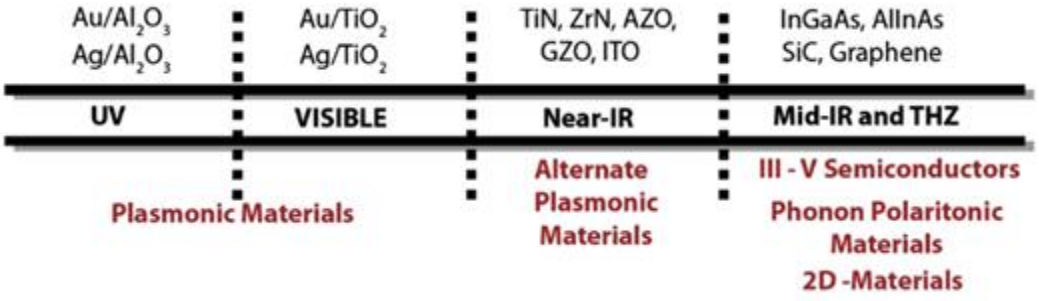

Figure 3: Different materials and metal-dielectric combinations used to fabricate HMMs at different operating regions of the electromagnetic spectrum (UV to mid-IR and THZ frequencies). Adapted from [17].

Other plasmonic materials as titanium nitride (TiN) [31], aluminum-doped zinc oxide (AZO) [32] and silicon carbide (SiC) were grown by plasma enhanced

chemical vapor deposition (PECVD) and used as effective constituents of HHMs in the near and mid-IR wavelengths [16]. In case of III-V semiconductors, molecular beam epitaxy (MBE) was used to grow uniform and smooth alternating layers of a same semiconductor but with different doping levels where the highly doped semiconductors behaved as metals [19]. Finally, it has been reported that multilayer graphene super-lattices showed a hyperbolic response in the THz spectrum range [33]. Similar to the multilayers, for HMMs in nanowire configurations the effective permittivities $\varepsilon_{\parallel}^{eff}$ and $\varepsilon_{\perp}^{eff}$ are expressed in the form of [18]:

$$\varepsilon_{\parallel}^{eff} = \frac{(1+f_m)\varepsilon_m \cdot \varepsilon_d + (1-f_m)\cdot \varepsilon_d^2}{(1+f_m)\varepsilon_d + (1-f_m)\cdot \varepsilon_m}, \tag{1.5}$$

$$\varepsilon_{\perp}^{eff} = f_m \cdot \varepsilon_m + f_d \cdot \varepsilon_d, \tag{1.6}$$

where the permittivities of metallic nanowires and dielectric host are indicated with ε_m and ε_d, while f_m and f_d correspond to the respective volume fractions of metal nanowire and dielectric template. The typical fabrication of nanowire-based HMMs relies on the electrodeposition of the metals (Au and Ag) into anodic alumina membranes [34], indium-tin-oxide (ITO) [35] and AZO [36] as dielectric host medium. The periodic nanoporous structure of the dielectric matrix determines the resulting metallic nanowires dimension, typically in the range of 20-700 nm in length, 10-50 nm in diameter and 40-70 nm rod separation [20]. Moreover, it is clear that the porosity of the dielectric template controls the final metal fill factor, indicating that a proper choice on the template's dimensional characteristics is needed in order to tailor the hyperbolic behavior of the resulting material.

1.2.3 Spontaneous emission enhancement

One of the most important features of HMMs is the ability to engineer the local density of optical states (LDOS) [32–35]. For isotropic dielectrics, the closed isofrequency surfaces such as spheres and ellipsoids lead to a finite value, hence the radius in the *k*-space determines a cut-off of the high-*k* modes so that they become evanescent waves. Instead, for hyperbolic medium, the isofrequency

surface diverges into theoretically infinite LDOS, supporting therefore the propagation of infinite magnitude wavevectors. This peculiar optical behavior allows for spontaneous emission properties of photon emitters coupled to HMMs that go beyond those that can be reached with traditional optical materials, such as photon emission enhancement, control of the emission directivity and of the emission spectrum. As stated by Fermi's golden rule, an increase of the density of available electromagnetic modes directly influences the spontaneous emission lifetimes of photon emitter [37]. When photon emitters as fluorescent dye molecules, NV-centers in nanodiamonds and quantum dots are in proximity to the HMM, the interaction is dominated by the preferential coupling of the emitters with the high LDOS modes that provide a large number of radiative decay channels. This leads to an overall increase in the radiative decay rate (Purcell factor) with direct consequences on photoluminescence enhancement and lifetime shortening [27]. The Purcell factor is defined as:

$$F_P = \frac{\Gamma_{HMM}}{\Gamma_0} \tag{1.7}$$

where Γ_{HMM} is the enhanced radiative decay rate of the emitter due to the HMM and Γ_0 is radiative decay rate of the emitter in free space. In this definition only radiative decay rates are used, therefore representing the correct measurement for photoluminescence enhancement. The neat decay rate of the emitter can be obtained by time-resolved measurements of spontaneous emission, in which the total lifetime (τ) can be expressed as:

$$\frac{1}{\tau} = \frac{1}{\tau_{rad}} + \frac{1}{\tau_{non-rad}} \tag{1.8}$$

where τ_{rad} is the radiative lifetime and $\tau_{non\text{-}rad}$ is the non-radiative lifetime. Although many experiments reported the successful coupling of photon emitters with multilayer or nanowire HMMs, one must take into account the different contributions (radiative, non-radiative, vacuum, surface plasmon polaritons and high-*k* modes) responsible for the lifetime decrease. For instance, when the distance of a photon source in proximity to the HMM surface reduces, non-radiative decay phenomena (*i.e.* quenching effects in the metal layer of the HMM)

increase, leading to an overall lifetime reduction, however without the ability to exploit this emission enhancement for fluorescence detection or any other application. One solution to overcome this issue is represented by tuning the emission directivity to obtain higher outcoupling efficiency.

As mentioned before, placing a quantum emitter in proximity of an HMM determines a drastic enhancement of the spontaneous emission rate. However, the practical implementation of quantum emitters into on-chip integrated systems, is prevented by the low photon extraction efficiency of supported high-k modes that cannot propagate to the far-field because intrinsically confined inside the HMM itself [38]. The low outcoupling efficiency of quantum emitters with guided modes of nanofibers or waveguides leads to an overall low repetition rate which is given by the product of outcoupling efficiency and the enhancement of the spontaneous emission rate. High repetition rates are fundamental requirements for the enhancement of the on-chip photon extraction decay rate for single-photon sources on a broad spectral range, to guarantee fast bit rates for a variety of application as quantum communication and quantum information processing [39]. One strategy which can be applied to overcome the limitations mentioned above, is represented by a judicious control on the orientation of HMM's optical axis. Shen *et al*. [40] theoretically demonstrated that by properly tilting the in-plane optical axis of the HHMs with respect to the end-facet of nanofibers, the high-k hyperbolic modes and the guided modes of the nanofibers become momentum-matched, also suppressing any reflection at the interface. In the proposed configuration illustrated in Figure 4a, the in-plane optical axis of the HMM is tilted by an angle θ with respect to the end-facet of nanofiber, therefore the isofrequency surface in the x-y plane can be expressed as:

$$\begin{aligned}\left(\varepsilon_{||}\sin^2\theta+\varepsilon_{\perp}\cos^2\theta\right)k_z^2+2(\varepsilon_{||}-\varepsilon_{\perp})\sin\theta\cos\theta k_x k_z\\+\left(\varepsilon_{||}\cos^2\theta+\varepsilon_{\perp}\sin^2\theta\right)k_x^2=k_0^2\varepsilon_{||}\varepsilon_{\perp},\end{aligned} \tag{1.9}$$

in which k_x and k_z are the wavevector's k parallel and perpendicular components to the end-facet of the nanofiber, $k_0 = \omega/c$; and c is the speed of light in free space. If we set the real part of the parallel components of the HMM's permittivity tensor positive ($\mathrm{Re}(\varepsilon_{\|}) > 0$) and perpendicular one's negative ($\mathrm{Re}(\varepsilon_{\perp}) < 0$) we end up with two solutions of k_z for any value of k_x if $\theta = 0$ (Figure 4b). On the other hand, there is only one solution if $\theta = \varphi_c$, where φ_c is the critical angle

between the optical axis and the of hyperbolic isofrequency contour's asymptotic line (Figure 1.4c).

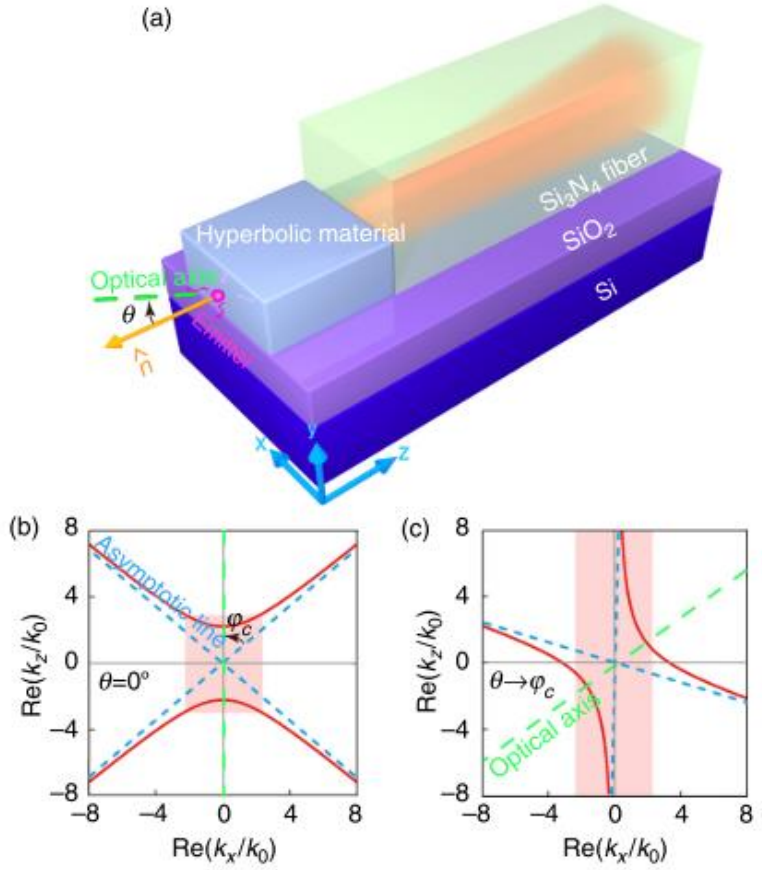

Figure 4: (a) Schematics of HMM with in-plane optical axis tilted with an angle θ with respect to the nanofiber's end-facet. Hyperbolic isofrequency contours of HMMs with un-tilted $\theta = 0$ (b) and tilted $\theta = \varphi_c$ (c) optical axis. The red areas in (b,c) are $|\mathrm{Re}(k_x/k_0)| \leq n_{\mathrm{fiber}}$ where n_{fiber} is the refractive index of the nanofiber material (Si_3N_4). Adapted from [40].

At tilted angles ($\theta = \varphi_c$) the phase-matching conditions guarantee a high on-chip photon extraction decay rate thanks to a very efficient transformation of high-k hyperbolic modes into the nanofiber's guiding modes, suppressing any reflection at the end-facet interface. Otherwise, for HMMs with un-tilted optical axis ($\theta = 0$) the hyperbolic modes remain intrinsically confined inside the material itself without any coupling with the nanofibers. HMM in conventional multilayer and nanowire configurations, however, do not offer flexibility in terms of optical axis orientation, preventing as a consequence their on-chip integration for the realization of more complex photonic devices and circuitries. One possible

solution is represented by HMMs with in-plane optical axis that have demonstrated to be valuable in different fields as nanoimaging and integrated photonic circuitries [5]. However, HMMs that work at visible wavelengths, require subwavelength dimensions of the metal and dielectric components in in-plane configuration. The fabrication of such materials is therefore still challenging due to the physical limitations imposed by conventional nanofabrication techniques in the definition and deposition of materials at subwavelength level.

The seek for advanced materials with boosted performances has pushed the research towards the development of novel nanofabrication approaches in order to provide a greater flexibility on the design and fabrication of materials with tailored properties. In the last decades, the fabrication of complex materials at the nanoscale, such as 3D structures and multicomponent hybrid materials, took advantage of the recent developments of bottom-up fabrication approaches. Bottom-up methods, as self-assembly process of block copolymers (BCPs) gained ever more interest in the definition and at priori-design of nanometric structures, with a high throughput, that are readily integrable into high-volume production lines. These methods represent therefore ideal candidates when it comes to the choice on the techniques for the fabrication of HMMs, providing high-density nanostructures with subwavelength dimensions (typical range of 10 - 100 nm) in a variety of morphologies and configurations that carry chemical functionalities that can be exploited for subsequent pattern transfers.

1.3 Bottom-up fabrication

The main goal of the research branch concerning HMMs is to tailor the optical properties of the material by exerting the control over the dimensions, the spatial placement, orientation and composition of the single building blocks. All these features heavily depend on the techniques for nanofabrication. Top-down lithographic tools as electron beam lithography (EBL) and direct laser-writing (DLW) offer excellent control on the geometrical parameters, giving access to a wide range of shapes and sizes, especially when combined with etching and micromachining techniques as reactive ion etching (RIE) and focused ion beam (FIB). However, despite these characteristics, obstacles on the fabrication of high-density multicomponent materials with in-plane configurations over a wide area still remain. To accomplish this request, bottom-up fabrication approaches, as self-assembly processes, are becoming popular solutions in nanofabrication in the last years, thanks to their promise to overcome the intrinsic limitations of conventional techniques.

1.3.1 Self-assembly process

The self-assembly process (SA) is defined in chemistry as "*the spontaneous and reversible organisation of molecular units into ordered structures by non-covalent interactions"* [41]. The SA is classified as a bottom-up approach which involves the arrangement of small units (usually molecules), referred to as nano-building blocks (NNBs) into higher structures in different shapes and architectures. The most peculiar feature of SA is that the self-organization of the NNBs into ensembles is driven by local forces without the intervention of any applied external force. Different nanostructures are achievable by the proper choice of the size, morphology, composition and functionalities of the NNBs. The long-range ordering of the resulting nanostructures can be further extended by implementing the SA process into guiding template, usually defined by optical or electron lithography [42]. The SA process is driven by intermolecular interactions (*e.g.* Van der Waals, capillary, π-π or hydrogen bonds) between the NBBs that display a key role in the formation of the nanometric ensemble even though being weaker than covalent, ionic and metallic bonds.

There are several examples of materials that can be fabricated by exploiting the SA process, as colloids, lipid bilayers, molecular crystals, self-assembled monolayers and phase-separated polymers [41,43], other than biological systems like self-assembled polypeptide chains and nucleic acids into their active forms [44]. In contrast to polymerisation or covalent synthesis, the NBBs units interact among each other without forming a covalent bond. Instead, the driving force of the SA relies on the seek for a lower Gibbs free energy. Consequently, the NBBs organize themselves into the best configuration at the thermodynamic minimum. The thermodynamic stability of the resulting self-assembled NBBs is higher than the single component. A fundamental condition required to obtain self-assembled structures is the simultaneous presence of both long-range repulsive and short-range attractive forces [45], (Figure 5).

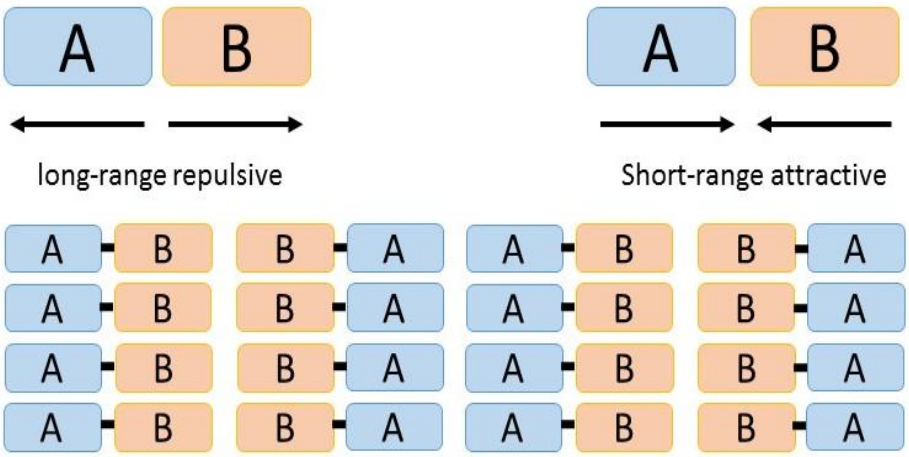

Figure 5: Long-range repulsive and short-range attractive interactions schematics between two chemically different units A and B.

The judicious choice of NBBs with suitable physicochemical properties, enables the possibility to exert a fine control on the resulting self-assembled nanoarchitectures. These properties can be finely tuned by the chemical synthesis, enabling therefore the ability to design the resulting intermolecular interactions in terms of strength and selectivity [46]. Among the various nanopatterning self-assembling materials, BCPs have emerged as a cost-effective and scalable bottom-up approach, suitable in various nanofabrication applications. In particular, BCPs provide highly dense and periodic patterns at the nanometric scale with a high throughput that go beyond the conventional nanopatterning tools.

1.3.2 Block copolymer lithography

BCP represent a special class of polymeric materials, formed by two or more polymeric chains linked together by a covalent bond [47]. One of their major properties is that these soft materials have fluidlike disorder at a molecular level but high order degree at longer length scales. The term BCP is referred to a variety of macromolecules composed of different polymeric blocks with different monomeric units. They can be referred to as diblock (n = 2), triblock (n = 3) or multi block (n > 2) copolymers depending on the number of blocks of which they are composed. These polymeric systems can be also classified based on the different molecular architectures. They can be linear, cyclic, star or heteroarm star BCPs [48] (Figure 6a-d).

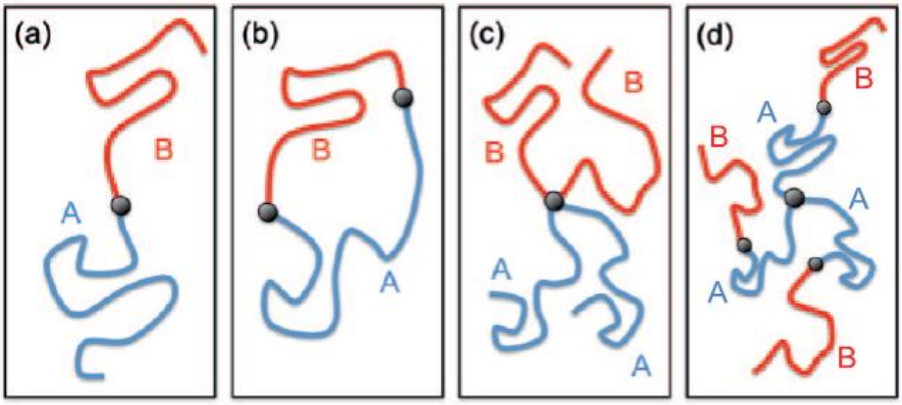

Figure 6: Molecular architectures attainable through polymerization of a block copolymer composed of two distinct monomers: (a) linear, (b) cyclic, (c) star diblock and (d) heteroarm star copolymers. Adapted from [49].

The most studied BCPs are the linear ones due to their simple structure (Figure 6a). They are formed by two distinct homopolymer chains A and B covalently linked together at one chain end. If both chain ends of each homopolymer chain are linked, this leads to a cyclic BCP (Figure 6b). The star copolymers are formed by multiple homopolymer chains linked to the same junction point (Figure 6c). Similarly, the heteroarm star copolymers are formed by connecting multiple BCPs to the same junction point (Figure 6d). The SA of BCPs can be described as the phase separation of the two constituent blocks driven by their chemical incompatibilities. When compared to low molecular weight polymer mixtures, the mixing entropy per unit volume of higher molecular weight homopolymers is smaller and scales inversely to the molecular weight. This results in a phase separation due to the increase of free energy even for small structural differences between the blocks A and B. Since in amphiphilic block copolymers the A and B blocks are covalently linked, the two different interactions (long-range hydrophobic-hydrophilic repulsion and short-range covalent attraction) coexist. This constrains the phase separation into structures with typical dimensions at the nanometric scale (5 – 100 nm) [50].

The main factors that influence the BCP behaviour in a linear block copolymer are:

- The degree of polymerization (N), which represents the number of monomeric units in a polymer.
- The Flory-Huggins interaction parameter (χ), used to describe the excess of free energy of mixing and to estimate the immiscibility of the constituent blocks.
- Geometric factors: the volume fraction (f_α and f_β) of each component of the diblock BCPs.

The enthalpic measure of interaction between two immiscible blocks is given by the Flory-Huggins parameter (χ), which describes the increase in the Gibbs free energy when the two blocks A and B are mixed. The Flory-Huggins parameter is expressed in thermal energy units k_BT by the equation:

$$\chi_{\alpha\beta} = (z/2)\left[\epsilon_{\alpha\alpha} + \epsilon_{\beta\beta} - 2\epsilon_{\alpha\beta}\right]/k_BT \tag{1.10}$$

in which Z is the number of nearest neighbour monomers to a copolymer configuration cell, k_B is the Boltzmann constant, $\varepsilon_{\alpha\beta}$ is the energy interaction per monomer between monomers of different blocks, while $\varepsilon_{\alpha\alpha}$ and $\varepsilon_{\beta\beta}$ are the energy interactions between the same monomers on the same block chain. For positive $\chi_{\alpha\beta}$ values the free energy drives the A and B system towards a net repulsion, while negative values indicate that the mixing is favoured. In other words, for negative $\chi_{\alpha\beta}$ the contact between A and B leads to lower energies than the sum contacts between the monomers on the same block. However, in contrast to homopolymer blends, the covalent bond linking the two different blocks prevents a macrophase separation, counterbalancing the thermodynamic forces involved in the phase separation. This leads therefore to a nanostructured self-organization [51].

The driving force that leads the phase separation can be quantified by the product of the polymerisation degree (N) of the BCP with the overall Flory-Huggins parameter for A and B interaction ($\chi_{\alpha\beta}$). By plotting the χN parameter with the volume faction of the A block (f_A) one can obtain the morphology diagram of a diblock copolymer system (Figure 7).

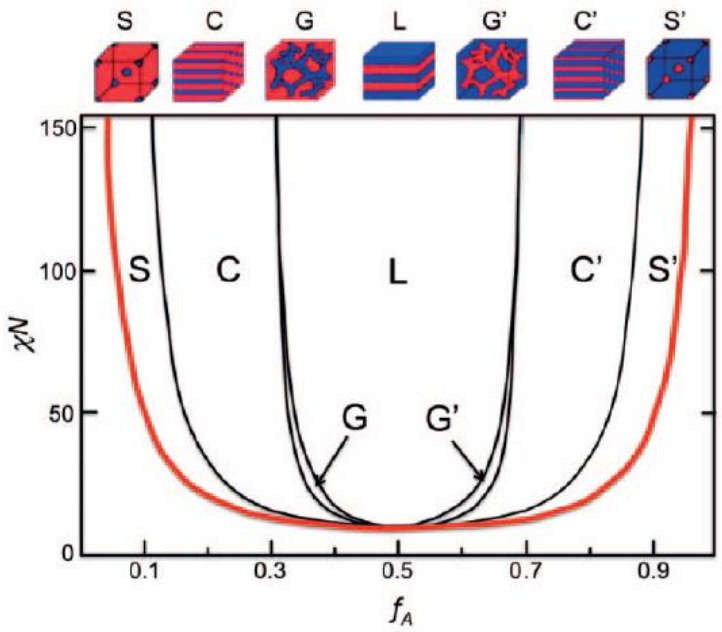

Figure 7: Schematic phase diagram of a diblock copolymer system showing the different phases as spherical (S), cylindrical (C), gyroid (G) and lamellar (L). Adapted from [49].

The red line delimitates the transition of diblock copolymers from a disordered to an ordered state depending on the χN value for a given f_A. Below a threshold value of χN =10, entropic factors dominate, favouring the mixing between the polymeric chains of the two blocks. Under these conditions the BCPs are in a disordered state in which we cannot observe any phase separation. At higher χN values (> 10) an order-disorder transition (ODT) into periodic nanostructures starts to take place due to a progressively reduced contact between the two blocks. At these χN values the nanostructures are characterized by narrow interfaces and well-defined composition profiles.

Above the ODT condition, changes in f_A affect the morphology and packing symmetry of the resulting phase-separated nanostructures. Self-consistent mean-field calculations predict four different phases of thermodynamic stability: spherical, cylindrical, gyroid and lamellar morphologies [52–54]. The patterns of highly asymmetric diblock copolymers with a ratio above 80:20 are zero-dimensional spheres arranged in a body-centred cubic (BCC) lattice of polymer B embedded in a polymer A matrix. Hexagonally packed (HP) cylinders of the minority component are formed for BCP with ratio 70:30. For a very narrow compositional ratio interval, double gyroids are formed. Finally, highly symmetric (ratio 50:50) BCPs self-assemble into two-dimensional lamellae.

While the volume fraction dictates the morphology in which the BCP self-assemble, the total molecular weight (M_n), given by the multiplication of N with the molecular weight of the monomeric units (M_0) of the BCP determines the periodicity (L_0) and the typical dimensions of the resulting nanostructures (Figure 8) [54].

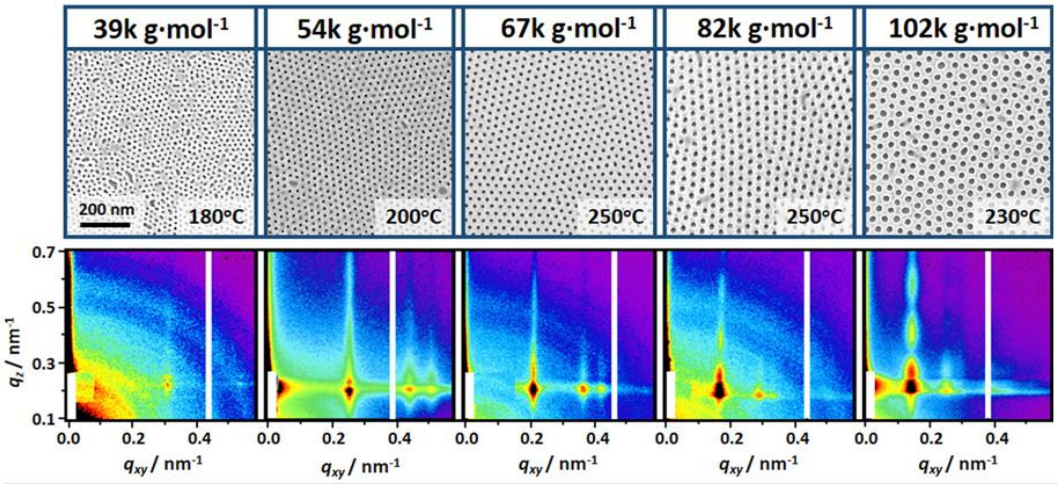

Figure 8: SEM micrographs of PS-*b*-PMMA diblock copolymer with 70:30 ratio in perpendicular orientation at increasing M_n and relative GISAXS patterns. Adapted from [55].

Thanks to the ability to self-assemble into highly periodic templates with nanometric dimensions, the interest on BCPs has grown over the last years for their implementation into nanopatterning applications. In this regard, despite the strong interest, the practical implementation of BCPs into industrial applications is still prevented by some hurdles. The stringent constrains imposed by microelectronics require a precise control of the SA over the fabrication of highly dense and high-aspect-ratio nanostructures and low defectivity with sharp side walls for pattern transfer [56]. This goal can only be achieved by a comprehensive understanding of the nanofeatures' dynamics and of the influence of processing conditions on the resulting morphology, defectivity and orientation of self-assembled BCPs [49].

There are several amphiphilic BCPs that have been studied and exploited for nanofabrication, such as polystyrene-*b*-polydimethylsiloxane (PS-*b*-PDMS), [57] polystyrene-*b*-poly(methyl methacrylate) (PS-*b*-PMMA), [58] polystyrene-*b*-poly2-vinylpyridine (PS-*b*-P2VP), [59] or polystyrene-*b*-poly(ethylene oxide) (PS-*b*-PEO) [60]. PS-*b*-PMMA (illustrated in Figure 9) has been the prototypical BCP used in the scientific community when it comes to studying and understating

of the SA mechanism. PS-*b*-PMMA holds most of the characteristics required by an ideal sublithographic patterning material [60], as the easy processing and chemical similarities with conventional photoresist materials, representing therefore a promising candidate for its integration with current top-down lithographic techniques.

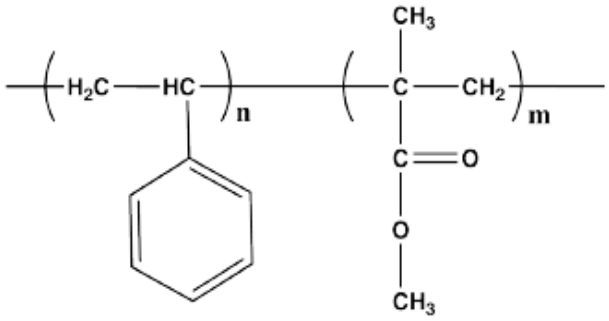

Figure 9: Structure of poly(styrene-*block*-methyl methacrylate) (PS-*b*-PMMA).

Some of the main characteristics of PS-*b*-PMMA are represented by its solubility in common solvents as toluene, acetone and tetrahydrofuran that favours an easy deposition over large scale on wafers by spin-coating. Moreover, thanks to the chemical differences between PS and PMMA it is possible to selectively remove one of the two polymeric domains (*i.e.* the PMMA) in acetic acid bath or by O_2 plasma, revealing a robust PS template that can be exploited for further pattern transfer processes. One of the drawbacks of PS-*b*-PMMA is represented by its low interaction parameter ($\chi \sim 0.04$ at 150 °C [60]) which limits the achievable typical dimensions of the self-assembled nanostructures as the diameter (d), width (W) and pitch size (L_0). However, the weak interaction parameter between the two blocks makes for an easy perpendicular orientation of the nanodomains, extending therefore the library of achievable nanopattern configurations as periodic nanopillars and alternated lamellar fins (Figure 10a-d). The perpendicular orientation of the nanodomains can be induced by tuning the polymer/surface interaction [61,62] through substrate functionalization *via* random copolymer (RCP) grafting process [63–65]. In these conditions, the absence of any preferential wetting of neither of the two blocks to the functionalized substrate, results in a perpendicular orientation of the nanodomains, representing optimal templates for lithographic purposes due to the higher aspect ratio achievable when compared to parallel oriented cylindrical and lamellar nanostructures.

The great flexibility offered by SA of BCPs in terms of morphology, dimensions and orientation opens the possibility to exploit BCPs as effective templates for the fabrication of advanced materials with tailored properties as HMMs with in plane configuration [2].

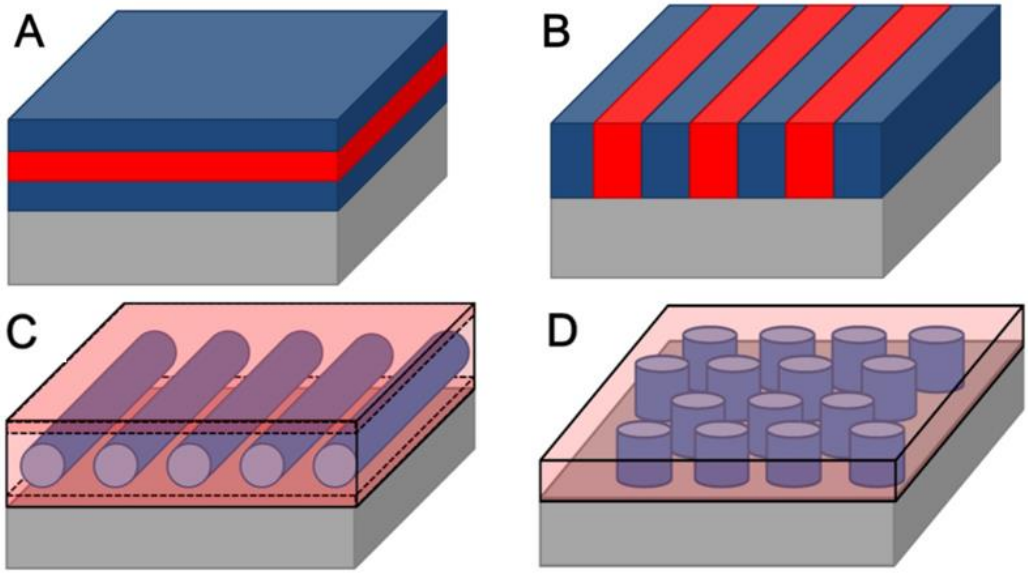

Figure 10: Schematics of (a,c) lamellar and cylindrical nanostructures in parallel orientation to the substrate and (b,d) lamellar and cylindrical nanostructures in perpendicular orientation to the underlying substrate. Adapted from [66].

1.4 Material and Methods

1.4.1 Block copolymer nanopatterning

In the following experiments, lamellar-forming polystyrene-*block*-polymethyl methacrylate (PS-*b*-PMMA) with styrene volume fraction (f_{PS}) = 0.50 (wt/wt), polydispersity index (PDI) = 1.09 and molecular weight (M_n) of 66 kg mol^{-1} were employed. The PS-*b*-PMMA was purchased from Polymer Source Inc. and used without further purification. PS and PMMA homopolymers were synthesized by the group of Prof. Laus at Università del Piemonte Orientale [1]. The BCP/homopolymer blend was constituted by mixing the symmetric BCP with 50% (by weight) for each homopolymer so that the total homopolymer mass fraction is ~2 times the mass fraction of each individual homopolymer. The solution was prepared by dissolving 9 mg of BCP with 4.5 mg of PS and 4.5 mg of PMMA in 2 ml of toluene. Polystyrene homopolymer is labelled as CS with a

M_n = 3.1 kg mol^{-1} and PDI = 1.09 while polymethyl methacrylate homopolymer is labelled RMM1 with a M_n = 3.9 kg mol^{-1} and PDI = 1.18. The neat BCP solutions were prepared by dissolving 18 mg of PS-*b*-PMMA in 2 ml of toluene. The random copolymer used for the substrate neutralization and promotion to perpendicular orientation of BCP nanostructures was a polystyrene-*random*-polymethyl methacrylate (PS-*r*-PMMA) labelled FSM7 with M_n = 14.60 kg mol^{-1}, f_{PS} of 58.7% (wt/wt) and PDI = 1.30.

BCP fabrication protocol is schematically represented in Figure 11:

a) Substrate cleaning;
b) Substrate functionalization with random copolymer PS-*r*-PMMA;
c) Block copolymer deposition and thermal processing;
d) Selective PMMA phase removal;

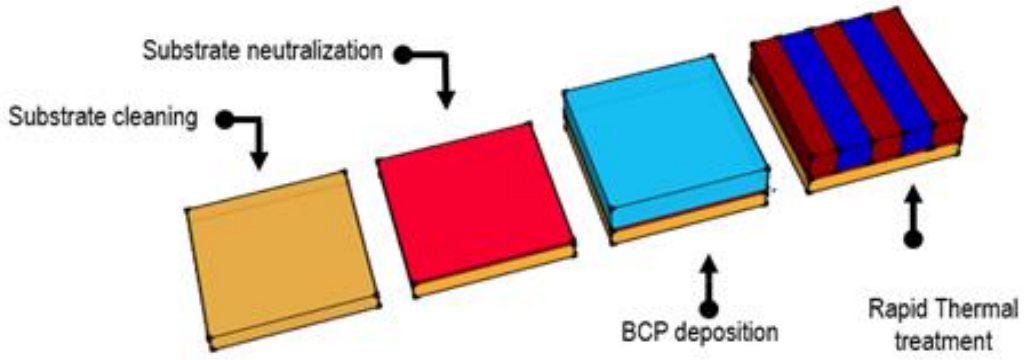

Figure 11: Schematics of a generic BCP nanopatterning protocol.

1.4.2 Graphoepitaxy patterns

In order to guide and locate the BCP patterns into specific sample locations, regular arrays of micrometric lines were fabricated by means of direct laser lithography in combination with reactive ion etching (RIE). Heidelberg Laser Writer µPG101 (Figure 12a) was used to define specific patterns with different sizes and periodicities over a 5 mm x 5 mm area on a silicon substrate. An optical commercial positive resist AZ 5214E MicroChemicals GmbH was spin-coated on a previously cleaned silicon substrate for a total thickness of 1 µm and subsequently exposed to a laser beam with 15 mW power and 375 nm

wavelength. The development was performed right after the exposure by sample immersion for 40 s in a 1:1 solution of AZ developer (Merck Performance Materials GmbH) and deionized H_2O, followed by subsequent water rinsing for 60 s. Once defined the micropatterns, their propagation into the substrate was performed by RIE in a PlasmaPro 100 Cobra 300 ICP (Oxford Instruments Plasma Technology) (Figure 12b) with fluorine-based chemistry (C_4F_8 and SF_6) for a final depth of 200 nm of the resulting microstructures.

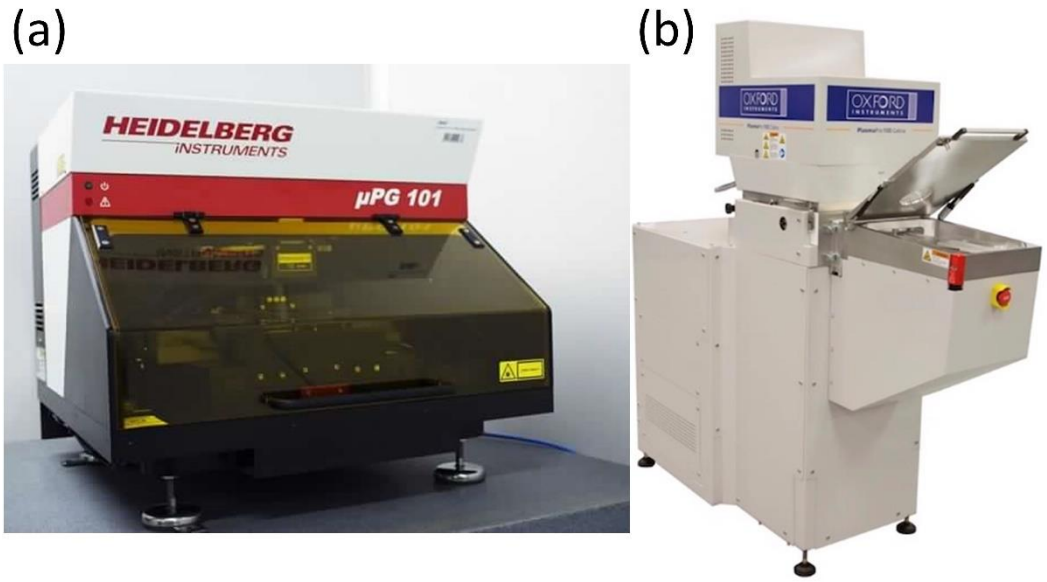

Figure 12: (a) Laser Writer µPG101 from Heidelberg and (b) PlasmaPro 100 Cobra 300 ICP from Oxford Instruments Plasma Technology in the QR Laboratories at INRiM.

1.4.3 Substrate functionalization and BCP deposition

Prior to the functionalization, the substrates were cleaned in ultrasonic bath with acetone for 3 minutes, followed by an isopropanol bath for 2 minutes and finally dried with N_2 flux. The activation step of silicon substrates with 1.5 nm-thick native oxide layers took place in a plasma Matrix cleaner by O_2 treatment at 130 W for 6 minutes. Afterwards, a solution of PS-*r*-PMMA (18 mg in 2 ml of toluene) was spin-coated onto the Si wafers at 3000 rpm for 60 s. The grafting process was promoted by thermal annealing treatments in a rapid thermal processing (RTP) JetFirst 100C Furnace from Jipelec^{TM} at high temperature (T_a = 290 °C) for an annealing time (t_a) of 300 s in N_2 environment (Figure 13a). Afterward, a sonication bath in toluene for 6 minutes removed any nongrafted chain, for a final RCP grafted layer of 7 nm. All the polymeric film thicknesses

were determined by spectroscopic ellipsometry measurements with an alpha-SE ellipsometer, J.A. Wollam Co (Figure 13b). Both the neat BCP and the BCP/homopolymer blend thin films were deposited on top of the grafted RCP layers by spin-coating at 3000 rpm for 60 s for a final thickness of 35 nm and subsequently annealed by RTP in a range of annealing temperatures from 210 °C to 330 °C, with annealing times from 30 s to 1200 s. The final step consisted in the selective removal of PMMA nanodomains of the self-assembled nanostructures by exposure to ultraviolet radiation (5 mW cm^{-2}, $\lambda = 253.7$ nm) for 180 s followed by isotropic O_2 plasma etching (40 W for 30 s).

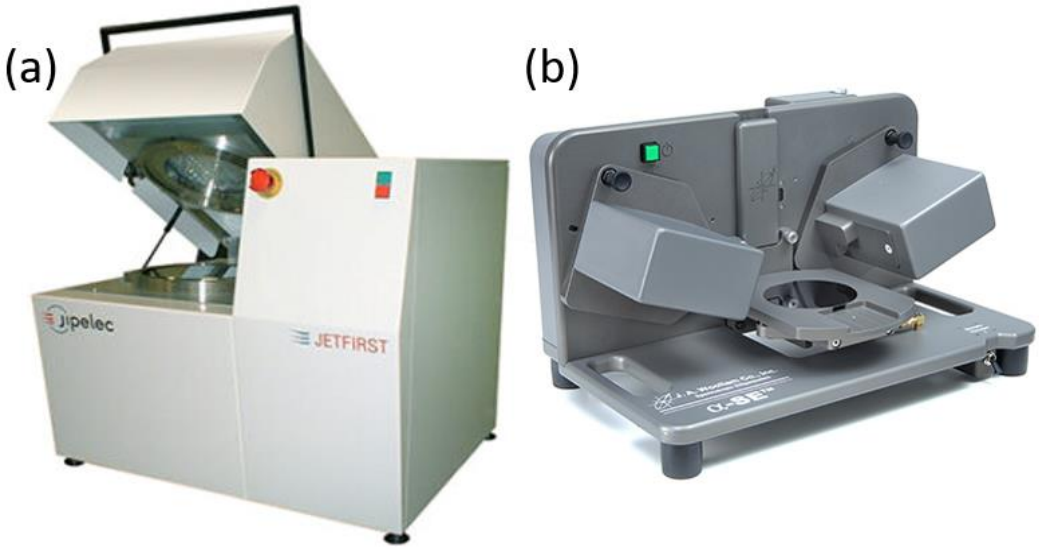

Figure 13: (a) JetFirst RTP 100C from Jipelec™ and (b) spectroscopic ellipsometer by J.A. Wollam Co in the QR Laboratories at INRiM.

1.4.4 Pattern transfer

The pattern transfer process of the BCP templates into Au/air HMM was performed by depositing a continuous layer of Au with 70 nm thickness and subsequent mechanical stripping. The metal was deposited by a homebuilt RF sputtering system with Ar plasma at 100 W at $5 \cdot 10^{-3}$ mbar, yielding a deposition rate of 0.2 nm s^{-1} (Figure 14). The following deposition of a UV-curing resin (Optical Norland Adhesive 81) on top of the Au layer facilitated the mechanical stripping of the metallic layer from the polymeric template.

Figure 14: Homebuilt RF sputtering system used for the gold deposition in the QR Laboratories at INRiM.

1.4.5 Morphology characterization

The morphological inspection of the polymeric templates and of the Au-stripped films were monitored by scanning electron microscopy (SEM) utilizing a FEI Inspect-F field emission gun scanning electron microscope (FEG-SEM) coupled with an Everhart-Thornley secondary electron detector (ETD) (Figure 15a). Backscattered electron detectors (BSEDs) were used to investigate the Au nanofeatures. Data analysis of the SEM micrographs of dewetted BCPs in terms of geometrical properties was conducted by ImageJ software. The binarization with automatic thresholding of the SEM micrographs allowed to fit the outlines of the dewetted droplets with ellipses in order to evaluate the circularities by calculating the ration between the major and minor axis. Finally, the droplets' heights were measured with a 3D optical profilometer (S neox SENSOFAR) equipped with a 150× confocal objective (Figure 15b).

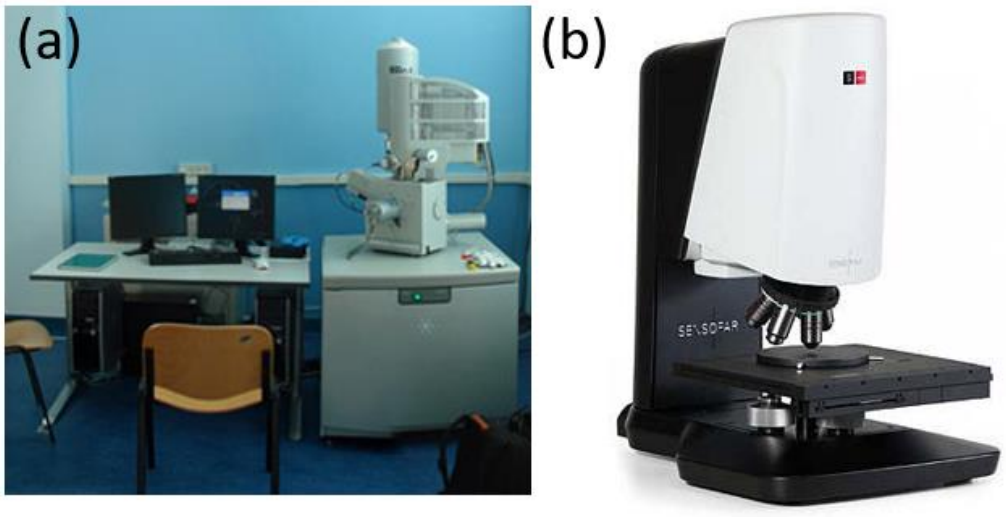

Figure 15: (a) FEI Inspect-F field emission gun scanning electron microscope (FEG-SEM) in Nanofacility Piemonte at INRiM and (b) 3D optical profilometer S neox SENSOFAR.

The lamellar organization in ordered structures was expressed quantitatively by means of correlation length (ξ). This value indicates the average grain size of an ordered domain of contiguous lamellae over a definite planar orientation. The ξ measurement was performed following the originally proposed method by Harrison *et al.*, [67]. The procedure consists of selecting several SEM images with a magnification sufficient that the image size is about 17 times the ξ and with sufficient resolution to keep an optimal nm/pixel ration. Then, the local orientation field at each point was computed by processing the SEM images [68]. A Matlab routine was then used to determine the autocorrelation function as reported in literature [69,70] and applied to the SEM images taken from different regions of the samples to extract the mean ξ value.

1.4.6 Fluorescence lifetime measurement setup

The schematics of the fluorescence lifetime spectroscopy setup is shown in Figure 16. The laser source employed in this setup is a Tsunami from Spectra-Physics that produces 10 ps laser pulses at 490 nm with an 80 MHz repetition rate and directed to a beam expander formed by the lenses $f1$ and $f2$ to tune the laser collimation. The pulses are then focused on the sample by a 20x objective after being reflected by a beam splitter (BS). Double side imaging was possible by positioning the samples over a microscope stage, allowing from one side white

light imaging with a Nikon 100 × 0.95 NA objective. On the other side, the laser passes through a Nikon 20 × 0.40 NA allowing both for laser focus on the sample surface and collection of the fluorescence. The laser was injected into a Princeton Instruments Acton SpectraPro SP-2300i monochromator (1200g/mm grating with a 0.1 nm resolution) after filtration of reflected laser by a FEL 550 from Thorlabs. Eventually, time-resolved fluorescence decay was measured by Hamamatsu universal streak coupled with a CCD.

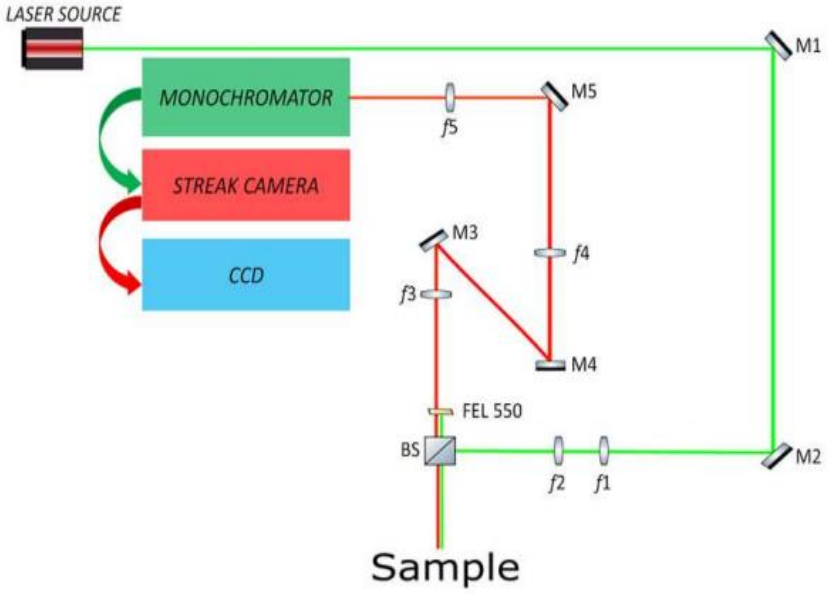

Figure 16: Schematics of fluorescence lifetime decay measurement setup. Adapted from [2].

1.4.7 Simulations

RCWA-based code was employed to calculate the reflectance maps with EMA assumption conditions [23]. The estimation of the optical response in terms of Purcell factor was simulated by commercial software Comsol Multiphysics 5.2, which exploits the Finite Element Method (FEM). A 2D symmetric model with a semi circumference of 10 μm as domain for the calculation of both the electromagnetic field distribution and the radiated power of a photon source in proximity to our lamellar HMM was designed. A frequency sweep analysis was performed to evaluate the spectral response of the material. The photon source is represented by a vertical dipole with a pseudo magnetic current of $8 \cdot 10^{-8}$ V flowing in a point at the desired height for the dipole, with point coordinates r = 113 nm, z = 5 nm + h. where h is the height of the simulated metamaterial. The

radiative power was estimated by integrating the Poynting vector along a flowing magnetic current through a 160 nm radius sphere. Figure 17 shows a schematic of the model.

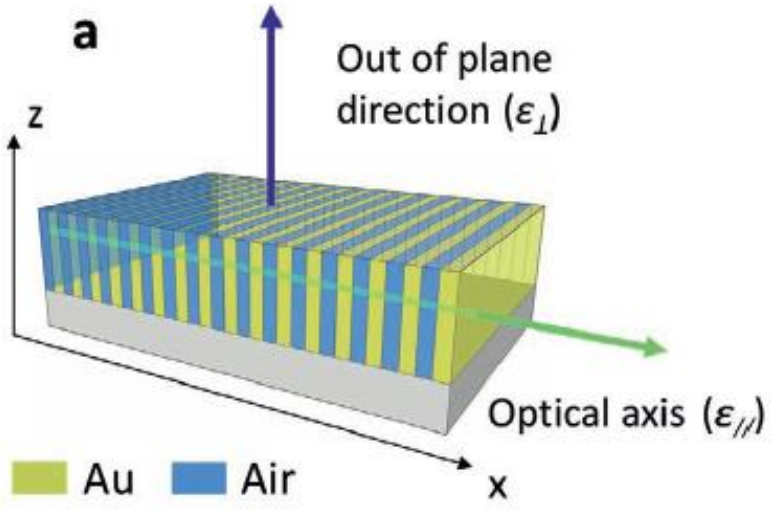

Figure 17: Schematics of a 2D lamellar Au-Air HMM with in-plane optical axis and the relative permittivity components in perpendicular ($\varepsilon_{\parallel}$) and parallel ($\varepsilon_{\perp}$) orientation to the optical axis. Adapted from [2].

The geometrical configuration of the simulated HMM consist of alternated Au lamellae with lateral width of 19 nm on top of a glass substrate with air gaps of the same lateral dimensions. The refractive indexes used for air and glass were 1 and 1.45, respectively. The Au refractive indexes were measured by optical ellipsometry of a 20 nm thick continuous Au layer deposited on Si substrate. With these geometrical configurations the Purcell factor was then estimated by dipole frequency sweeps between 500 nm and 800 nm at different lamellae heights and different dipole-HMM distances in order to find the best conditions for the highest Purcell factor value.

1.5 Results and Discussion

There is a wide literature concerning the preparation of nanostructures for optical applications by exploiting the self-assembly process of BCPs [71–74]. BCP, however, when deposited on a flat surface, are characterized by the intrinsic stochastic nature of their self-organization which leads to disordered nanostructures. The lack of any preferential orientation and large-area ordering, represents one of the bottlenecks to their practical implementation to large-scale

manufacturing of optical and electronic devices. The fabrication of perfectly aligned periodic nanostructures by self-assembling materials represents one of the key factors that the industry is currently seeking after for the production of devices with even smaller features and in a cost-effective manner.

By inducing the dewetting process of thin BCP films on pre-patterned substrates, different research groups demonstrated the feasibility to fabricate highly ordered BCP nanostructures, by taking advantage of the extensive optimization of the various processing parameters as annealing conditions, substrate functionalization and BCP film thickness [75–77]. A great control on the nanofeatures' orientation and long-range ordering was achieved by means of surface tailoring approaches by using pre-patterned substrates [78,79]. The main drawback of the dewetting-based BCP nanopatterning however, is represented by the intrinsic nature of the dewetting process that occurs only for ultrathin (h < 10 nm) polymeric film thicknesses, limiting as a consequence, the preparation of self-assembled nanostructures with high aspect ratio [80]. Strong alignment of self-assembled nanostructures was reported on thick BCP films with local thickness gradient in the near-edge regions of the polymeric film induced by tailoring the casting conditions. The lamellar and cylindrical nanofeatures were preferentially oriented perpendicularly to the film edge under specific geometric constrains (contact angle θ >3−5° and h > 500 nm) following the so-called "geometrical anchoring" phenomenon [81,82]. These constrains however, impose a low defect annihilation rate for h < 500 nm. Other alternatives to improve the defect annihilation rates are represented by the blending of BCPs with homopolymers, random copolymers or even other BCPs with lower molecular weights [83,84]. Of particular importance is the BCP blending with low molecular weight homopolymers of the constituent blocks. BCP/homopolymer ternary blends enable a substantial increase of the lateral ordering of the nanofeatures and a thermally activated dewetting phenomenon of thicker films that leads to perfectly aligned nanostructures in a single-grain configuration, representing therefore ideal templates for the fabrication of HMM with in-plane optical axis. However, the overall reduced effective transition glass temperature (T_g) [85] of the ternary blends may affect the segregation stability with negative effects in the self-assembly process which leads to a loss of the nanostructure morphology at the typical annealing conditions. Therefore, it is essential to assess the thermal stability of ternary blends, in comparison to the un-blended BCPs, in order to optimize the processing conditions while preventing thermal damage.

In this section, the development and optimization of the bottom-up fabrication of hyperbolic metamaterial with in-plane optical axis, based on self-assembly of block copolymers, will be discussed. The fabrication strategy of the HMM templates based on the self-assembly process of BCP/homopolymer blends will be illustrated. The self-assembly process represents a fundamental step in the fabrication of HMM since it affects the structural and optical properties of the resulting material. For these reasons a comprehensive understanding of the nanopatterning process as well as a detailed characterization of the BCP nanostructures is essential to fully understand and optimize the optical behavior of the HMM. Afterwards, complete optical characterization of the emissive properties of single-photon emitters coupled with the BCP-based HMM will be assessed by fluorescence lifetime decay measurements and supported by numerical modeling.

1.5.1 Block copolymer blending

In order to assess the thermal stability of BCP/homopolymer ternary blends in comparison to the un-blended BCPs, two sample sets of symmetric PS-*b*-PMMA with M_n = 66 kg mol^{-1} and DPI = 1.09 were prepared. The first set, labeled neat BCP, was prepared by dissolving 18 mg of BCP in 2 ml of toluene. The second set, labeled blend BCP, was prepared by dissolving 9 mg of the same BCP with 4.5 mg of low-molar-mass PS (M_n = 3.1 kg mol^{-1} and DPI = 1.09) and 4.5 mg PMMA (M_n = 3.9 kg mol^{-1} and DPI = 1.18) homopolymers in 2 ml of toluene to avoid the formation of microemulsions or microphase-separation [86] while maintain the lamellar morphology. Both solutions were spin-casted on Si substrates previously functionalized with a 7 nm random copolymer FSM7 grafted by RTP at 250 °C for 900 s using a heating rate of 18 °C s^{-1}. The spin-casting conditions were adjusted to deposit a final BCP film thickness of 40 nm.

Both BCP sets were then thermally annealed by RTP for an annealing time (t_a) ranging from 30 to 1200 s and for an annealing temperature (T_a) range from 210 to 330 °C. For each annealing run, one neat and one blend BCP samples were processed simultaneously in order to suppress any stochastic effect related to minor differences on the thermal conditions. After the thermal annealing, the resulting nanoscale self-assembly process and the film topography were analyzed by SEM and optical profilometry. In Figure 18 and Figure 19 all the SEM micrographs relative to the neat and blend BCPs under the aforementioned RTP conditions are reported.

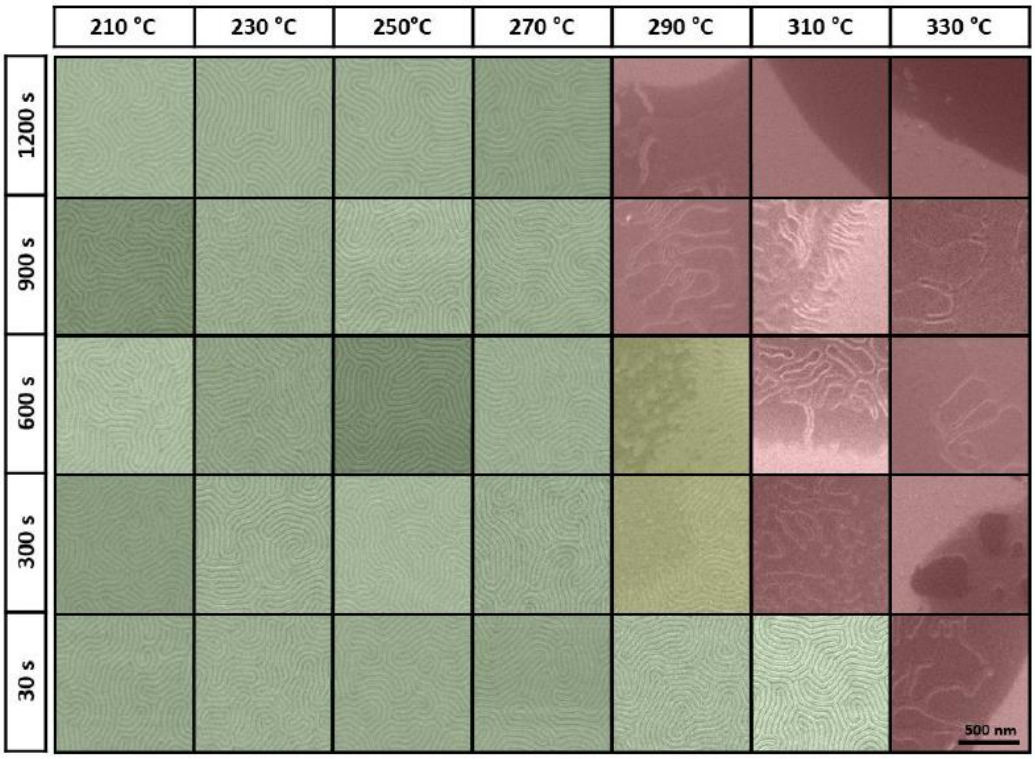

Figure 18: SEM micrographs of neat BCP after RTP annealing performed at different annealing times and temperatures. Green micrographs represent the thermal conditions for continuous films; yellow micrographs for inhomogeneous films and red micrographs for the inhomogeneous films with loss in lamellar morphology. Adapted from [1].

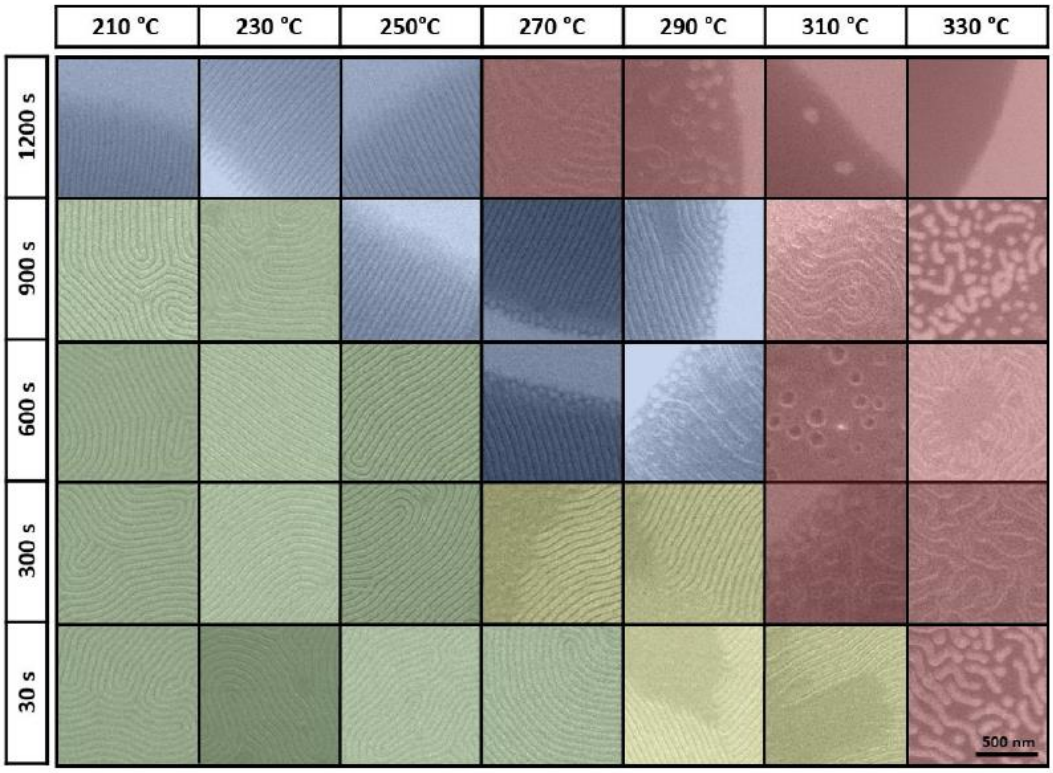

Figure 19: SEM micrographs of BCP/homopolymer blends after RTP annealing performed at different annealing times and temperatures. Green micrographs represent the thermal conditions for continuous films; yellow micrographs for inhomogeneous films; red micrographs for the inhomogeneous films with loss in lamellar morphology and blue micrographs for dewetted films. Adapted from [1].

The topographical assessment of the BCP thin films enabled the definition of a stability diagram for both neat and blend BCPs as a function of the thermal annealing conditions. As reported in Figure 20, the differences in topography and nanoscale self-organization, define four stability conditions at different T_a and t_a for the two sample sets. When the surface is flat and continuous (Figure 20a), we refer to the polymeric film as stable (green triangles in Figure 20c,d). In contrast, if the film shows discontinuities and inhomogeneities (Figure 20b), then we refer to these annealing conditions as unstable. Under the unstable conditions the films can be further differentiated into early formation of inhomogeneities, film dewetting and loss of nanostructured lamellar morphology (yellow, blue and red annealing conditions respectively in Figure 20c,d).

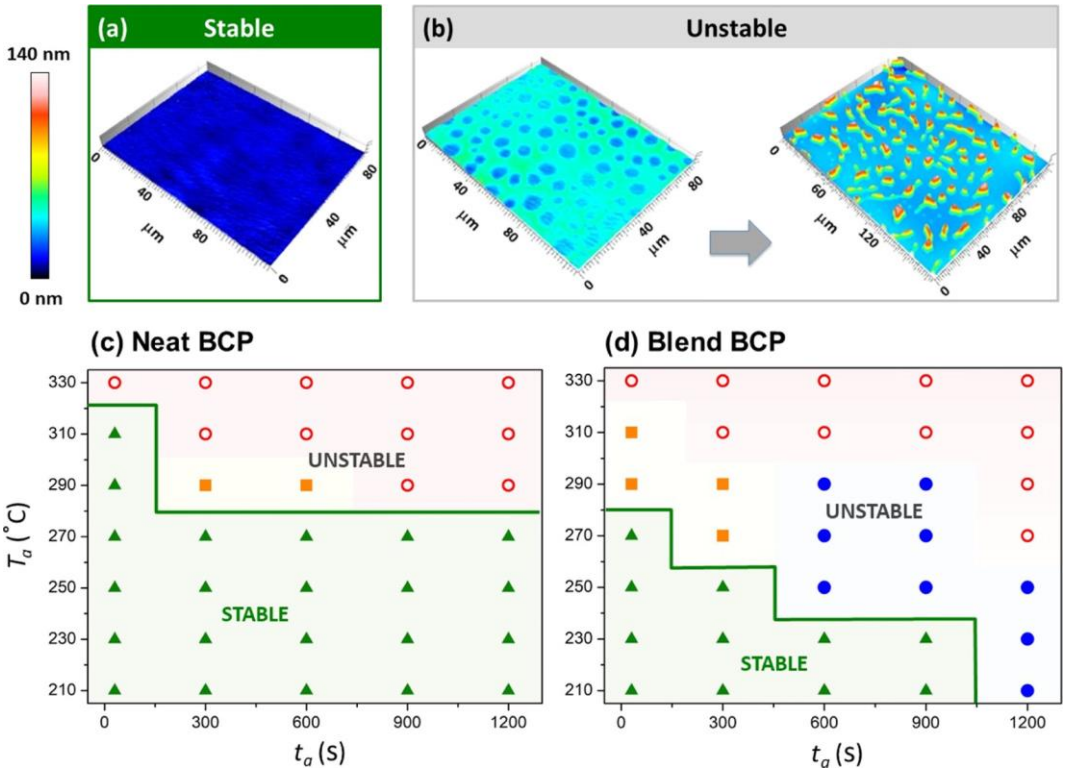

Figure 20: (a) Stable and (b) unstable BCP thin film conditions measured by optical profilometry. (c,d) Morphological and thermal BCP thin film stability diagram at different RTP annealing temperatures and annealing times for neat and blend BCP respectively. In these stability diagrams different stability conditions are highlighted: green area represent the thermal annealing temperature (T_a) and time (t_a) for continuous and homogenous film defined as stable conditions; the yellow squares define the thermal conditions for early-stage topographic discontinuities; the blue circles indicate the annealing conditions for BCP film dewetting with self-assembled nanostructures and the red circles for the complete loss of any nanostructured morphology. Adapted from [1].

Clear differences are visible on the thermal stability when comparing the neat to blend BCPs. The thermal conditions for a stable and homogenous film span for a very wide range of annealing times and temperatures. In neat BCPs the stability conditions are met even for long RTP annealing (1200 s) up to 270 °C. The annealing temperature can also be extended to 310 °C for very short (30 s) annealing times preventing any film disruption. Moreover, self-assembled nanostructures are already visible at relatively low temperatures (210 °C) and for very short annealing times (30 s). Film discontinuities of the polymeric film start to appear at 290 °C for 300 and 600 s, anticipating the complete film disruption and total loss of the lamellar features for higher temperatures (red circles in Figure 20c). In contrasts, for blend BCPs the stability diagram shows strong differences

compared to the neat one. The main difference is represented by a substantial reduction of the processing conditions in terms of annealing times and temperatures for a continuous and homogeneous film. These conditions do not exceed the 270 °C and the 900 s before encountering into film instability. For a given annealing time, the presence of low molecular weight homopolymers reduces the film stability of about 40 °C. However, under specific conditions beyond the stable region, a thermally activated dewetting process of the thin film occurs leading to micrometric droplets in which inside highly ordered nanostructuring can be observed (blue SEM micrographs in Figure 19). The overall reduction of the stable conditions of blend BCPs may be attributed to a lowered effective glass transition temperature (T_g) of the ternary blend when compared to the same BCP in absence of any homopolymers [85].

In order to assess whether the film topography and nanostructuring are impaired by the polymeric thermal stability, thermogravimetric analysis (TGA) was performed on the neat and blend BCP solutions. Specifically, TGA coupled with a gas chromatograph and a mass spectrometer, allowed the thermal degradation detection of styrene (S) (mass peaks at m/z = 104) and methyl methacrylate (MMA) (mass peaks at m/z = 100). No significant differences are noted on the MMA evolution of the neat and blend BCP solutions, with onset degradation at 330 °C, reaching a maximum value at 380 °C (blue dashed line) as shown in the TGA-GC-MS chromatogram in Figure 21. The S evolution, however, shows clear difference for blend BCP when compared to the neat BCP. The loss profile of S in neat BCP is quite wide, in a temperature range of 150 °C with maximum peak at 450 °C, whereas for blend BCP the loss profile splits into two peaks while still within the same temperature range of neat BCP. This can be attributed to the different thermal stabilities of the S monomer in PS homopolymer and in the corresponding PS block in the BCP. These data clearly agree with those reported in literature where the thermal degradation of PS-*b*-PMMA, PS, and PMMA at these thermal conditions follows an unzipping depolymerization mechanism [88]. However, since the temperature conditions at which the TGA analyses were conducted are much higher than those of BCP processing, we can conclude that the polymer thermal stability does not affect the final self-assembled morphologies.

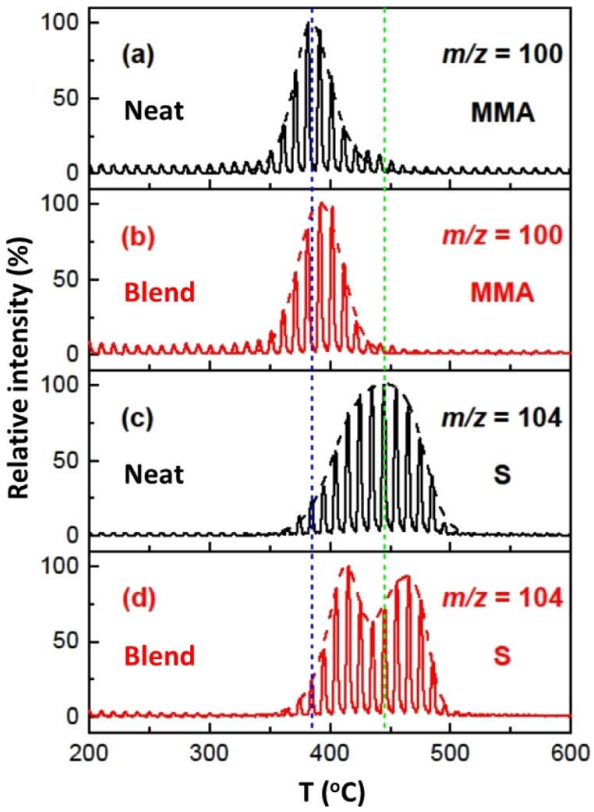

Figure 21: Neat and blend BCP TGA−GC−MS chromatograms with (a,b) reference to the mass peaks of MMA at *m*/*z* 100 and (c,d) to the mass peak of PS *m*/*z* 104. Blue line indicates the maximum loss temperature of MMA and the green line indicates the maximum loss temperature of S. The analyses were conducted with a heating rate of 20 °C/min under a nitrogen atmosphere, with a collection of the evolved gas from TGA every 30 s. The resolution of the gas profiles is 10 °C. Adapted from [1].

Once defined the thermal stability conditions of both neat and blend BCP systems to achieve homogeneous films, the next step regarded the assessment of the influence of homopolymers on the long-range ordering of the BCP blends. In this regard, the ξ values were extracted from the SEM micrographs of both neat and blend BCP samples under the stability conditions. In Figure 22, the ξ values related to different T_a are plotted as a function of t_a for both neat and blend BCPs. In neat BCP (Figure 22a) the already low initial ξ values (70 – 100 nm) for short t_a at any given temperature, are characterized by a slow growth exponent (τ) ranging from τ = 0.02 (for T_a = 210 °C) to τ = 0.06 (at T_a = 270 °C), reaching a maximum ξ of 130 nm at t_a = 900 s and T_a = 270 °C. The slow increase on the lateral ordering of neat BCPs along with the annealing temperature is confirmed by the low growth exponent (< 0.1) reported in literature for thermally treated BCPs in RTP apparatus or standard furnace at t_a > 100 s and T_a < 270 ° [87–89].

On the other hand, the ξ in blend BCPs follows a completely different evolution (Figure 22b).

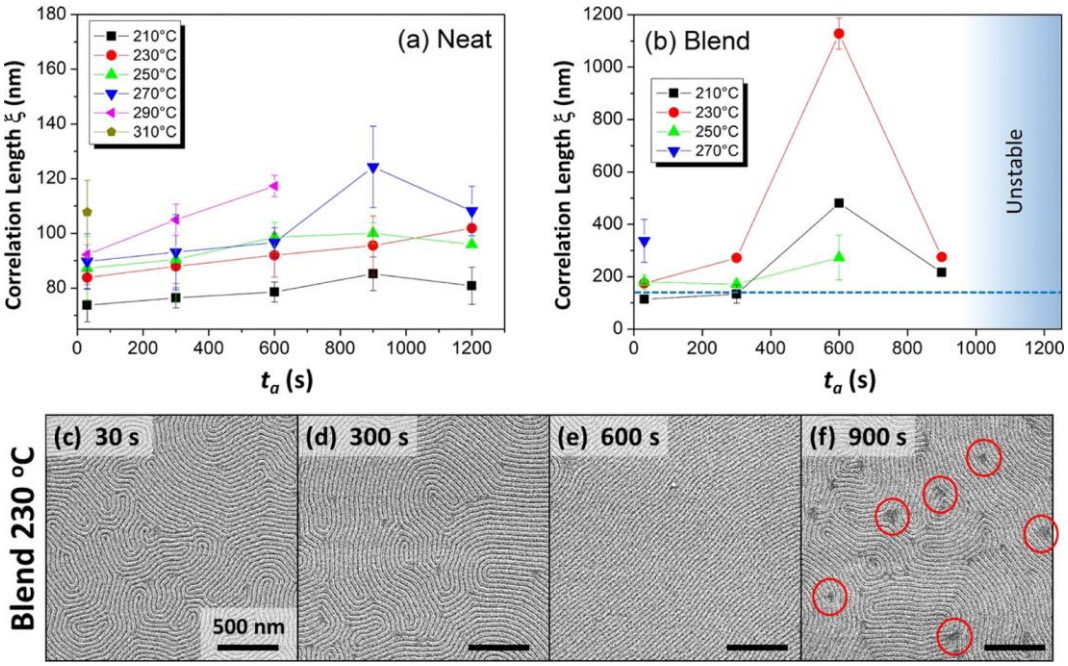

Figure 22: Correlation length evolution of (a) neat BCP and (b) blend BCP at different annealing times (t_a) and temperatures (T_a). The blue dashed line in (b) represents the highest ξ achieved by neat BCP and used as a reference for comparison purposes. (c-f) SEM micrographs illustrating the lateral ordering evolution of blend BCP for different t_a at 230 °C. The red circles highlight the defect areas of lamellar structures after long annealing treatments. Adapted from [1].

At very short t_a, the ternary blends already show ξ values around 200 nm, that exceed the highest achievable by the neat BCPs. The overall increased lateral length ordering at any given T_a reaches its highest peak after 600 s of RTP treatment, almost doubling for heating ramps at 210 °C and 250 °C. The most interesting trend is illustrated by the lateral ordering evolution at 230 °C (Figure 22c-f). In this case, the ξ reaches a maximum value of 1120 nm after 600 s of annealing, which corresponds to one order of magnitude higher when compared to the highest ξ observed for a neat BCP. After reaching the highest ξ value, a drastic decrease of the lateral ordering is observed for longer T_a (900 s), dropping down at around 200 nm. As illustrated in the red circles in Figure 22f, the progressive reduction on the lateral ordering is accompanied by an increase in local defect density represented by some dark areas, suggesting that under these conditions, the BCP film is approaching an order-disorder transition [85].

The strikingly high lateral length values obtainable by simple BCP/homopolymer blending at relatively low temperature conditions, open the opportunity for an easy fabrication of aligned periodic nanostructures by means of BCP lithography. For the fabrication of HMM however, high ξ values, do not necessarily imply the possibility to directly implement the BCP nanostructures without any further alignment into defect-free patterns. In fact, although the average grain sizes of lamellar nanostructures oriented on the same direction might be at the micrometric scale (as indicated by ξ = 1120 nm for blend BCPs), the 2D multigrain nature of the overall self-assembled polymeric film do not show any preferential orientation over the entire length scale of the substrate (Figure 23a,b). One of the methodologies exploited to propagate the BCP alignment into defect-free structures is represented by implementing the self-assembly process into chemical or topographical guiding patterns by means of directed self-assembly (DSA) [90]. In DSA the perfect alignment of the BCP nanostructures can be achieved when the geometric dimensions of guiding patterns are commensurable to the correlation length of the BCP self-assembled on a flat surface [91].

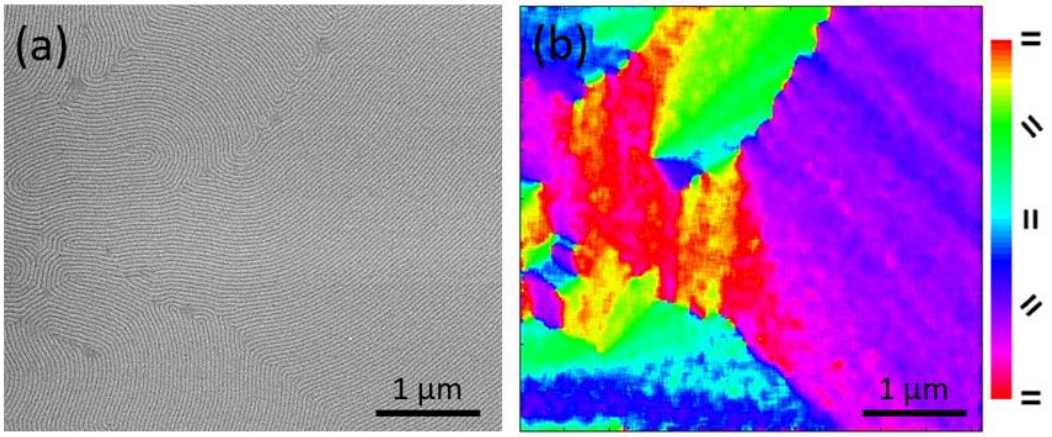

Figure 23: (a) Wide view SEM micrograph of blend BCP treated at T_a = 230 °C for t_a = 600 s and (b) relative colour orientation map describing the lamellar orientation inside the lamellar grains.

To verify the propensity of blend BCPs to align into perfectly ordered nanostructures, we implemented the self-assembly process into topographically defined linear trenches with different widths, ranging from 0.9 to 5 µm. The linear trenches were fabricated on silicon substrates by laser writer lithography in combination with reactive ion etching for a total depth of 200 nm, as described in the methods section. In Figure 24a,b are reported the SEM micrographs of both

neat and blend BCPs self-assembled over a flat surface and in Figure 24c,d the same BCPs self-assembled inside the graphoepitaxy-defined trenches. For neat BCPs the maximum ξ value (130 nm) obtained by RTP at 270 °C for 900 s, is much lower that the trench width (W = 3.5 μm), therefore no appreciable long-range propagation of the lamellar alignment is impaired by the guiding trenches. To support this consideration, the ξ of neat BCP measured inside the trenches is the equal to that one measured on a flat surface (Figure 24c). On the contrary, for blend BCPs, a sensible enhancement of the correlation length is noted when self-assembled inside the guiding patterns (Figure 24d). The long-rage ordering propagation impaired by the guiding patterns extends the lamellar alignment from one side of the trench to the other over approximately 3 times (3.5 μm) the ξ over a flat surface. The perpendicular alignment of the lamellar features with respect to the trenches is determined by the RCP layer grafted on the side walls of the trenches. Despite the sensible enhancement of the long-range ordering propagation, it should be noted that a perfect defect-free lamellar alignment is prevented by the presence of some dislocations, junctions and bridging.

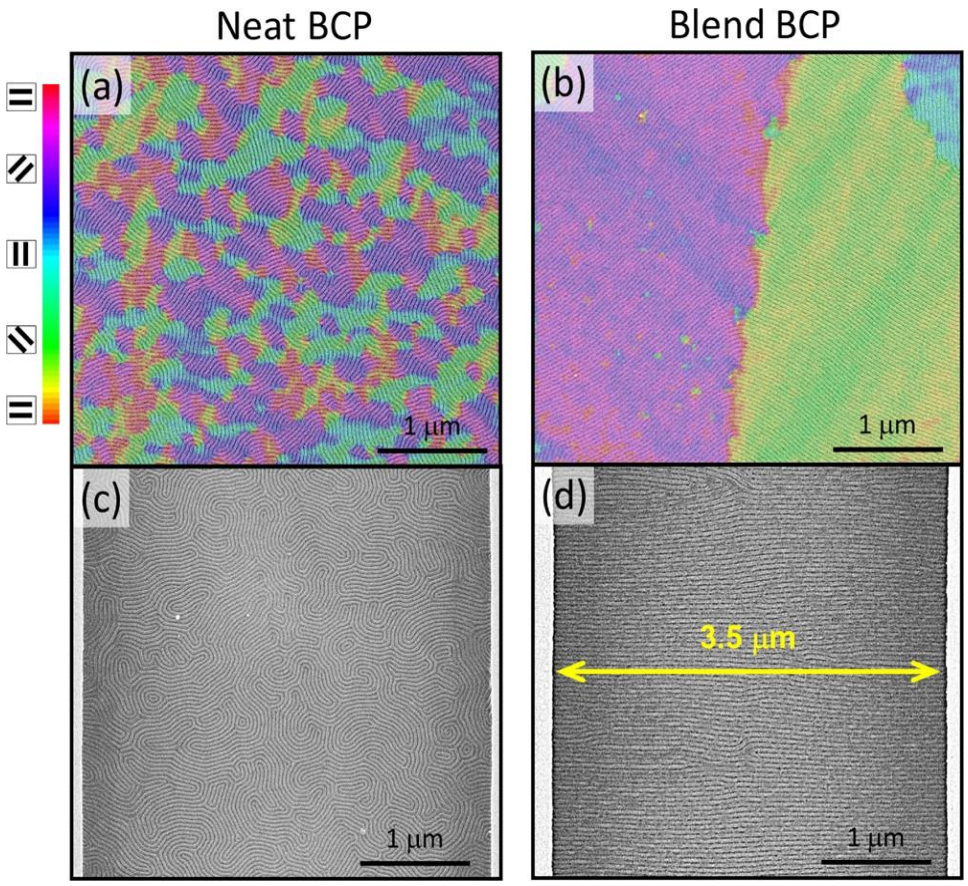

Figure 24: False color orientation maps overlapped to the corresponding SEM images of lamellar neat (a) and blend (b) BCPs over a flat substrate treated by RTP at T_a = 270 °C and t_a = 900 s and T_a = 230 °C and t_a = 600 s, respectively. SEM images of the same neat (c) and blend (d) BCPs inside 3.5 µm-wide trenches. Adapted from [1].

Once assessed the self-assembly process on stable films, we focused on the characterization of the BCP films in unstable conditions. The AFM morphological characterization of the polymeric films, defined as "early-stage topographic discontinuities" (yellow squares in Figure 20c and 20d), reveals an uneven film thickness across the sample with the presence of holes over the RCP layer (Figure 25a). These holes extend for several micrometers, gradually increasing the film thickness up to 70 nm (Figure 25b). Surprisingly, very well aligned lamellar nanostructures are visible along the thickness gradient imposed by the holes (Figure 25c,d). With a closer look at the edges of the holes, the AFM micrographs show two different film behaviours along the parallel or perpendicular direction to the thickness gradient (Figure 25e,f). Starting from the center of the hole, the film is flat in the perpendicular direction to the film gradient, whereas a continuous thickness increase is noted in the parallel direction along with the presence of

highly aligned lamellar nanostructures guided by the “geometrical anchoring” effect [82].

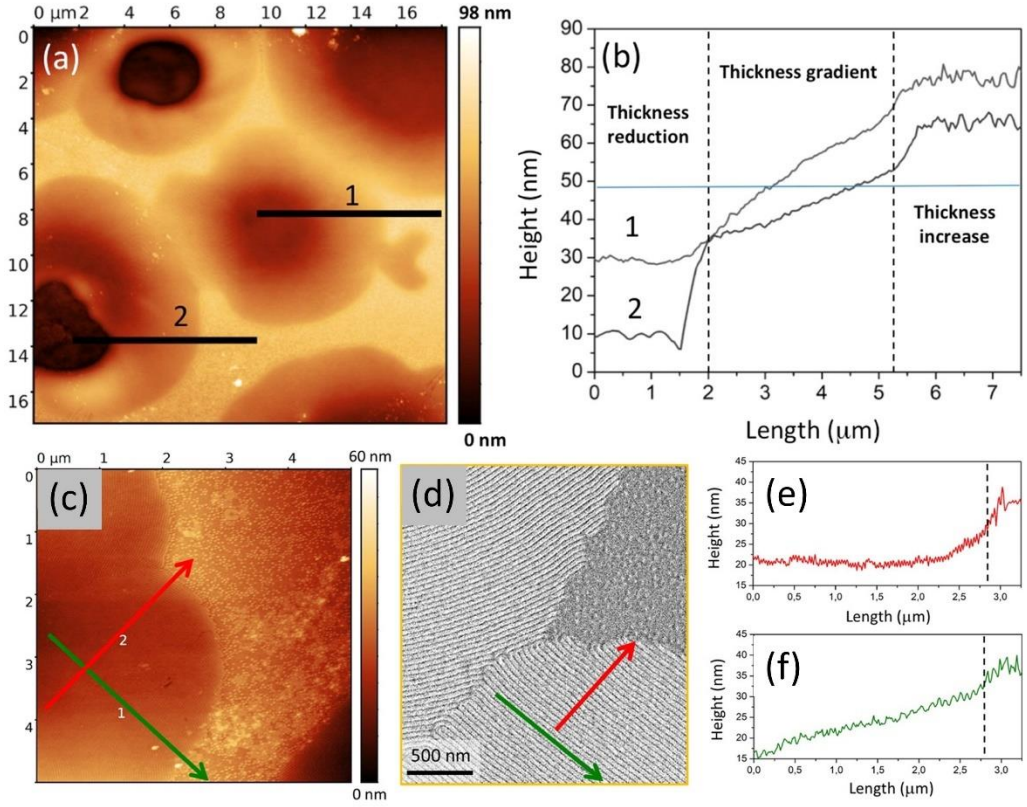

Figure 25: (a) Surface topography analysis by AFM of a blend BCP under unstable conditions (T_a = 290 °C and t_a = 30 s) and (b) relative profiles of the hole thickness gradient extracted from the black lines 1 and 2 in (a). Higher magnification (c) AFM and (d) and SEM images to better illustrate the geometrical anchoring effect. (e,f) Height profiles of film holes in perpendicular and parallel direction to the thickness gradient, respectively. Adapted from [1].

Interestingly, the lamellar morphology drastically changes once reached the highest film thickness and new circular features with 28 nm of diameter appear (Figure 26a,b).

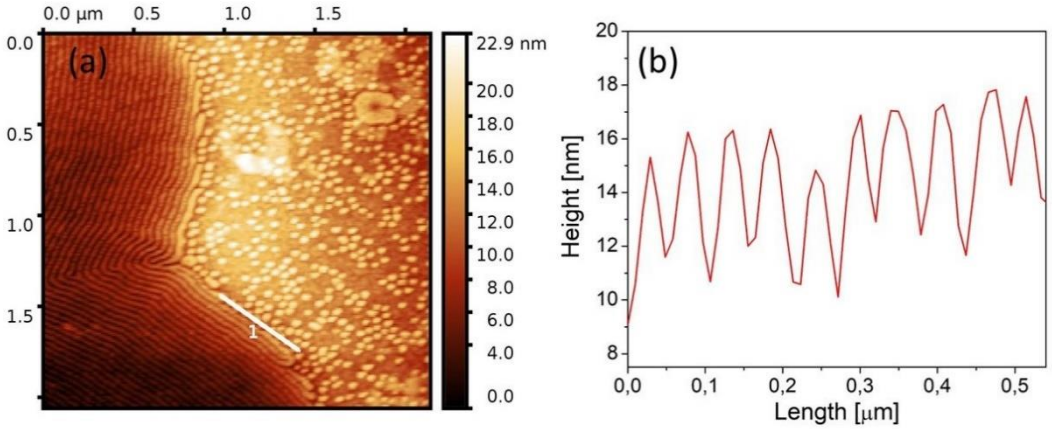

Figure 26: (a) AFM micrograph and (b) relative height profile of the circular features formed on the top of the film at the highest thickness. Adapted from [1].

By extending the thermal annealing conditions at higher T_a and longer t_a, both neat and blend BCP undergo a dewetting phenomenon. In particular, we can identify two different kinds of dewetted features. The first kind, defined as high temperature dewetting, is observed for both neat and blend systems and typically occur at T_a higher than 310 °C and t_a longer than 900 s and are characterized by the absence of any nanostructures as seen in Figure 27a. These dewetted features are indicated by the red circles in the stability diagram in Figure 20c,d. The second kind of dewetted features, defined as low temperature dewetting, are observed in blend BCP only. Under specific annealing temperature and time conditions, blend BCP films undergo a thermally activated dewetting process that leads to micrometric droplets in which inside the lamellar nanostructures are preserved (Figure 27b). Compared to neat BCP, in which the low temperature dewetting is reported for ultra-thin films (< 10 nm) [92,93], in blend BCP this process is observed starting from films with thickness of 40 nm. This clearly confirms an overall stability reduction imposed by the presence of low-molecular weight homopolymers when blended with BCPs.

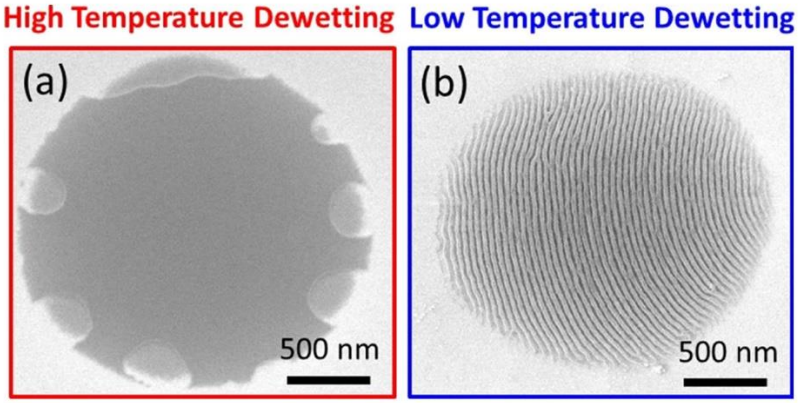

Figure 27: SEM images of a blend BCP under (a) high temperature dewetting conditions (T_a = 310 °C and t_a = 1200 s) and (b) low temperature dewetting conditions (T_a = 250 °C and t_a = 1200 s). Adapted from [1].

In order to access the dewetting mechanism followed by neat and blend BCP at high and low temperature, two-dimensional Fourier transform (2D-FFT) of the optical profilometer images at low magnification were applied in order to extract intensity rings related to in-plane prominent lengths λ. Depending on the λ evolution with respect to annealing time and film thickness, one can distinguish three different dewetting mechanism [94]. The complete procedure for the λ calculation is described in Figure 28. For continuous and homogeneous films in stable conditions (T_a = 250 °C; t_a = 300 s) as in Figure 29a, sporadic dewetted features appear due to surface contamination *e.g.,* dust particles. This can be referred to as a heterogeneous nucleation mechanism in which no prominent λ are detectable. Under low temperature dewetting conditions (T_a = 250 °C; t_a > 300 s) (Figure 29b) however, the PSD calculation reveal λ values in the range from 10 to 20 μm suggesting a spinodal dewetting mechanism. In contrast, at higher temperature conditions (T_a > 310 °C) appreciable λ values were detected only for annealing times longer than 600 s for both neat and blend BCPs (Figure 29c-e). Interestingly, for these sample, the λ values are around three times higher than those calculated for low temperature conditions (Figure 30a).

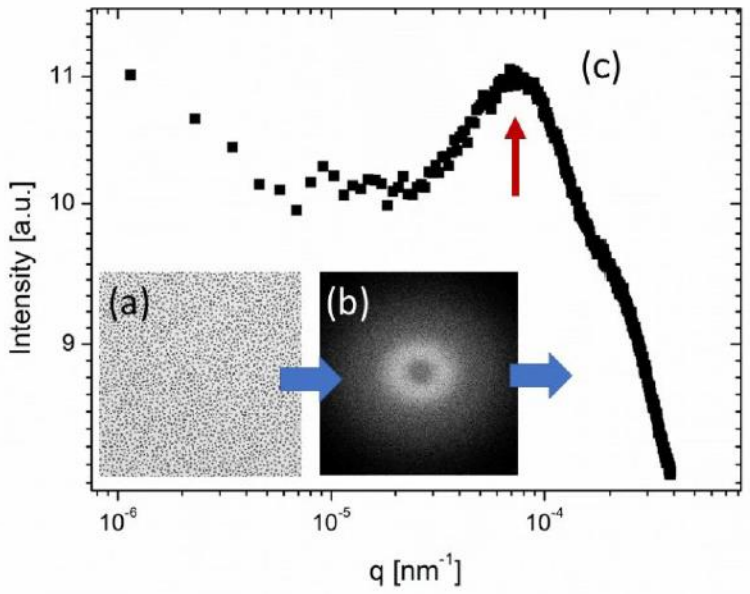

Figure 28: Power spectral density function (PSD) calculation from optical profilometer images procedure. (a) 2D FFT is applied to the topographical image of dewetted droplets followed by (b) radial averaging of the intensity distribution in reciprocal space. (c) The generated PSD. Prominent in-plane lengths (λ) can then be calculated by PSD peak identification (red arrow), corresponding to the mean droplet distance. Adapted from [1].

Deeper insights into the dewetting spinodal mechanism followed by blend BCP films are given when the λ values are plotted as a function of the polymeric film thickness. Figure 30b shows very similar increasing λ values for blend BCPs annealed at 250 and 310 °C, with growth exponents ε of 1.24 and 1.26 respectively, suggesting that at both temperatures the BCP films follow the same dewetting mechanism independently to the presence or not of the lamellar morphology. As reported in literature [95], the nanometric morphology in self-assembled BCPs impairs an additional stabilizing effect preventing any film disruption for thickness $h > 2R_g$ (R_g is the radius of gyration). In BCP ternary blends, the presence of dewetting phenomenon observed for $h > 2R_g$, indicates that the low molecular weight homopolymers sensibly reduce the stabilizing effect of the lamellar nanostructures, leading to ε values that are independent to the film thickness.

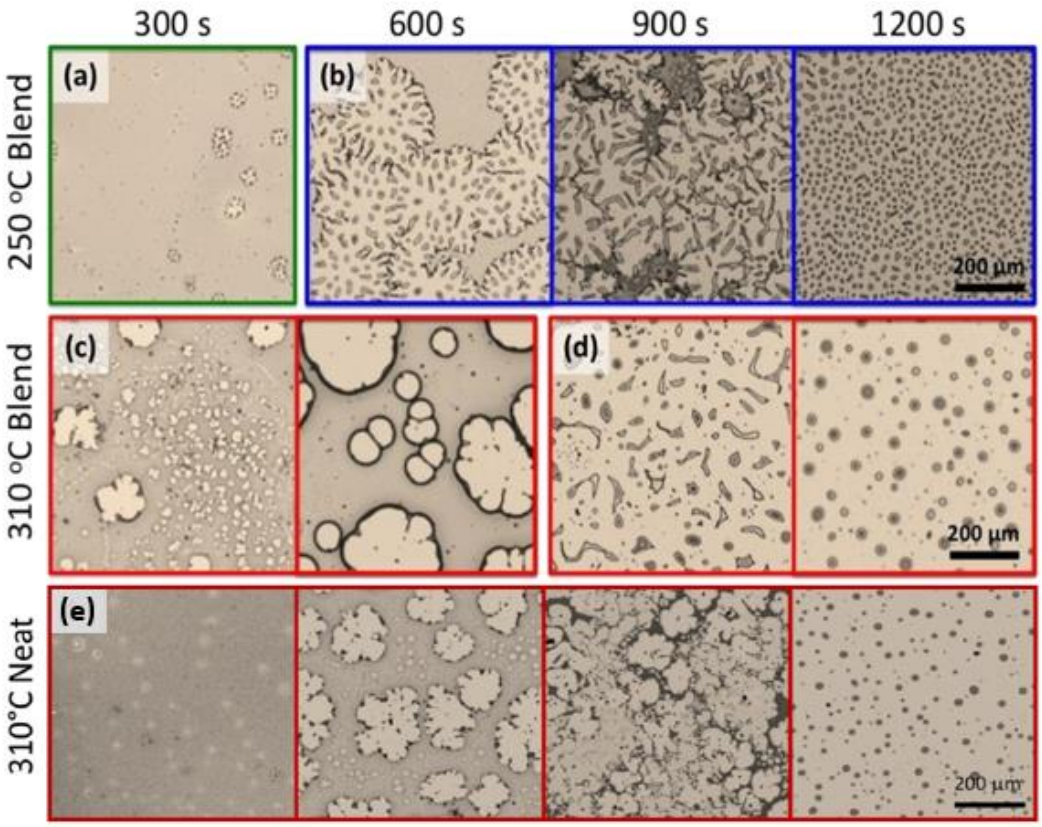

Figure 29: Large-area optical microscopy images of blend (a-d) and neat (e) BCP films under different annealing conditions used for the PSD calculation of the in-plane λ values. Adapted from [1].

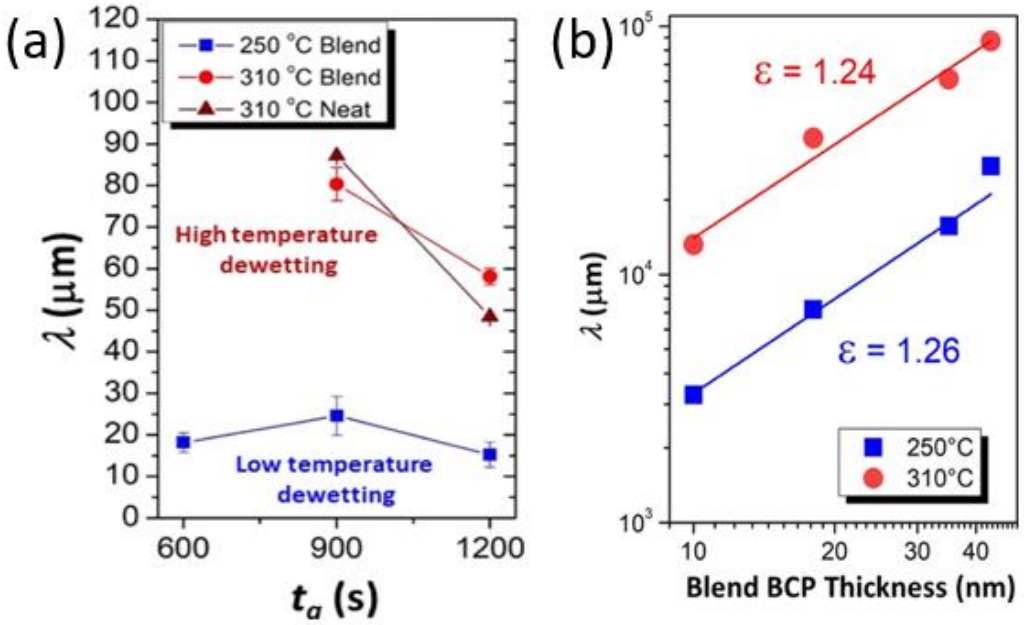

Figure 30: In-plane λ values evolution as a function of (a) different annealing times for neat and blend BCP films and (b) of blend BCP film thickness at 250 °C and 310 °C. Adapted from [1].

One of the main features of low temperature dewetted droplets is the remarkable ordering of the lamellar structures induced by the geometrical anchoring effect as shown in Figure 27b. As described by Kim *et al.* [82], at specific conditions of critical angle θ >3−5° and height h > 500 nm, the spontaneous alignment of the lamellar structures along the thickness gradient is favored by the energetic gain from the annihilation of linear defects, dislocations, and disclinations. Surprisingly, the same effect is also observable in low temperature dewetted droplets even though the AFM measurements reveal critical angles of θ = 6.5° and h < 100 nm (Figure 31a,b).

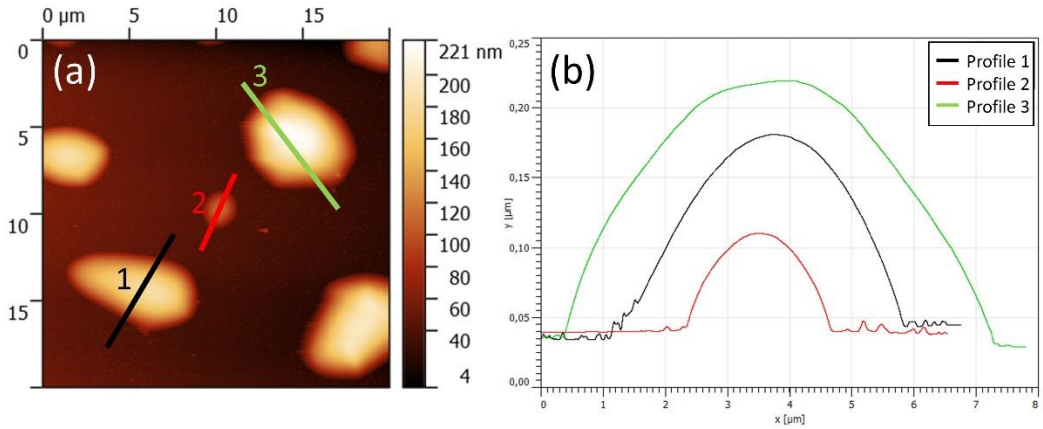

Figure 31: (a) AFM micrographs of low temperature dewetted droplets with different dimensions and (b) relative height profiles. Adapted from [1].

In order to determine whether the lamellar ordering in dewetted BCP films can be attributed to the geometrical anchoring effect or to the low molecular weight homopolymers in the blend BCPs, a direct comparison of nanoscale ordering inside dewetted neat and blend BCPs with similar geometrical characteristics is necessary. Since the low temperature dewetting process does not occur in neat BCPs, it was necessary to artificially induce a film disruption by thermal treatment of neat BCPs over topographical patterns. Figure 32 shows the direct comparison between the AFM and SEM images of low temperature blend BCP dewetted droplets (Figure 32a,b) with artificially induced dewetting of a h = 40 nm neat BCP (Figure 32c,d). Although the contact angles (θ = 6.0°) of neat BCP droplets are similar to the blend ones (θ = 6.5°), the false color orientation map reveals a multidomain nature of the self-assembled lamellae, thus indicating that lamellar ordering is not enhanced when outside the geometrical conditions imposed by the geometrical anchoring effect (h < 500 nm). On the contrary, the highly ordered lamellar structures in blend BCPs droplets indicate the ability of low molecular weight homopolymers to extend the geometrical constrictions of the geometrical anchoring to polymeric films with lower thicknesses (h = 40 nm).

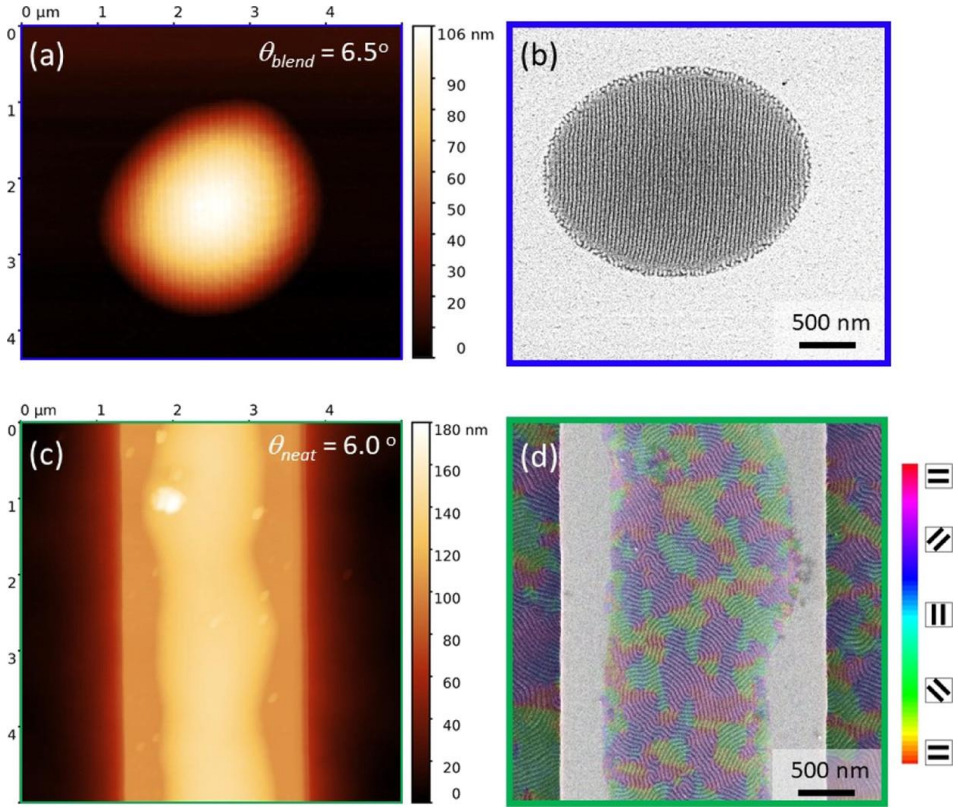

Figure 32: (a,b) AFM and SEM micrographs of a low temperature dewetted blend BCP. (c,d) AFM and SEM micrographs of dewetted neat BCP artificially induced over topographical patterns. Both neat and blend BCP were thermally processed under the same RTP conditions (T_a = 250 °C and t_a = 900 s). (d) False color map is overlapped to the respective SEM image to better illustrate the lamellar multidomain. Adapted from [1].

1.5.2 Block copolymer dewetting

Blending BCPs with low molecular weight homopolymers of the constituent blocks demonstrated to be a valid method to enhance the lateral ordering of the self-assembled nanostructures up to one order of magnitude higher than neat BCPs [1]. More interestingly, the overall reduced thin film stability imposed by the presence of the homopolymers induces thermally activated low temperature dewetting that generates micrometric droplets, in which inside one can observe a perfect alignment of the lamellar nanofeatures. The blend BCP dewetting process, therefore, represents to be a promising candidate for the realization of polymeric templates for the fabrication of HMM with in-plane optical axes. One of the main drawbacks of BCP dewetting however, is represented by the stochastic generation of droplets in a wide variety of contours and dimension randomly arrange over a surface (Figure 33a). Topographic analysis by SEM, revealed that the low

dewetting process leads to the formation of droplets with two area distributions (Figure 33b): a very broad area distribution ranging from 10 to 200 μm^2 (red columns in Figure 33b) and a narrower area distribution at sub-10 μm^2 (blue inset in Figure 33b).

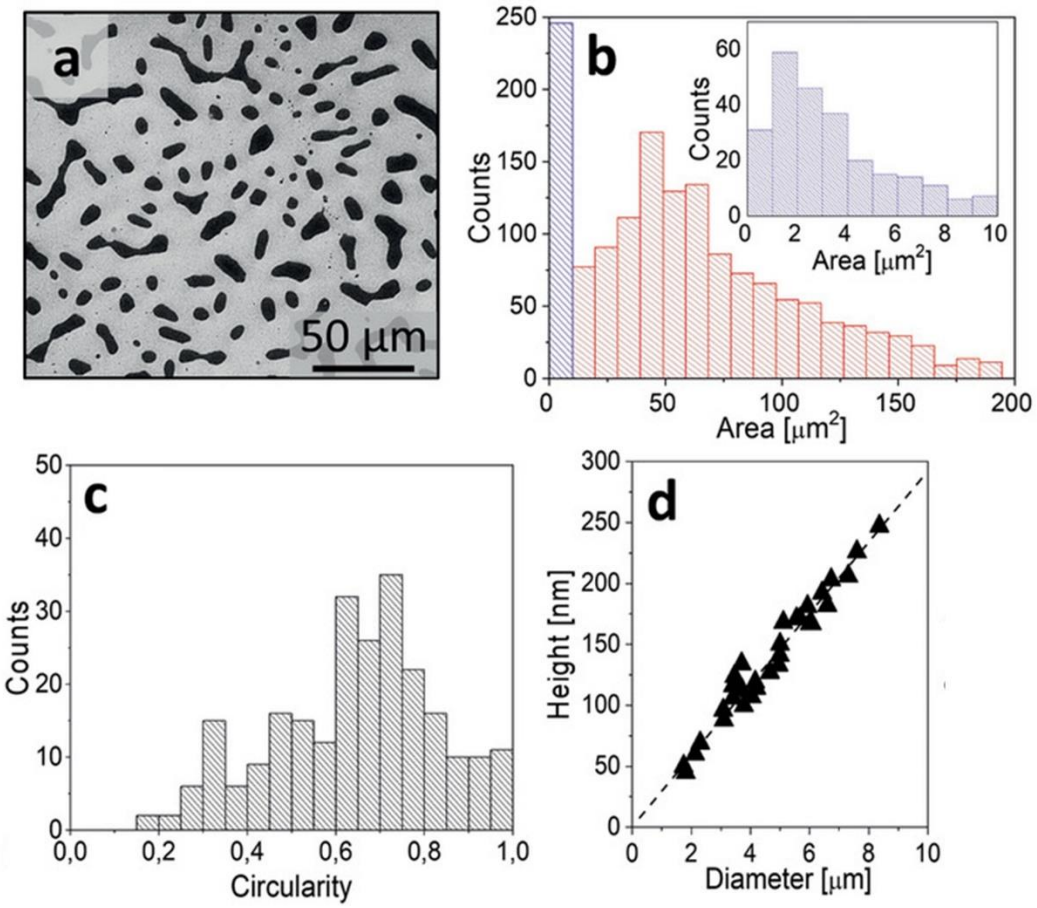

Figure 33: (a) SEM image of blend BCP dewetted over a flat surface. (b) Relative distribution of droplets' area; the inset represents the distribution for sub-10 μm^2 droplets. (c) Droplets' circularities and (d) their heights as a function of their diameter. Adapted from [2].

The stochastic arrangement of the dewetted droplets into a wide plethora of contours and dimensions is also supported by the topographical analysis by optical profilometry which reveals a wide distribution of circularities and a linear dependence of the film thickness to the their diameter (Figure 33c,d). The lack of any control over the spatial position of the dewetted droplets, along with their stochastic arrangement into a wide variety of dimensions and shapes, implies

some severe limitations into the technological exploitation of the dewetting process as a lithographic tool.

By taking into consideration the aforementioned geometrical anchoring effect [82], which describes the tendency of self-assembled nanostructure to align along a film thickness gradient, one can expect a great influence on the nanostructures ordering determined by the wide variability of the dewetted droplets. As illustrated in Figure 34a, for a wide and irregular droplet, the spontaneous perpendicular alignment of the lamellae with respect to the film thickness gradients at different edges, leads to the formation of defects on inner zones. For elongated droplets, the perpendicular orientation of the lamellae along the two opposite borders, indicated by the white arrows in Figure 34b, propagates the nanostructures alignment from one edge to the other in a defectless configuration. Similarly, in elliptical droplets the lamellar alignment propagates for the entire droplet width along the orthogonal direction of the major axis in a single-grain configuration (Figure 34c), highly desirable as a platform for the fabrication of HMMs with in-plane optical axis.

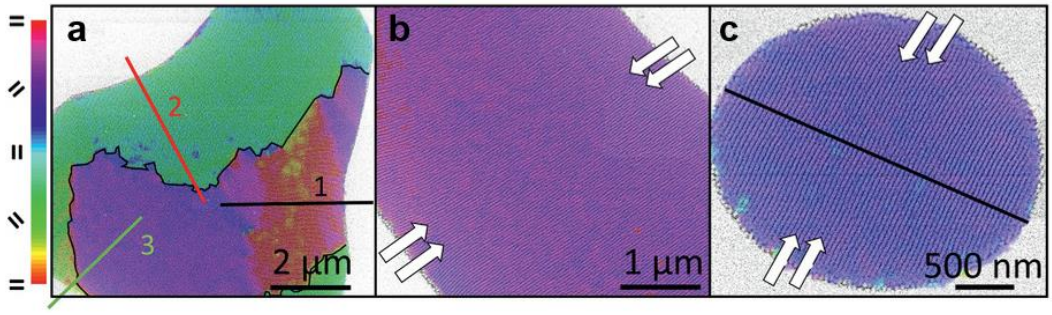

Figure 34: False colour maps superimposed on the relative SEM images of (a) irregularly shaped droplet (black, red and green lines indicate the perpendicular direction with respect to the droplet edges), (b) elongated droplet (opposite edges indicated by the white arrows) and (c) elliptically shaped droplets in a single-grain configuration. Adapted from [2].

The practical exploitation of the BCP dewetting process into the fabrication of HMMs requires the ability to control the position, dimensions and morphology on each single droplet, in order to tailor the self-assembled nanostructures into the desired configuration. Many strategies have been reported in literature to achieve this task, mainly relying into the chemical or topographical modification of substrates [96,97], microcontact and transfer printing [98]. The fabrication method of choice in our work came to the use of topographical patterns obtained by RIE over micrometric patterns defined by laser-writer lithography. This fabrication

method allows for the precise definition of the guiding template with sufficient robustness to withstand the subsequent processes into the realization of the HMM. Different patterns consisting of periodic meshes with 200 nm height and widths ranging from 5 to 50 µm, were fabricated and used as guiding templates for the subsequent dewetting process. On top of the guiding patterns with widths of 30 and 50 µm, the SEM images in Figure 35a show the formation of multiple droplets whose shapes and dimensions roughly replicate those obtained over a flat surface (Figure 35b). This indicates that the geometrical constrains imposed by the topographical patterns are not sufficient to guide the dewetted droplets into the desired positions, dimensions and morphologies. By reducing the mesh width to 10 µm, the restricted geometrical constrains induce the dewetting process into the generation of single droplets. However, high average droplet area (above 30 μm^2) prevents the organization of the lamellar features into a single-grain configuration.

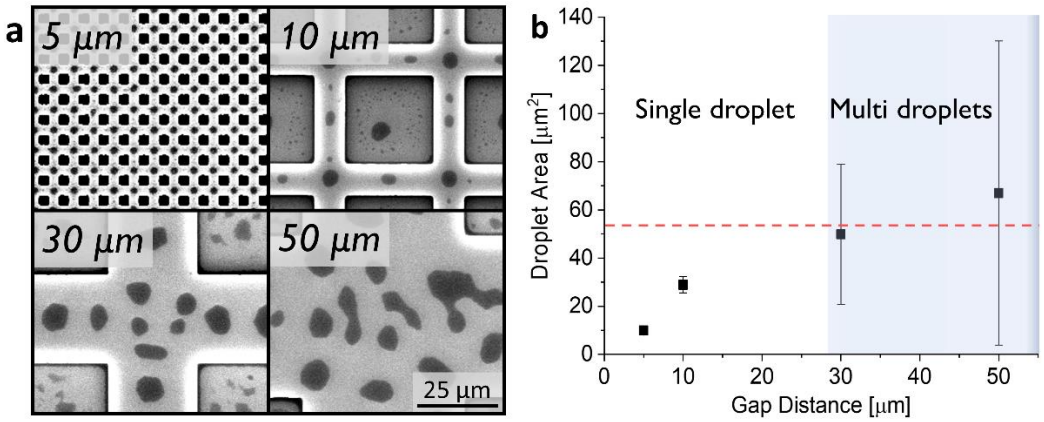

Figure 35: (a) SEM images of dewetting process over guiding patterns with mesh widths of 5, 10, 30 and 50 µm. (b) Relative droplet area distributions. Red dotted line indicates the average droplet area of dewetted BCP over a flat surface. Adapted from [2].

The best geometrical conditions of the micrometric patterns are achieved for guiding meshes with 5 µm widths. Under these constrictions, the dewetting process generates droplets in two sets of size distributions peaked at 0.5 and 10 μm^2 respectively (Figure 36a,d) with defectless lamellar ordering in a single-grains configuration (Figure 36b,c). The so achieved high level of ordering is to be attributed to the guiding mesh geometrical dimensions that enables for a filtering of the dewetted droplets in terms of dimensions and circularities (> 0.8) (Figure 36e) with consequent impact on the resulting nanoscale ordering in specific spatial locations, dictated by the topographic layout.

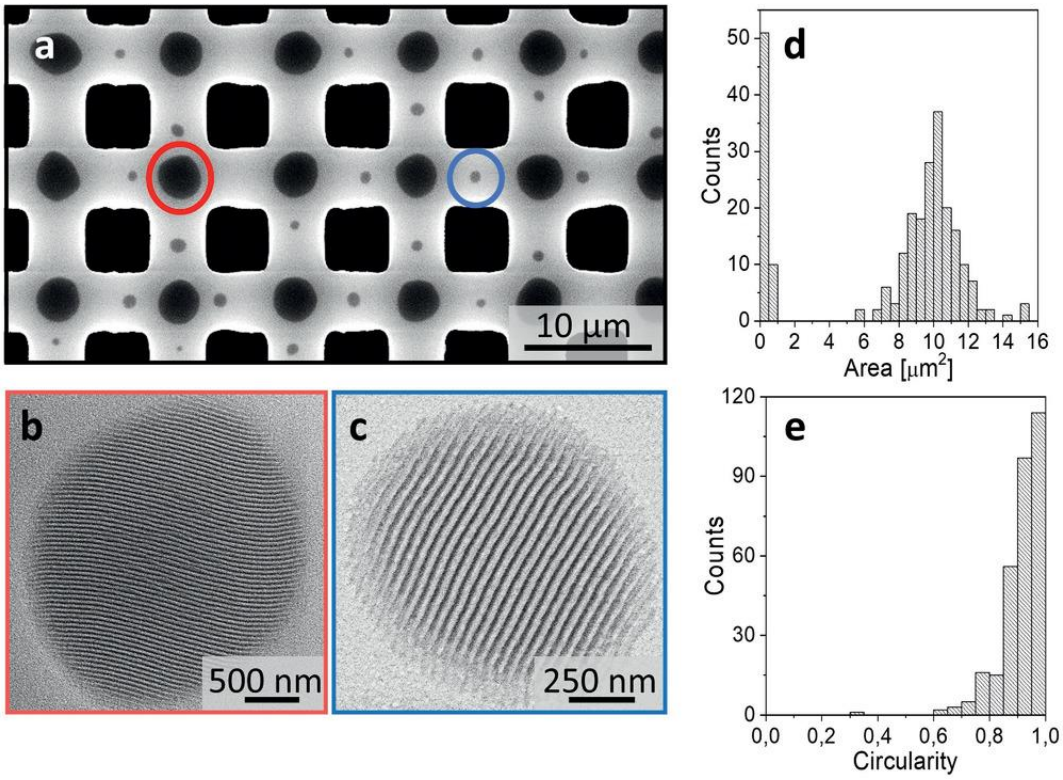

Figure 36: (a) SEM image of the hierarchical organization of blend BCPs dewetted over a large-area topographic guiding pattern with mesh width of 5 µm. SEM images of lamellar nanostructures in a single-grain configuration inside (b) 10 μm^2 and (c) 5 μm^2 average droplet areas. (d) Area distribution and (e) circularities of the dewetted droplets over the guiding template. Adapted from [2].

1.5.3 Hyperbolic metamaterial fabrication

The so-obtained hierarchical organization of the dewetted droplets was then employed as an effective template for the subsequent conversion into an HMM. Figure 37a describes the entire fabrication strategy involved into the realization of the HMM. After the guiding pattern definition and dewetting process, the PMMA domain was selectively removed by UV exposure and acetic acid bath (see methods section), resulting in PS lamellar structures interspaced with gaps of the same width of the PMMA nanodomains. Afterwards, a continuous Au film with a thickness of 70 nm, was sputtered on top of the entire hierarchical pattern. The subsequent pattern transfer process was then achieved by peeling off the Au layer with a transparent flexible UV cured resin. The UV cured resin was chosen in order to guarantee a good adhesion to the metallic film to withstand the mechanical stripping of the film from the BCP template. The pattern transfer process revealed a continuous Au layer which perfectly replicates the hierarchical

template (Figure 37b). The Au layer is constituted by 5 µm x 5 µm domes, interspaced by micrometric Au lamellae in a single-grain configuration that maintain the same geometrical parameters of BCP pattern (lamella width d = 18 nm ad pitch L_0 = 37 nm) (Figure 37c an 37d).

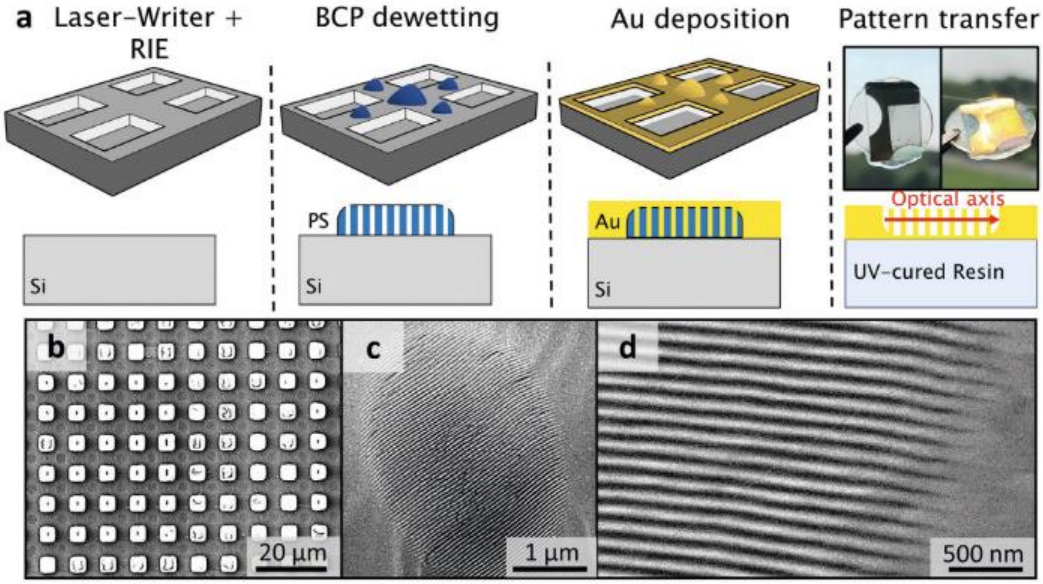

Figure 37: (a) Schematics of the fabrication strategy applied for the attainment of Au/air HMM based on hierarchical BCP blend film dewetting. (b-d) Different magnifications SEM micrographs of the continuous nanostructured Au layer after the pattern transfer process. Adapted from [2].

1.5.4 Effective medium approximation

The optical performances of so-obtained HMM were then assessed by experimental measurements supported by numerical modeling. For the numerical analyses, a model was constructed based on the geometrical parameters extracted from the SEM micrographs. The model consists of a periodic array of Au lamellae with width d = 18 nm, height h = 70 nm and pitch L_0 = 39 nm. A sketch of the resulting model is illustrated in Figure 38.

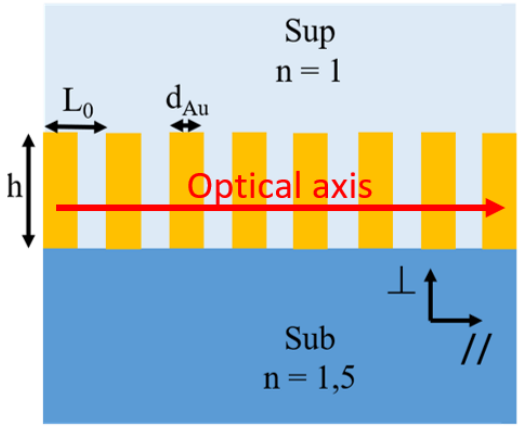

Figure 38: Cross-sectional view of the Au/air HMM model. Au lamellae geometric dimension: height h = 70 nm, width d = 18 nm and pitch L_0 = 39 nm. In-plane orientation of the optical axis is indicated by the red arrow. The refractive indexes are n = 1.5 and n = 1 for the substrate and superstrate, respectively. Adapted from [2].

Since the geometrical dimensions of the lamellar nanostructures are much smaller than the optical frequencies wavelengths (d << λ), the model can be homogenized by an effective medium approximation approach. For deeper insights into the modeling see Methods section. The following relations:

$$\varepsilon_{\perp} = \frac{\varepsilon_m \, d + \varepsilon_d \, (L_0 - d)}{L_0} \tag{1.11}$$

$$\frac{1}{\varepsilon_{\parallel}} = \frac{\frac{d}{\varepsilon_m} + \frac{(L_0 - d)}{\varepsilon_d}}{L_0} \tag{1.12}$$

describe the effective components of the permittivity tensor parallel ($\varepsilon_{\parallel}$) and perpendicular ($\varepsilon_{\perp}$) to the optical axis, while ε_m is the Au permittivity measured by ellipsometry (Figure 39), and ε_d is set to 1.

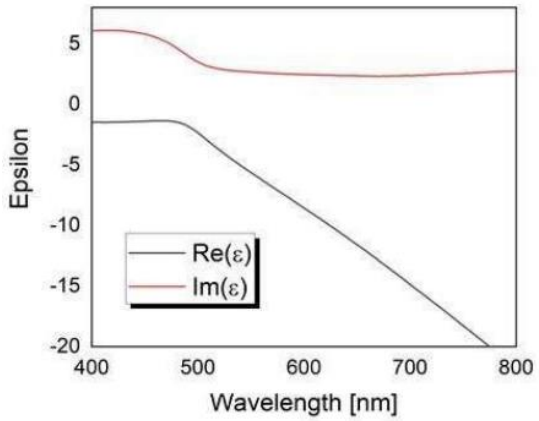

Figure 39: Dielectric permittivity's real and imaginary components of a 70 nm Au layer over a glass substrate extracted by J.A. Wollam Co. alpha-SE ellipsometer. Adapted from [2].

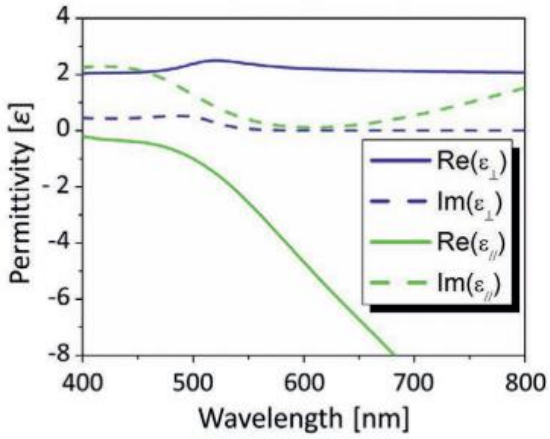

Figure 40: Real and imaginary permittivity components, perpendicular ($\varepsilon_{\parallel}$) and parallel ($\varepsilon_{\perp}$) to the optical axis in the visible spectrum of the HMM model by EMA. Adapted from [2].

Figure 40 reports the real and imaginary components of the permittivity tensor parallel ($\varepsilon_{//}$) and perpendicular ($\varepsilon_{\perp}$) to the optical axis of the effective material over the visible spectrum (400 – 800 nm). At low wavelengths ($\lambda < 500$ nm) the imaginary component increases, thus indicating the presence of absorption losses. However, the real components hold opposite signs over the considered wavelength range, suggesting a hyperbolic behavior of the HMM over the entire visible spectrum. Specifically, the parallel component is positive ($\varepsilon_{//} > 0$), while the perpendicular component in negative ($\varepsilon_{\perp} < 0$), therefore indicating that the HMM in the present configuration can be referred to as a type II HMM. To

support the hyperbolic behavior of the HMM, in Figure 41a is reported the reflectance map as a function of λ and the effective index calculated as $n_{eff} = k_x/k_0$ computed by a rigorous coupled wave analysis (RCWA) code (see Method section) that clearly shows two propagative modes at high-magnitude wavevectors. Moreover, the reflectance map, when in the (ω,k) space, reveals two negative slopes (Figure 41b) that better illustrate the dispersion relation of the modes.

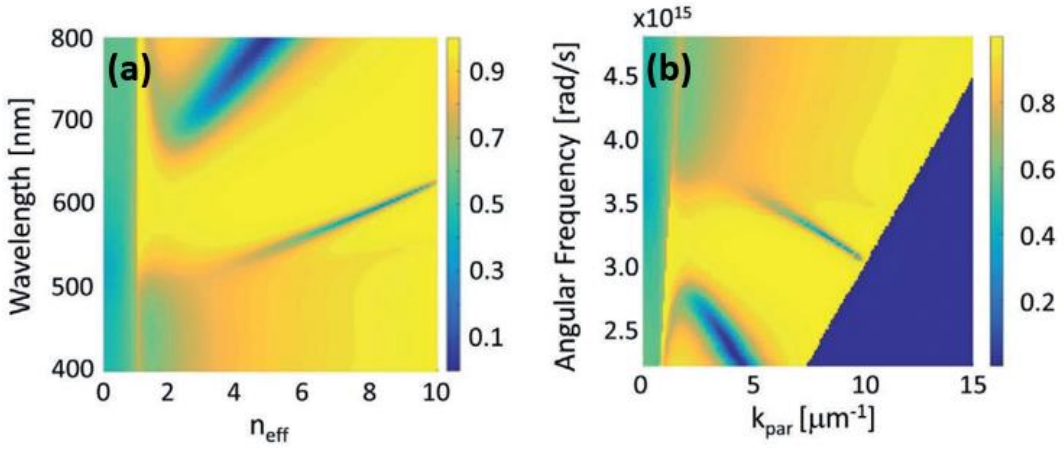

Figure 41: Reflectance maps computed (a) as a function of wavelength against effective index with EMA approximation and (b) as a function of angular frequency ω against the parallel wave-vector to the optical axis k_{par}. Adapted from [2].

To verify the optical properties of the proposed model, we computed the optical response of a photon emitting source (dipole), coupled with the HMM. The computed far-field distribution at a wavelength of λ = 594 nm, reveals to be bounded to the surface and propagated by near-field coupling among consecutive lamellae (Figure 42a). In addition, the Purcell factor, computed both by assuming the EMA approximation and the real structure, peaks at 590 nm with a broadband enhancement for larger wavelengths (Figure 42b). The spectral profiles match for both models, however as reported in literature [23], the EMA approximation overestimates the Purcell factor by a factor of 2 when compared to the real model. Under these considerations, however, a Purcell factor of 15 at 590 nm is expected for the proposed HMM.

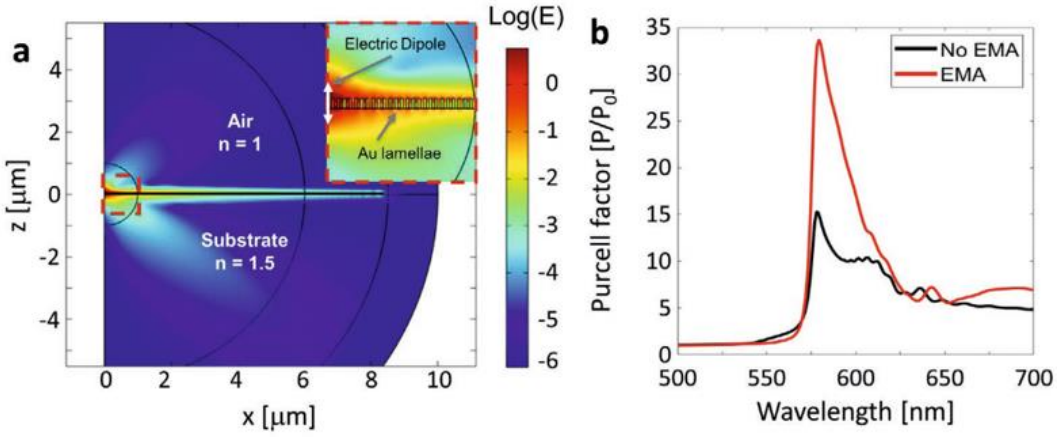

Figure 42: (a) Electric field distribution radiated by a dipole at 594 nm in which the colorbar is represented in log scale. The inset is reported for a better view of the zone marked by the red dotted line and the dipole orientation is illustrated by the white arrow. (b) Computed Purcell factor for EMA assumption and real structure. Adapted from [2].

1.5.5 Luminescence lifetime dynamics measurements

The experimental assessment of the hyperbolic properties of the HMM was conducted by luminescence lifetime dynamics measurements of nitrogen-vacancy (NV) centers [99] inside a nanodiamond positioned on top of a single lamellar droplet as shown in Figure 43a. The measurement setup employed on these measurements was previously described in the Method section and illustrated in Figure 16. The use a laser beam with 10 ps pulses centered at 490 nm and a spot size of 1 μm, allowed to perform the local excitation of a single nanodiamond placed over an isolated lamellar droplet, avoiding any contribution from the nearby nanostructures. The NV centers in nanodiamonds were selected as single photon sources for the present study since their emission spectrum matches the Purcell factor spectral range at which the highest value was computed. The relative time-resolved decay curves in Figure 43b show a clear reduction in the fluorescence lifetime of the NV center when placed on top of the Au lamellar droplets, up to one order of magnitude higher than when placed over a flat Au layer or a bare glass substrate. This strong lifetime reduction is clear evidence of a larger density of radiative decay channels associated with the hyperbolic behavior of the fabricated material. We can conclude that the experimental assessment of the optical properties resulted in a reduction of the fluorescence lifetime decay of single photon sources when placed in proximity to the HMM. The hyperbolic behavior of the proposed material is supported by numerical modeling that

indicates a strong Purcell factor in the same spectral range of the NV centers (Figure 42b).

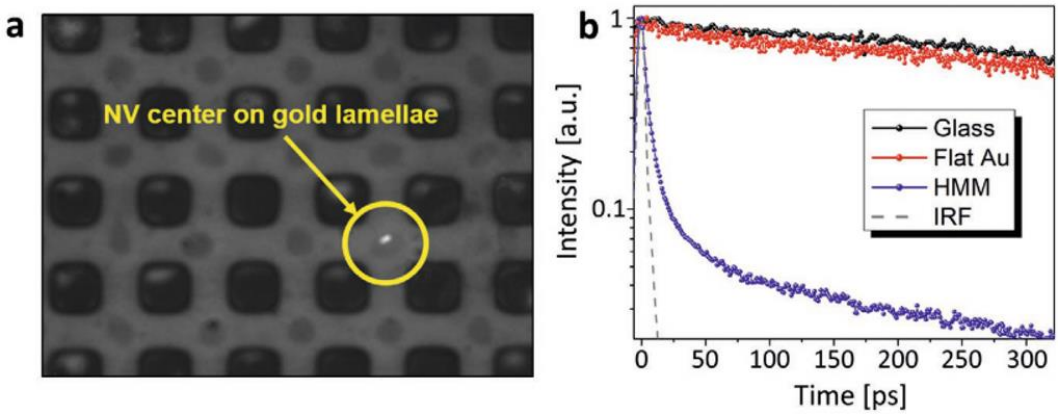

Figure 43: (a) Optical image of the hierarchical Au layer after pattern transfer process superimposed to the fluorescence image of an excited nanodiamond with NV centres over a single Au lamellar droplet. (b) Lifetime fluorescence decay measurements of the same nanodiamond on top of the HMM (violet dots), glass surface (black dots) and flat Au film (red dots) respectively. Adapted from [2].

1.5.6 Towards the optimization of HMMs

The proposed strategy based on BCP film dewetting, although representing a first attempt on the realization of simple systems that consist of Au lamellae interspaced with air, clearly suggests that BCPs can be used as effective templates for the fabrication of metamaterials with hyperbolic behavior. The BCP dewetting, as a general nanopatterning tool, however, suffers from some limitations imposed by the intrinsic constraints determined by the dewetting process itself. These constraints are related to the limited patterned area, and consequently to a limited number of lamellar features, as well as to an inhomogeneous distribution of the lamellar heights along the dewetted droplet. This strongly reduces the control over geometrical parameters of the fabricated material. Moreover, the metallic pattern transfer process, based on metal deposition and film stripping, imposes limits on metallic film thickness and on the choice of the metal/dielectric composition. The poor control over the geometry and composition results in a lower degree of freedom on the selection of the different dimensional and analytical parameters for the design of HHMs with optimized performances. As shown by the Finite Element Method (FEM) calculations of real structures in Figure 44a, the spontaneous emission enhancement is strongly affected by even slight changes on the Au lamellar

features height. The progressive increase of the lamellar height from 50 to 100 nm induces a Purcell factor shift towards higher wavelengths in the Vis spectrum, along with modulations of the peak intensities.

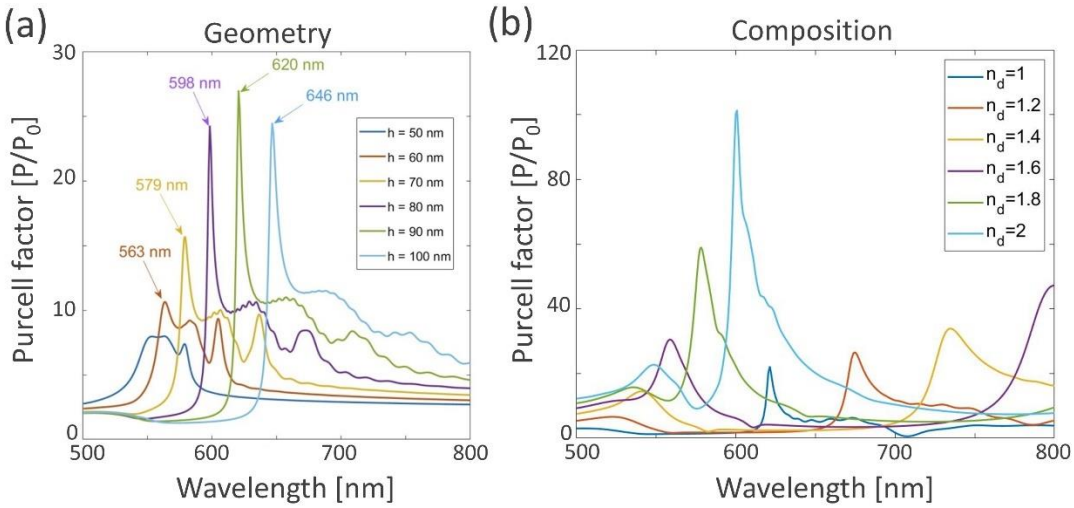

Figure 44: (a) Computed Purcell factor evolution of Au/air HMM as a function of different Au lamellae heights. (b) Computed Purcell factor evolution of HMM constituted by Au/dielectric material as a function of different refractive indexes of the dielectric. The heights of Au and dielectrics lamellae features were set to 90 nm.

An even stronger influence on the Purcell factor peak intensity is determined by the proper choice of the dielectric material. Figure 44b illustrates that the employment of high refractive index materials such as metal oxides (Table 1), can sensibly enhance the Purcell factor, reaching extraordinary values higher than 100.

Table 1: Refractive indices of dielectric materials at 550 nm.

PDMS	**PMMA**	**PS**	**Al_2O_3**	**ZnO**	**TiO_2**
1.42	1.49	1.59	1.77	2.02	2.65

The Purcell factor profile is characterized by a very narrow peak with a high intensity ratio with respect to the background. The control over the Purcell factor's position and peak intensity, can be exploited to match the emission spectral profile of a single-photon emitter determining its amplification on a

specific frequency, representing therefore one of the key advantages towards the optimization of HMMs' optical performances.

The optical properties of HMMs, as shown by the numerical modeling reported in Figure 44a,b, exhibit a strong dependency on the geometry and composition of the constituent materials, demonstrating that even slight variations in terms of nanofeature's height or refractive index significantly influence the optical properties by a strong enhancement of the computed Purcell factor. The great sensibility of the optical properties of HMMs to the dimensions and compositions of the constituent metal and dielectric, requires therefore the development of novel fabrication processes that provide precise control on the metal/dielectric constituent materials, that go beyond the current nanopatterning and material deposition/growth technologies. The proposed fabrication scheme, that relies on the dewetting phenomenon of BCP blend films, poses some limitations in terms of nanostructures' achievable configurations due to their geometrical inhomogeneities and their local alignment that also prevent a facile positioning of the SPS, hindering therefore their on-chip integration. Long-range nanostructures' ordering induced by global alignment methods of BCPs, such as soft-shear laser zone annealing (SS-LZA) [100,101], would guarantee wide-area nanopatterning with low defectivity. Novel alignment strategies along with the great flexibility offered by BCP self-assembly and in combination with new synthetic processes can be further exploited for the development of more complex photonic devices, paving the way for an easy fabrication of photonic hypercrystals, hyperbolic waveguides and providing an additional degree of freedom for the fabrication of graded index elements. In this perspective, during the PhD project different fabrication avenues were explored with the aim to develop the most suitable methodology that provides the degree of control needed to meet the best conditions for enhanced optical performances.

Chapter 2

Hybrid Metrology for HMMs

Related publications:

[102] *Malafronte, A., Emendato, A., Auriemma, F., Sasso, C., Laus, M., Murataj, I., Ferrarese Lupi, F. & De Rosa, C. (2020). Tailored inclusion of semiconductor nanoparticles in nanoporous polystyrene-block-polymethyl methacrylate thin films. Polymer, 210, 122983.*

[103] *Murataj, I., Cara, E., Baglieri, N., Pirri, C. F., De Leo, N., & Ferrarese Lupi, F. (2022). Liquid Phase Infiltration of Block Copolymers. Polymers, 14(20), 4317.*

[104] *Cara, E., Murataj, I., Milano, G., De Leo, N., Boarino, L., & Ferrarese Lupi, F. (2021). Recent Advances in Sequential Infiltration Synthesis (SIS) of Block Copolymers (BCPs). Nanomaterials, 11(4), 994.*

The work reported in this chapter finds its motivation in the development of novel fabrication and characterization methodologies aimed at the improvement of HMMs' performances (Figure 44a and 44b). As discussed in the previous chapter, the optimization of such photonic structures could be achieved through a great control over the morphology and composition of the constituent materials, as well as a reliable measurement strategy to fully characterize complex nanostructures. The development of novel fabrication avenues could provide additional control over the geometrical and compositional parameters that go beyond the intrinsic limitations of conventional lithographic and material deposition/growth

technologies. On the other hand, the strong dependency of the material's functionality over its chemical and physical properties requires the implementation, in a hybrid approach, of different characterization techniques applied to the same area, in order to gain information on the whole set of compositional and dimensional parameters of such complex nanostructures. This requires therefore the fabrication of materials that could be employed as model systems for a reliable interpretation and correlation of materials' functionality to their underpinning physical and chemical properties. The following section will illustrate novel fabrication routes based on the selective infiltration of inorganic materials into self-assembled BCPs. Then, an analytical strategy based on a hybrid metrology approach is applied to reveal dimensional and analytical information on such nanomaterials. This strategy relies on the implementation and correlation of different analytical techniques such as scanning probe and electron microscopy, combined with synchrotron-based X-ray spectroscopy.

2.1 Fabrication of model systems for hybrid metrology

2.1.1 Nanoparticle inclusion

In a first attempt to fabricate high-refractive index materials, ZnO and CdSe pre-synthesized nanoparticles were incorporated into self-assembled nanostructures in a joint collaboration with Università degli Studi di Napoli Federico II and Università del Piemonte Orientale [102]. The ZnO nanoparticles incorporation inside the BCP template was achieved by their selective localization into the PS domain after dispersion into a BCP solution. The subsequent UV irradiation selectively removed the PMMA domain leading to nanostructured PS lamellae filled with ZnO nanoparticles without any alteration on the PS nanodomains morphology (Figure 45a). A different approach was employed for the incorporation of CdSe nanoparticles. Here, the BCP template was dipped into an ethanol dispersion of CdSe nanoparticles after the PMMA removal, leading to a selective deposition of the nanoparticles inside the resulting nanochannels (Figure 45b). The typical dimensions of ZnO (d = 5.3 nm) and CdSe (d = 3.2 nm) nanoparticles were sufficiently small to allow their selective inclusion in the PS domain or their localization into the BCP nanochannels. However, due to the intrinsic nanoparticle nature of employed ZnO and CdSe materials, this incorporation route leads to a simple organization of individual nanoparticles, posing severe limitations on the optical properties determined by related possible scattering issues and optical losses.

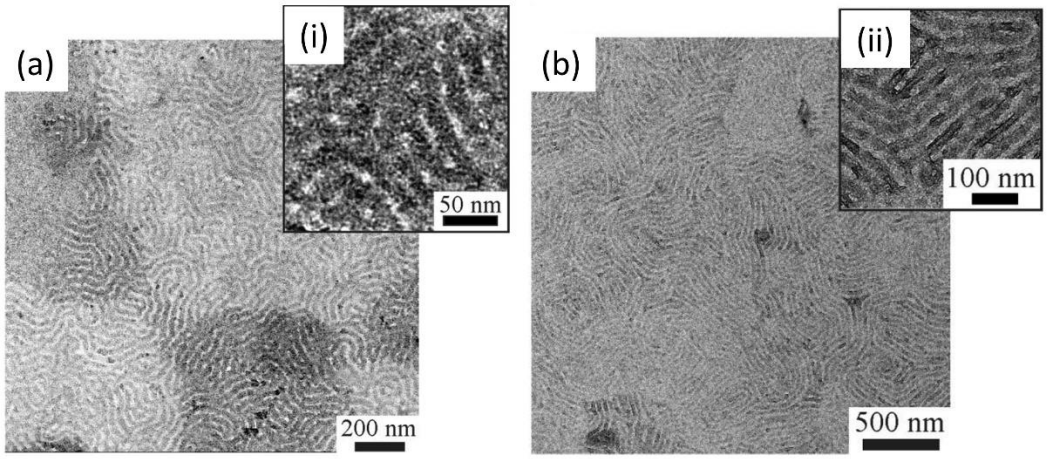

Figure 45: (a) TEM micrographs of BCP filled with ZnO nanoparticles before UV irradiation and (i) relative higher magnification image. (b) TEM micrographs of BCP dipped into CdSe solution and (ii) relative higher magnification image. Adapted from [102].

2.1.2 Electrodeposition

In the pursuit of a fabrication methodology that provides the desired control over dimensional and compositional material characteristics, a joint activity on the electrodeposition of Au inside BCP templates was carried out in the framework of a NFFA-EU project in collaboration with the Institute of Microelectronics of Barcelona (IMB-CSIC). Based on the FEM simulations reported in Figure 44a,b that showed the highest enhancement of the Purcell factor for nanostructures' typical heights above 90 nm, the aim of this project regarded the growth of high aspect-ratio Au nanofeatures using BCP thick films (h > 100 nm) as templates. To this purpose, lamellar and cylindrical BCP templates were fabricated on top of a Ni-Ti-Al conductive substrate with different film thicknesses in the range from 70 to 150 nm. Electrodeposition is a well-exploited method for the growth of nanometric metallic features when applied to solid templates. Figure 46a shows examples of Au electrodeposition into lamellar BCP templates with film thicknesses of 100 nm. For short electrodeposition times (300 s), there is no evidence of electrodeposited Au. For longer times (60 and 1200 s) however, sporadic growth of nucleated Au nanoparticles appears on the substrate surface along with a BCP film disruption. This behavior could be associated with an incomplete PMMA phase removal. In thick lamellar BCP films, the total removal of the PMMA phase might be prevented by a collapse of the PS lamellar domains during the progressive degradation of PMMA. This hinders therefore a direct contact of the electrolytic solution with the conductive substrate through the

polymeric template, leading as a consequence to the constriction for Au to grow underneath the polymer film. Cylindrical BCP templates are revealed to be better candidates for the electrodeposition of high aspect-ratio nanofeatures. Compared to the lamellar ones, cylindrical templates have a higher robustness to withstand the PMMA removal without sensible collapse of the PS sidewalls. The successful electrodeposition process, however, was prevented by an inhomogeneous and incomplete deposition of Au inside the cylindrical voids (Figure 46b,c).

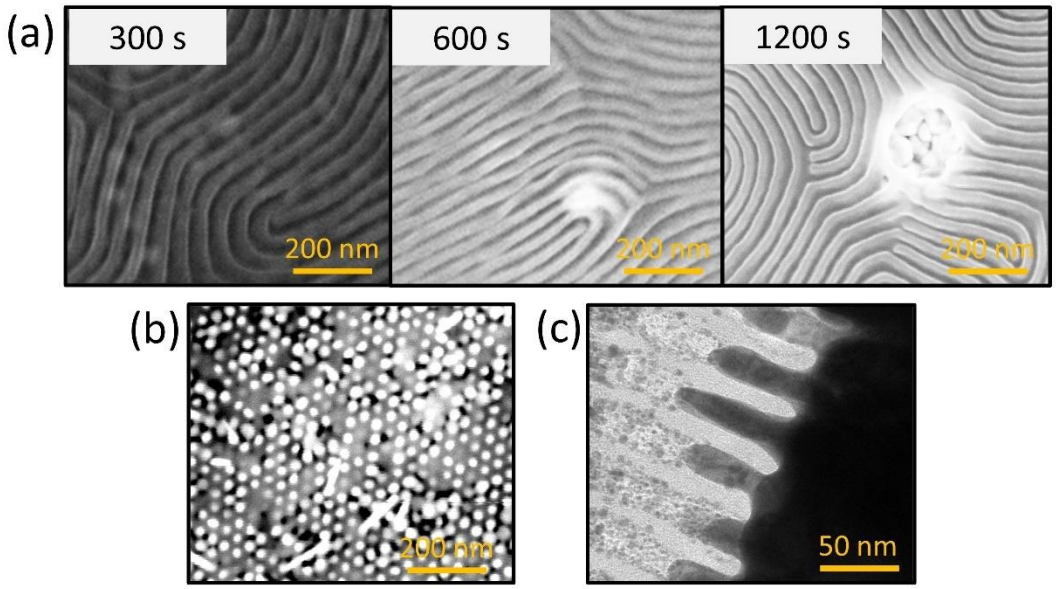

Figure 46: (a) SEM micrographs of thick (100 nm) lamellar BCP templates after Au electrodeposition at 2.5 mA for different deposition times. (b) Top-view SEM image of cylindrical BCP template after Au electrodeposition at 2.5 mA for 600 s and (c) relative cross-section TEM view.

2.1.3 Selective infiltration processes

Among the various strategies that could be employed for the incorporation of inorganic materials into BCPs, in the last years, infiltration processes as liquid phase infiltration (LPI) [103] and sequential infiltration synthesis (SIS) [104] demonstrated to be the most suitable synthetic approaches for the fabrication of advanced materials with tailored properties. Both infiltration processes take advantage of the chemical differences of the constituent blocks of self-assembled BCPs. The different functional groups carried by each polymeric domain are responsible for the selective interaction of specific metal salt or metalorganic precursors with one of the two components of the BCP. Subsequent precursor reduction/oxidation and polymer removal reveal a nanostructured metal or metal

oxide that perfectly replicate the polymeric template morphology. The major differences between the two infiltration processes rely on the different experimental conditions, equipment and on the different inorganic materials that can be synthesized.

Specifically, LPI is a wet chemical process in which the selective binding of a metal salt precursor is driven by a complexation or electrostatic interaction with the functional groups of the polar domain on the self-assembled BCP (Figure 47).

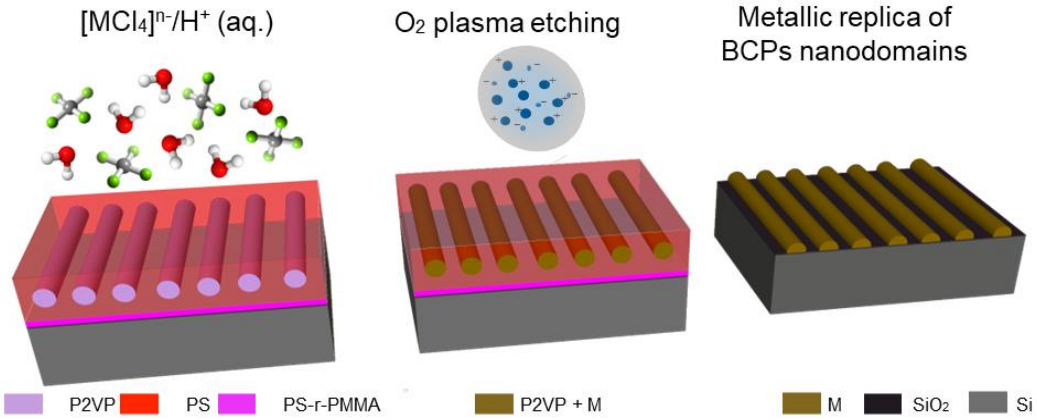

Figure 47: Schematics of the LPI of cylindrical PS-*b*-P2VP horizontally aligned to the substrate. Adapted from [103].

LPI, when applied to BCPs, provides a great control over the nucleation and growth of different inorganic materials in which the structural/compositional distribution is controlled by the infiltration conditions of different metal salt precursors. The range of different inorganic materials that can be synthesized spans from metals (Pt. Pd, Au, Co, Fe, Ni, Cu) to alloys (FePt, AuAg), metal oxides (Fe_2O_3, Fe_3O_4, NiO, Cr_2O_3) and metal halide perovskites ($MAPbBr_3$). By taking advantage of the most recent BCP nanopatterning techniques such as directed self-assembly (DSA) [105], multi-mechanism directed self-assembly (MMDSA) [106] and soft-shear laser-zone annealing (SS-LZA) [100], in combination with a judicious choice of simultaneous or sequential precursors infiltration, this process allows for the fabrication of different multicomponent materials, arranged in complex nanoarchitectures that are exploited for different applications in photonics [107], plasmonics [108] and electronics [109]. Although the wide variety of infiltrated materials provided by LPI, the synthesis of high-refractive index metal oxides (*e.i.* Al_2O_3, ZnO and TiO_2) required for the

fabrication of HMMs, is prevented by the low availability of suitable precursors that can be used in wet conditions.

To this end, the different processing conditions at which the SIS operates, allow for the employment of metalorganic precursors (for the synthesis of Al_2O_3, ZnO, TiO_2), such as TMA, DEZ, $TiCl_4$ in vapor phase. SIS is an infiltration process that shares the same apparatus and metalorganic precursors of atomic layer deposition (ALD). In contrast to LPI, SIS is a vapor-phase process that consists in the cyclic exposure of self-assembled BCPs to metalorganic precursors and oxidizing agents such as water, ozone or hydrogen peroxide leading to the selective nucleation and growth of metal oxides inside the polar BCP domain. SIS follows a Lewis acid-base interaction mechanism between the metalorganic precursor and the functional moiety of the BCP polar domain (Figure 48a).

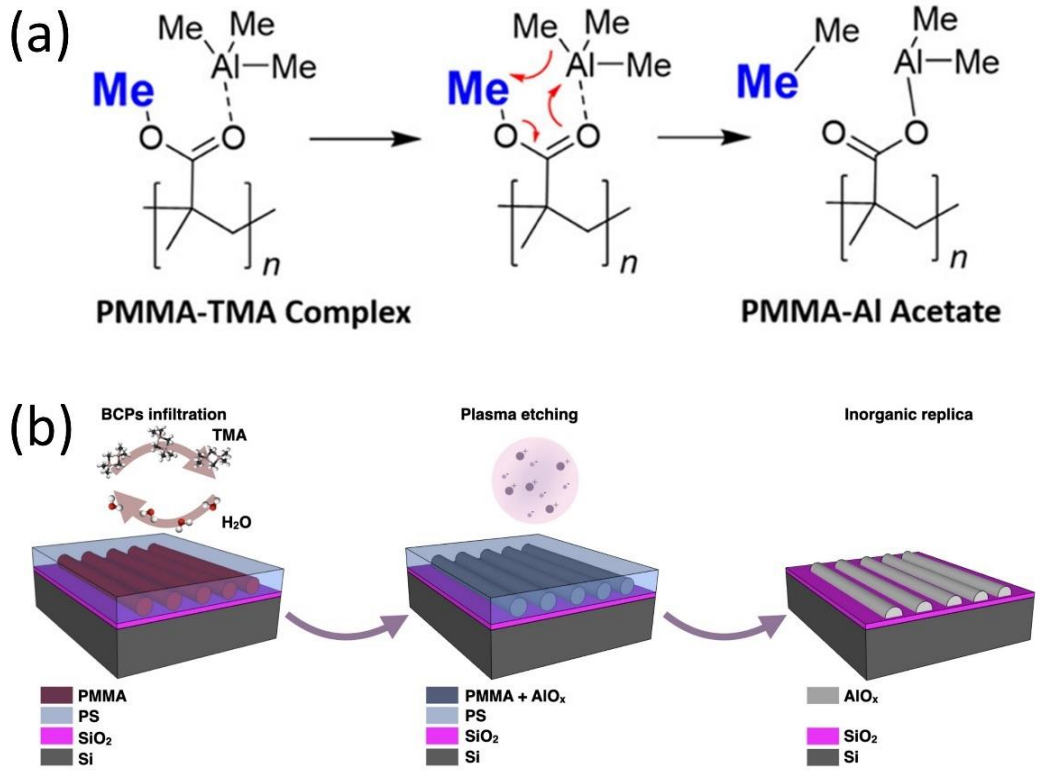

Figure 48: (a) LPI mechanism for trimethylaluminum (TMA) and PMMA. Adapted from [110]. (b) Schematics of the SIS of cylindrical PS-*b*-P2VP horizontally aligned to the substrate. Adapted from [104].

The subsequent exposure to the oxidizing agent determines the oxidation of the precursor located in the BCP. The following polymer removal by plasma etching or polymer ashing reveals a nanostructured oxide whose morphology is inherited by the BCP template (Figure 48b). Compared to ALD, used as a deposition tool of very thin conformal metal oxide coatings, SIS requires substantially different processing parameters in order to penetrate, diffuse and selectively entrap the metalorganic precursors inside the polymeric template (Figure 49a) [111]. This reflects therefore into a higher complexity on the choice of the experimental conditions due to the increased number of involved parameters that extend those of the conventional ALD (*e.i.* polymer-precursor interaction and precursor diffusion) with direct consequences on material mass incorporation and pattern quality. Among the different SIS protocols, micro-dose infiltration synthesis (MDIS) [112] guarantees a superior amount of infiltrated material thanks to the multiple repetition of precursor dosing while still maintaining static vacuum. This modified protocol translates into an increased fidelity and more uniform conversion of the BCP template into metal oxide (Figure 49b,c).

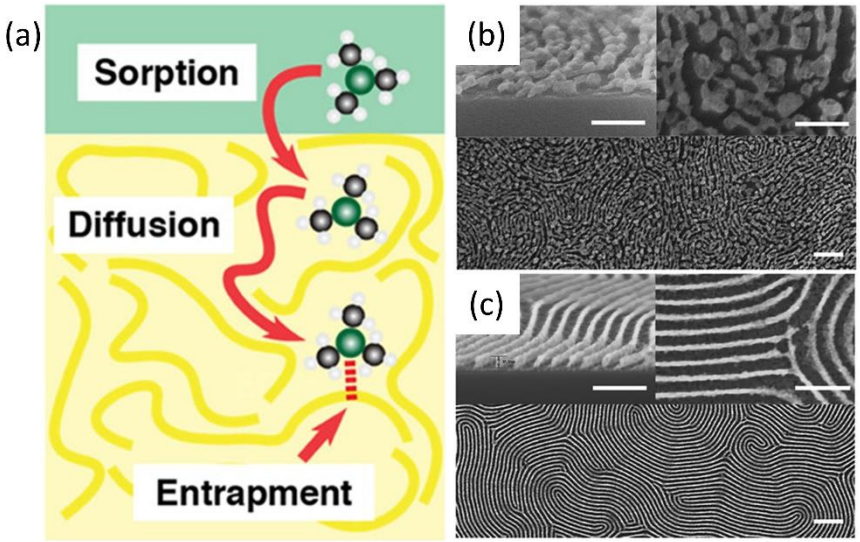

Figure 49: (a) Schematic representation of the different processes involved in the SIS. Adapted from [113]. SEM images of a comparison between (b) PS-*b*-P2VP infiltrated with ZnO with conventional SIS protocol and (c) PS-*b*-P2VP infiltrated with ZnO with MDIS protocol. Scale bars are set to 100 nm. Adapted from [114].

The increasing expansion of the SIS in the recent years, opened new opportunities to define novel nanomaterials with tailored properties for their direct application into different research fields. The seek for a comprehensive

understanding of SIS-based materials, pushed the researchers towards the characterization of chemical and structural properties by complementary *in situ* and *ex situ* vibrational [115], optical [116] and X-ray spectroscopic methods [117] combined with electron [118] and scanning probe microscopies [119]. To further assess the control and optimization of the material properties, basic metrology requirements must be met in terms of traceability and absolute quantitative methods that provide valid interlaboratory comparison and a more reliable data interpretation. To this end, the development of hybrid metrology protocols would guarantee a reliable correlation of the material dimensional and compositional properties to their functionality through the implementation of complementary analytical tools.

2.2 Hybrid metrology at the nanoscale

The increasing demand for advanced materials with boosted performances, has pushed the research to the development of ever so smaller and complex materials. At the nanoscale dimensions, even slight deviations from a certain dimensional or compositional nominal value sensibly affects the material properties. One of the key metrology challenges is currently represented by the ability to measure all the dimensional and analytical parameters on such advanced nanomaterials for an accurate correlation to their functionality. At the moment, the complete description of a nanomaterial on its geometry and composition, cannot be provided by a single analytical method due to limitations on resolution, low value of uncertainty, measurement speed and physical inaccessibility of the measurand to a specific characterization tool. The implementation of complementary analytical techniques, with a wide range of underlying physics and in the same region of interest, is therefore required to ensure a more reliable characterization by using the best attributes of each single technique. In this context, hybrid metrology has emerged in the last years, as a measurement strategy that takes advantage of the correlation of the data obtained by several analytical tools, for a more reliable and valid comparison of the results to better illustrate the relationship between material properties and functionalities. One of the main issues when comparing various measurement techniques with substantially different underlying physics, is represented by divergences on the results for the same nominal measurand. As an example, AFM and SEM make possible the geometrical characterization of nano-objects. However, the observation of the measurand on both techniques is different due to their distinct measurement principles, *e.i.* the detection of interaction of the tip with the substrate and electron

beam-sample interaction, respectively [120]. The implementation of synchrotron-based traceable X-ray spectrometry techniques [121] along with a good knowledge of the relationship of each targeted measurand to the specific physical or chemical quantities of interest, allows for mutual validation and more complete, coherent description of complex samples.

2.3 Materials and Methods

This section provides the details of all the materials, methods and technologies exploited during the fabrication of model systems based on BCPs and the analytical techniques employed for their full characterization by a hybrid metrology approach.

2.3.1 TiO_2 nanostructures synthesis protocol

TiO_2 nanostructures were fabricated by selective infiltration of self-assembled BCP films by SIS and used as a model system for the development of a hybrid metrology characterization strategy. To this purpose, two sets of samples consisting of lamellar and cylindrical forming PS-*b*-PMMA were fabricated. Two lamellar samples were fabricated by self-assembly process of two lamellar forming PS-*b*-PMMA BCPs with M_w = 146 kg mol^{-1}, PDI = 1.20, f_{PS} = 50.0% (wt/wt) and M_w = 160 kg mol^{-1}, PDI = 1.09, f_{PS} = 50.0% (wt/wt), respectively. Two cylindrical samples were fabricated by self-assembly process of two cylindrical forming PS-*b*-PMMA BCPs with M_w = 82 kg mol^{-1}, PDI = 1.06, f_{PS} = 69.5% (wt/wt) and M_w = 101.5 kg mol^{-1}, PDI = 1.09, f_{PS} = 67.0% (wt/wt), respectively. The PS-*b*-PMMA, both lamellar and cylindrical forming, were purchased from Polymer Source Inc. and used without further purification. Random copolymer grafting process was used for the substrate neutralization and promotion to perpendicular orientation of BCP nanostructures. PS-*r*-PMMA labelled FSM7 with M_n = 14.60 kg mol^{-1}, f_{PS} = 58.7% (wt/wt) and PDI = 1.30 was grafted to 100 nm SiO_2 substrate for the perpendicular promotion of lamellar nanostructures. PS-*r*-PMMA labelled FSM4R1 with M_n = 19.93 kg/mol, f_{PS} = 59.0% (wt/wt) and PDI = 1.13 was grafted to 100 nm SiO_2 substrate for the perpendicular promotion of cylindrical nanostructures. Lamellar BCP were annealed by RTP at 230 °C for 600 s, in N_2 environment whereas the cylindrical samples were thermally treated in RTP at 190 °C for 450 s in N_2 environment. The SIS was carried out inside a commercial ALD system (BENEQTFS 200) at 150 °C using $TiCl_4$ as metal organic precursor and water as oxidant. All the four samples were processed simultaneously, undergoing the same infiltration

conditions for a total number of 80 ALD cycles with a MDIS protocol [109]. The timing sequence of each single cycle consists of exposure of $TiCl_4$ and water by dosing the precursors for 100 ms every 100 ms for 100 times followed by chamber purging with N_2 (250 sccm) for 30 s. Polymer matrix removal was subsequently performed by Ar plasma (100 W for 600 s). In this paper the infiltrated samples obtained by SIS of BCP with M_w = 146 kg mol^{-1}, M_w = 160 kg mol^{-1}, M_w = 82 kg mol^{-1} and M_w = 101.5 kg mol^{-1} will be referred to as LAM146, LAM160, CYL82 and CYL102 respectively (Figure 50).

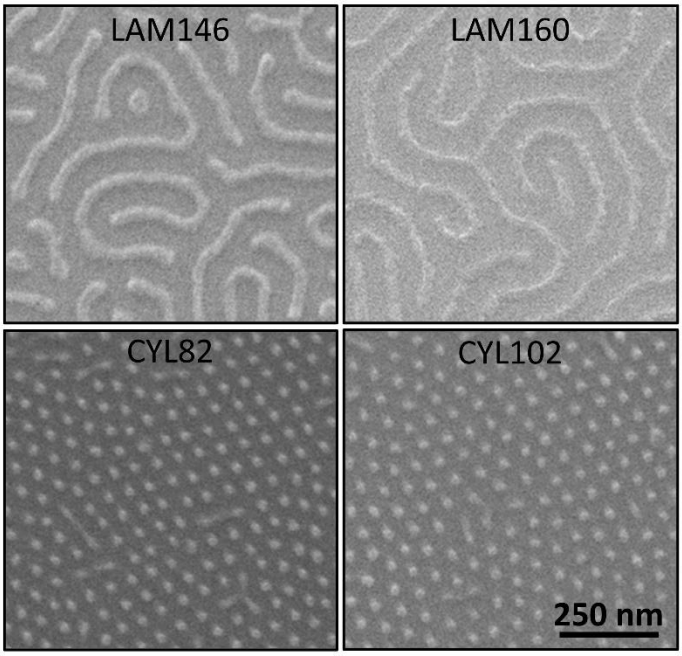

Figure 50: Top-view SEM images of TiO_2 nanostructures obtained by SIS of lamellar (LAM146 and LAM160) and cylindrical (CYL82 and CYL102) BCP templates with different M_w.

2.3.2 Grazing-incidence small-angle X-ray scattering

The grazing-incidence small-angle X-ray scattering (GISAXS) experiments on the BCP-based samples were conducted at the Four Crystal Monochromator (FCM) beamline of Physikalisch-Technische Bundesanstalt (PTB) X-ray radiometry group at synchrotron BESSY II in Berlin, Germany. The beamline operates in the tender X-ray regime, offering a photon energy E_{ph} from 1.75 keV to 10 keV. In GISAXS measurements performed on the infiltrated samples, the incident focused beam (E_{ph} = 6 keV) with a spot size of 0.5 mm x 0.5 mm impinged on the samples at grazing angle θ = 0.70° with an acquisition time of 30 s at which we observed

the highest intensity of the diffraction pattern. The GISAXS scheme is illustrated in Figure 51. The elastically scattered waves were detected by an in-vacuum calibrated PILATUS 1M hybrid pixel detector with 172 µm x 172 µm pixel size [122], installed on a movable sledge at 5063 mm of distance from the samples. The detector is constituted by 10 separate modules with 20-bit counters for every pixel The GISAXS patterns were recorded on 10 different positions of each sample integrating 20 measurements on each position.

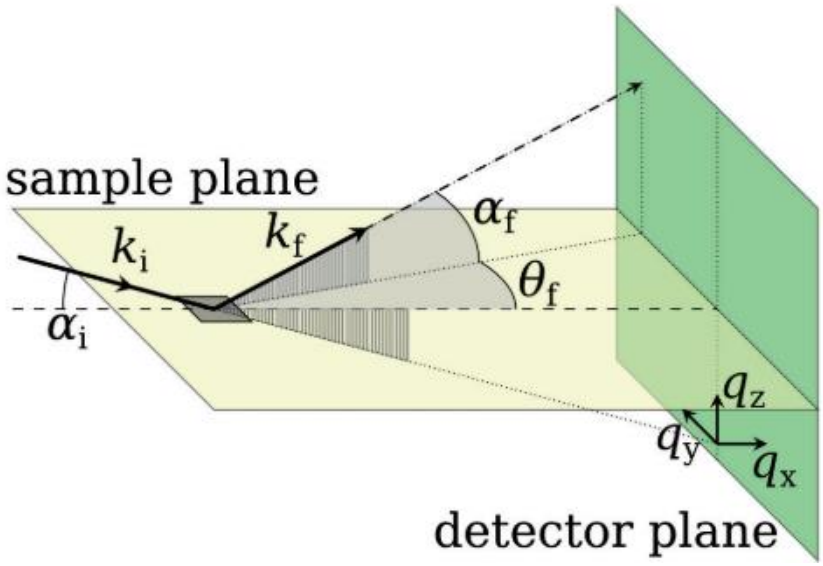

Figure 51**:** Schematic illustration of a GISAXS setup. The monochromatic radiation impinges on the sample surface at grazing angles and the elastically scattered radiation is collected by an area detector placed in a vertical position to the sample surface. Adapted from [123].

2.3.3 Grazing-incidence X-ray Fluorescence

The reference-free grazing-incidence X-ray fluorescence (GIXRF) measurements were performed at the FCM beamline of PTB X-ray spectrometry group at synchrotron BESSY II in Berlin, Germany. The samples were placed on a 9-axis sample manipulator inside an ultra-high vacuum (UHV) chamber which allows very precise sample alignment and tuning of the synchrotron radiation at grazing incident angles (θ) to the sample surface. For the quantification of Ti on the TiO_2 nanostructures obtained by sequential infiltration synthesis, the incident monochromatic X-ray beam energy was set at E_{in} = 6 keV, exceeding the X-ray absorption Ti *K*-edge of 4.966 keV. The employment of a calibrated silicon drift detector (SDD) in terms of both response function and detection efficiency placed

in the perpendicular plane of the incident beam, allows for an energy-dispersive detection of the emitted fluorescence minimizing the scattered radiation. A representation of the measurement setup is visible in Figure 52. The incident photon flux is monitored by calibrated photodiodes. The reference-free material quantification can be obtained once all the relevant instrumental and fundamental parameters are known in terms of mass deposition m_i/F_1 of an element i in a unit area F_1 following the expression:

$$\frac{m_i}{F_1} = -\frac{1}{\mu_{\mathrm{tot},i}} \ln\left\{1 - \frac{P_{i,j}}{P_{\mathrm{in}} I_{\mathrm{XSW}}(E_{\mathrm{in}},\theta)\frac{\Omega_{\mathrm{det}}}{4\pi}\frac{1}{\sin\theta}\frac{Q_i(E_{\mathrm{in}})}{\mu_{\mathrm{tot},i}}}\right\}, \tag{2.1}$$

$$\mu_{\mathrm{tot},i} = \frac{\mu_i(E_{\mathrm{in}})}{\sin\theta} + \frac{\mu_i(E_{i,j})}{\sin(90^\circ - \theta)} \text{ and } Q_i(E_{\mathrm{in}}) = \tau_{Xi}(E_{\mathrm{in}})\omega_{Xi}g_{j,Xi} \tag{2.2}$$

where θ is the angle of incidence of the X-ray beam, E_{in} the incident photon energy, P_{in} the incident photon flux expressed as number of photons per second, I_{XSW} is the relative intensity of the X-ray standing wave (XSW), $P_{\mathrm{i,j}}$ the photon flux from the fluorescence line j of the element i, $\tau_{Xi}(E_{\mathrm{in}})$ is the photoelectric cross section, $\mu_i(E_{\mathrm{i,j}})$ is the partial photoelectric cross section of the element i, Ω_{det} is the solid angle of detection, ω_{Xi} is the fluorescence yield of the absorption edge Xi and $g_{\mathrm{j},Xi}$ is the transition probability of the fluorescence line j [124].

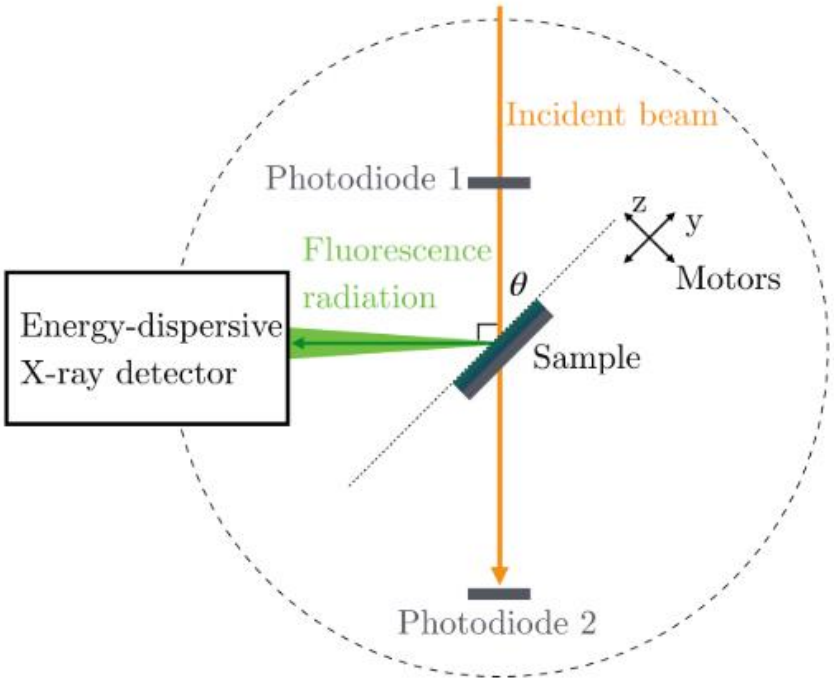

Figure 52**:** Schematic illustration of the GIXRF measurement setup at the FCM beamline of PTB X-ray spectroscopy group at BESSY II. The samples are located on a 9-axis manipulator inside a UHV chamber, allowing for precise variation of the incident X-ray radiation. A calibrated SSD detector is placed perpendicularly to the incident beam direction to collect the fluorescence signal. The two calibrated photodiodes are used for the photon flux measurement and for the sample alignment process.

The uncertainty of the measurements was calculated through standard propagation of uncertainty of the major components reported in equation 2.3. This includes contributions from solid angle (4%), incident photon flux (1.5%), detector efficiency (1.5%), Ti-*K* shell fluorescence yield (3.4%) estimated by Krause *et al.* [125] and Ti-*K* shell photoionization cross-section (5%) for a total relative uncertainty of 8% for all the samples.

$$u^2(y_j) = \sum_{i=1}^{n} u_i^{\,2}(y_j) \tag{2.3}$$

2.4 Results and Discussion

The results presented in the following sections are related to a joint research activity carried out at the X-ray Spectrometry and Radiometry groups at PTB laboratories at synchrotron BESSY II of Helmholtz-Zentrum Berlin (HZB) in

Berlin, Germany, within a Researcher Mobility Grant (RMG) of the EURAMET EMPIR project 20FUN06 MEMQuD.

2.4.1 Geometrical characterization

The first step towards the full characterization of the infiltrated nanostructures relies on the assessment of the geometrical parameters such as the pitch (L_0), the width (W), diameter (d), height (h) and ξ. So far, traditional scanning probe techniques (*e.g.*, AFM) and electron microscopies (SEM and TEM) represent the main tools used on the measurement of different geometrical characteristics. However, a single technique does not have the full capability to provide information on the whole set of geometrical parameters. This requires the integration of multiple tools. For instance, AFM provides quantitative information about nanostructures' h with an associated low level of uncertainty where SEM is not able to. On the other hand, for the lateral dimensions' measurements, SEM is the tool of choice, reaching 1 nm resolution in the xy plane whereas the AFM measurements are impacted by tip convolution. AFM and SEM, despite having a high spatial resolution, can only probe small areas, limiting as a consequence the possibility to perform statistical analysis for comprehensive understanding of the pattern quality, defectivity and homogeneity over the entire sample surface. Statistical information on the morphology and relative size distribution can be directly yielded by traceable GISAXS measurements thanks to the large area probing (square millimeters) determined by the very large footprint of the incident X-ray radiation at grazing angles, providing traceability to the measurements which is crucial when comparing and validating different instruments. Moreover, the GISAXS probing is not limited only to the material surface, but it also extends to the sample volume due to the X-ray penetration, providing depth-resolved information of buried structures by controlling the incidence angle. Figure 53 illustrates the SEM images and relative GISAXS patterns recorded on the reciprocal space q of four BCP samples with different M_w infiltrated with TiO_2 in lamellar (LAM146 and LAM160) and cylindrical (CYL82 and CYL102) morphologies.

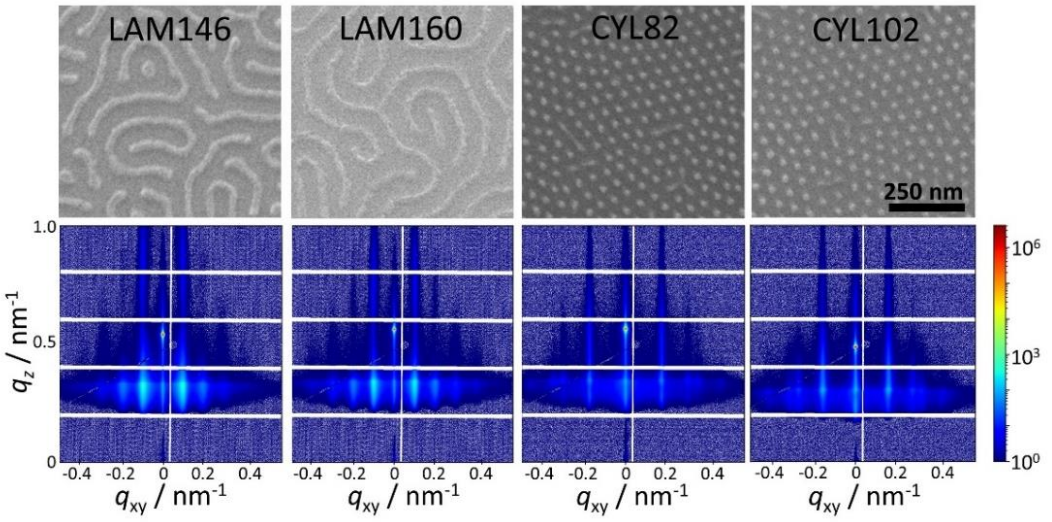

Figure 53: Top-down SEM micrographs of TiO_2 nanostructures obtained by sequential infiltration synthesis of lamellar BCPs with different M_w (LAM146 and LAM160) and cylindrical BCPs with different M_w (CYL82 and CYL102) and relative GISAXS diffraction patterns in the reciprocal q space.

The analysis of the GISAXS patterns were performed by tracing cuts along the q_{xy} at a constant q_z. As illustrated in Figure 54, the GISAXS profile cuts of lamellar nanostructures (LAM146 and LAM160) consist of peaks equidistant from each other. On the other hand, for cylindrical samples (CYL82 and CYL102) the peak positions are scaled following the ratio $1:\sqrt{3}:2:\sqrt{7}$, typical of a 2D hexagonal lattice which validates the hexagonal packing of self-assembled cylindrical BCPs.

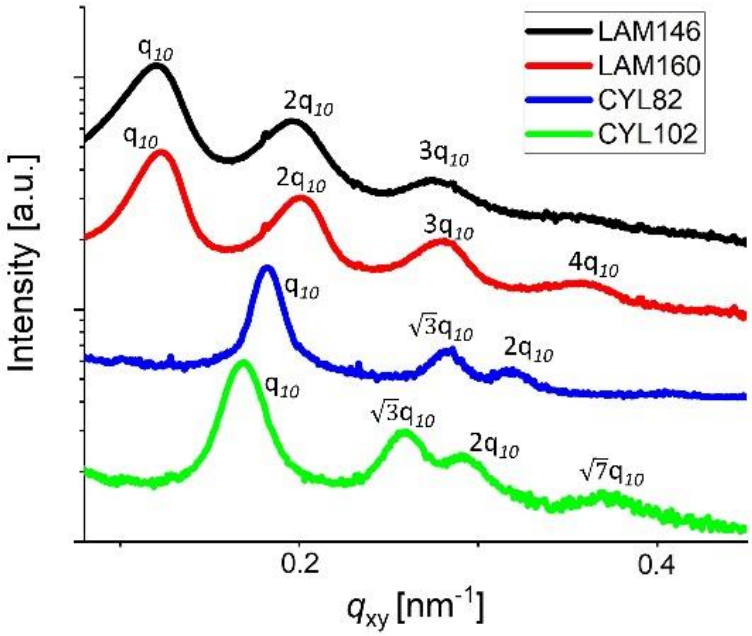

Figure 54: Horizontal intensity profiles at constant q_z of the lamellar and cylindrical samples.

Geometrical information on the lateral periodicity of the nanostructures can be extracted by assessment of the diffraction order peaks positions. The specific distance of the primary diffraction maximum to the zero-diffraction order directly provides the lamellar nanostructures' pitch (L_0) following the expression [126]:

$$L_0 = \frac{\lambda L_S}{d_{px}} \tag{2.4}$$

in which λ is the incident beam wavelength, L_s is the sample-detector distance and the d_{px} is the zero-first diffraction order distance. Whereas the L_0 of cylindrical nanostructures in a two-dimensional hexagonal lattice is expressed as [55]:

$$L_0 = \frac{2\lambda L_S}{\sqrt{3}d_{px}} \tag{2.5}$$

The results of L_0 values for the sets of samples under investigation are reported in Table 2.

Table 2: Pitches (L_0) values and related dispersion and combined standard uncertainty.

Samples	L_0 [nm]	Dispersion [nm]	$u_c(L_0)$ [nm]
LAM146	68.2	5.5	0.2
LAM160	67.4	4.1	0.2
CYL82	44.1	0.9	0.2
CYL102	48.8	1.3	0.1

By a comparison on both lamellar and cylindrical samples, one can notice some incongruencies on the pitch values in function of the M_w of the starting block copolymers, which shows L_0 value of sample LAM146 (68.2 ± 5.5) nm, slightly higher when compared to sample LAM160 (67.4 ± 4.1) nm. Although a lower M_w block copolymer template was employed on the fabrication of sample LAM146 with respect to the one used for sample LAM160, the discrepancies on the expected pitches values can be accounted for the higher polydispersity index (PDI = 1.20) which reflects also into a broader pitch dispersion. As reported in literature, the increase of PDI directly leads to an increase of the nanostructures' domain size and spacing [127]. The recent advances in polymerization processes led to the development of synthetic techniques such as controlled radical polymerization that, however, result into BCPs with relatively broader molecular weight distributions than those typically obtained by living anionic, cationic, or metal-catalyzed techniques [128]. The great influence of the PDI impaired to the geometrical characteristics of the resulting nanostructures, poses challenges on the employment of BCPs for nanoscale metrology due to potential inconsistency of the measurand (*e.i.* pitch) which may vary depending on the different synthetic routes applied for the synthesis of BCPs with the same M_w by different research groups. Therefore, the best metrology practice to overcome this issue would be represented by a judicious choice of the most appropriate synthetic method to be applied for a specific BCP. Cylindrical samples (CYL82 and CYL102) however, exhibit a clear increase of the L_0, consistent with the M_w. In Table 2 is also reported the combined standard uncertainty $u_c(L_0)$, determined according to the

Guide to the Expression of Uncertainty in Measurement (GUM) [124]. The $u_c(L_0)$ was calculated by summing the absolute squares of all uncertainty contributions from the input parameters as reported in Table 3.

Table 3: Uncertainty contributions estimated for the FCM beamline on GISAXS measurements [129] of input parameters χ_i, and related uncertainty components according to GUM [130].

Input quantity	$u(\chi_i)$	$\frac{u_i(\chi_i)}{\chi_i}$
Photon energy E_{ph}	1 eV	1.0×10^{-4}
Sample-detector distance L_s	3 mm	1.0×10^{-3}
Pixel size L_{px}	0.2 µm	2.9×10^{-3}
Zero-first order distance d_{px}	≤ 0.87 px	1.6×10^{-3}

The major contribution to the $u(L_0)$ derives from the photon energy E_{ph}, sample-detector distance L_s, pixel size L_{px} and the distance between the zero and first diffraction order d_{px}. Further analysis of the GISAXS patterns can be applied in order to extract information about the long-range lateral ordering of the nanostructures. To this end, the first Bragg order peak width provides direct information on the ξ of self-assembled pattern following the relation [126]:

$$\xi = \frac{\lambda L_S}{FWHM} \tag{2.6}$$

in which λ is the incident beam wavelength, L_s is the sample-detector distance and FWHM is the full width at half-maximum of the Gaussian fitting of the first diffraction order. As reported in Figure 55, all samples, whether lamellar or cylindrical morphologies, exhibit high ξ values exceeding 400 nm. However, two distinct evolutions on the ξ can be observed for lamellar (LAM146 and LAM160) and cylindrical (CYL82 and CYL102) nanostructures. Both sets of samples underwent to two different self-assembly processing parameters, respectively. Lamellar BCP were annealed by RTP at 230 °C for 600 s, whereas the cylindrical samples were thermally treated in RTP at 190 °C for 450 s. Higher M_w lamellar sample LAM160 shows higher ξ value (540.2 ± 105.1) nm when compared to a

lower M_w LAM146 (426.6 ± 106.6) nm, thus indicating more favorable thermal annealing conditions to promote the self-assembly process of high M_w BCPs. On the contrary, in cylindrical samples CYL82 and CYL102, by monitoring the ξ evolution, one can notice an opposite trend with respect to the lamellar ones. Under these processing conditions, the thermal annealing promotes an increased nanostructure ordering for lower M_w BCPs CYL82 (838.7 ± 209.7) nm compared to lower M_w BCPs CYL102 (707.4 ± 176.8) nm. It must be noted however, that the overall high confidence intervals lead to no significant differences among the ξ values due to overlap of the relative error bars represented as 1σ [131].

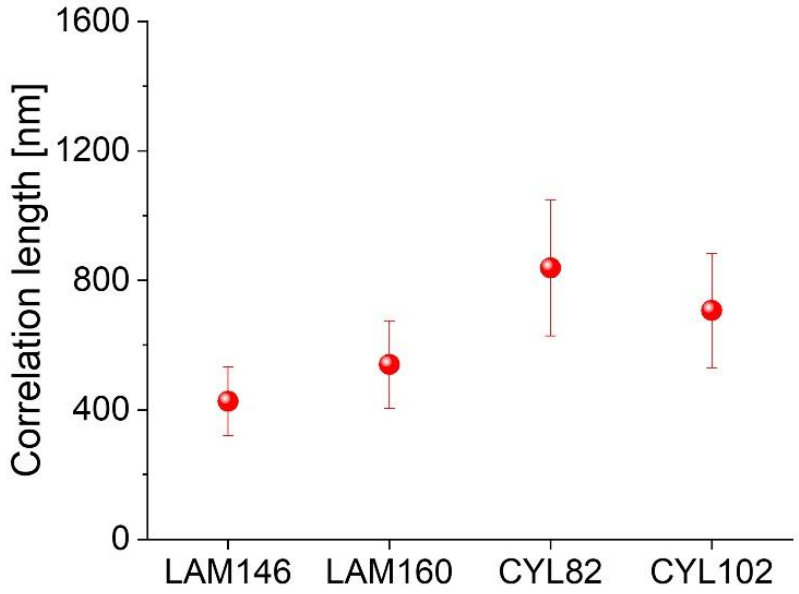

Figure 55: Correlation lengths (ξ) as a function of the molecular weight of the BCP template for lamellar (LAM146 and LAM160) samples annealed by RTP at 230 °C for 600 s and cylindrical (CYL82 and CYL102) samples annealed by RTP at 190 °C for 450 s. The error bars represent 1σ due to uncertainty in the fit [131].

Although GISAXS provides straightforward information on the pitch and correlation length, the assessment of other geometrical parameters as height and width would require additional modeling. Previous works demonstrated the capability of GISAXS to fully reconstruct the critical parameters as the line widths and heights of perfectly aligned grating structures thanks to the possibility to reduce the computational domain in a 2D model [132]. However, due to the disordered and fingerprint-like pattern of self-assembled nanostructures, this approach would significantly increase the overall computational effort. In this scenario, complementary analysis would provide morphological information

otherwise not accessible with X-ray scattering methods. Specifically, AFM was employed to measure the height of the nanostructures. The measurements were conducted in tapping mode in ambient conditions over a 1 µm x 1 µm and 2 µm x 2 µm areas (Figure 56), revealing dissimilar heights of lamellar and cylindrical nanostructures.

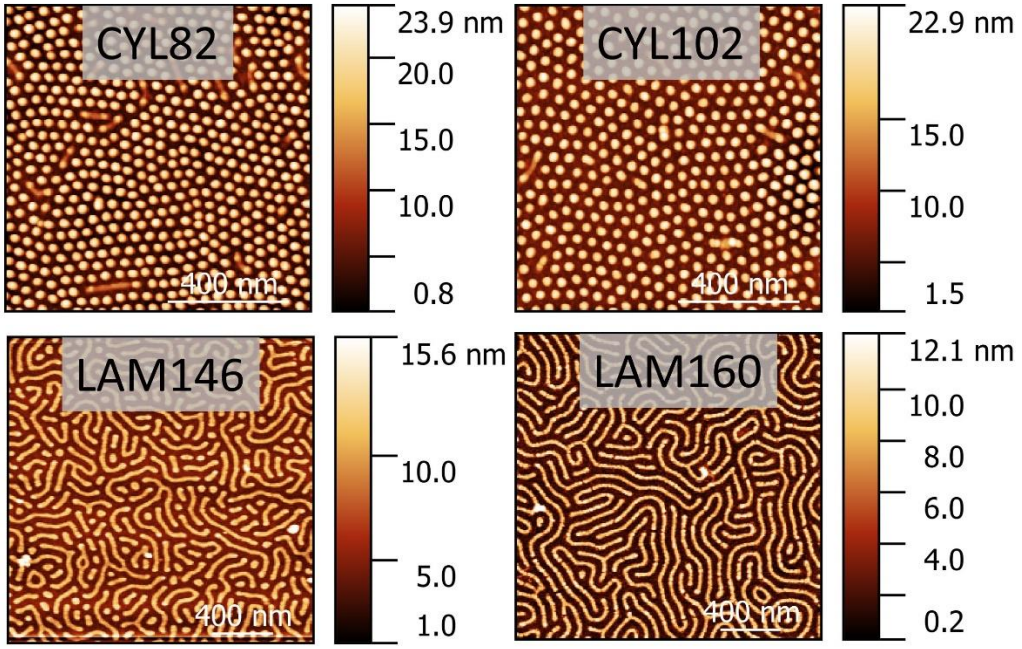

Figure 56: Representative AFM micrographs of TiO_2 nanostructures on measurement fields 1 x 1 μm^2 (CYL82 and CYL102) and 2 x 2 μm^2 (LAM146 and LAM160).

The lamellar nanostructures are characterized by a reduced height when compared to the cylindrical ones (Table 4). There are three major contributions that determine the resulting nanofeatures' heights: the BCP film thickness spin-casted on the substrate, the TiO_2 mass uptake and the PMMA block volume fraction. All samples were fabricated following the same spin-coating parameters therefore, depositing the same polymeric film thickness of nominally 35 nm. Moreover, all the samples underwent the same infiltration conditions, preventing therefore any process-to-process variation of metalorganic precursor concentration inside the ALD chamber. Therefore, the striking increased height of the cylindrical features (around 10 nm higher) with respect to the lamellar nanostructures, can be attributed to the lower PMMA volume fraction (~30%) when compared to the lamellar ones (~50%). The reduced volume fraction of the reactive polymeric phase (PMMA) in hexagonally packed cylindrical

configuration, imposes lateral restrictions on the growth of inorganic material. As a consequence, the metal oxide deposition distributes along the *z* axis, resulting in an overall increased nanofeatures height.

Table 4: TiO_2 nanostructures' heights measured by AFM.

Samples	TiO_2 height [nm]	Dispersion [nm]
LAM146	6.9	2.6
LAM160	7.7	2.0
CYL82	17.6	2.1
CYL102	17.0	2.2

The morphological analysis was complemented by SEM investigation. The nanostructures' width (*W*) and diameter (*d*) determination was performed by FFT analysis of the SEM micrographs (Figure 57). A set of representative SEM images at different magnifications were acquired for each sample. The second order radial averaging fitting provides information on the typical lateral dimensions of the nanofeatures that are reported in Table 5.

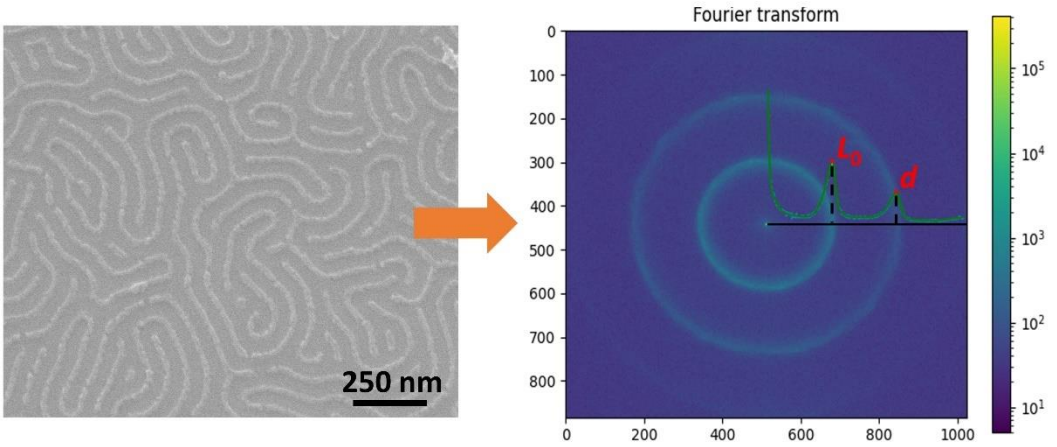

Figure 57: Representative SEM micrographs of sample LAM160 and workflow for the determination of lamellae width by fitting of the second order radial averaging.

The presented *d* and *W* results derive from the averaging of at least 10 SEM images collected in random locations of each sample over the entire sample surface and expressed with relative standard deviation of the mean peak position. The cylindrical samples show a coherent relation of *d* as a function of the M_w, from 19.0 ± 2.0 nm for CYL82 to 22.7 ± 1.0 nm for CYL102, validating the expected tendency of nanostructure's dimensional increase along with the BCP template M_w. Whereas the *W* of TiO_2 lamellar features is quite similar for both LAM146 (34.6 ± 0.9 nm) and LAM160 (34.1 ± 0.5 nm) that can be accounted for the higher PDI of PS-*b*-PMMA with M_w = 146 kg/mol. Since the GISAXS measurements revealed a relatively high L_0 dispersion, one might expect a wide dispersion on the *W* values as well. However, the relatively low measured *W* dispersion of LAM146 (± 0.9 nm) could be related to the lower statistical information evaluated on the FFT analysis of a limited number of SEM images when compared to the larger analyzed area due to the wide footprint of X-ray scattering at grazing angles.

Table 5: TiO_2 nanostructures' lateral dimensions measured by FFT analysis of SEM images.

Samples	**TiO_2 *W* [nm]**	**Samples**	**TiO_2 *d* [nm]**
LAM146	34.6 ± 0.9	**CYL82**	23.0 ± 2.0
LAM160	34.1 ± 0.5	**CYL102**	24.5 ± 1.0

The calculation of the area covered by the TiO_2 nanostructures was conducted by ImageJ software analysis (Table 6). In order to analyze the pattern, the TiO_2 nanostructures were identified and separated by auto-thresholding plugins available for ImageJ software. However, the manual contrast enhancement performed the SEM micrograph acquisition, can be responsible for considerable image-to-image variations of the contrast, resulting therefore in covered area values that might be affected by operator variations.

Table 6: TiO_2 nanostructures' covered area percentage.

Samples	Covered area	Samples	Covered area
LAM146	36.1%	**CYL82**	20.3%
LAM160	40.4%	**CYL102**	20.5%

2.4.2 Chemical speciation

Once defined the geometrical parameters on the synthesized nanostructures by means of complementary tools as GISAXS, AFM and SEM, the comprehensive characterization of the infiltrated TiO_2 requires the assessment of the effective material composition and the chemical speciation. To this end, near-edge X-ray absorption fine structure spectroscopy (NEXAFS) ensures the identification of chemical valence states in nanomaterials providing in-depth information depending on the angle of incidence and photon energy.

NEXAFS measurements on the infiltrated TiO_2 nanostructures were carried out at the plane grating monochromator (PGM) beamline in the soft X-ray regime (E_{ph} < 1 keV) at PTB spectrometry group at BESSY II by varying the photon energy in the range of 450 – 480 eV and 525 – 550 eV to investigate the fine structure of the X-ray absorption of Ti $L_{2,3}$-edge and O K-edge, respectively. The NEXAFS setup follows the same geometry of the GIXRF setup described previously and the measurements were realized in fluorescence mode, implying that a fluorescence spectrum is acquired for every photon energy by an SDD detector and subsequently normalized to the incident photon flux and detector efficiency [133].

In Figure 58a are illustrated the NEXAFS spectra of Ti $L_{2,3}$-edge of the TiO_2 samples fabricated by sequential infiltration synthesis (LAM146, LAM160, CYL82 and CYL102) for an incidence angle of 30°. The peak positions of the four curves related to the infiltrated samples perfectly overlap each other, suggesting that there are no differences on the chemical binding states. The $L_{2,3}$ absorption peaks split in two main groups separated by ~5.5 eV related to the L_2 and L_3-edges respectively. The material under consideration exhibits a very broad L_2-edge, dominated by D_2 peak along with a broadened D_3 peak in the L_3-edge.

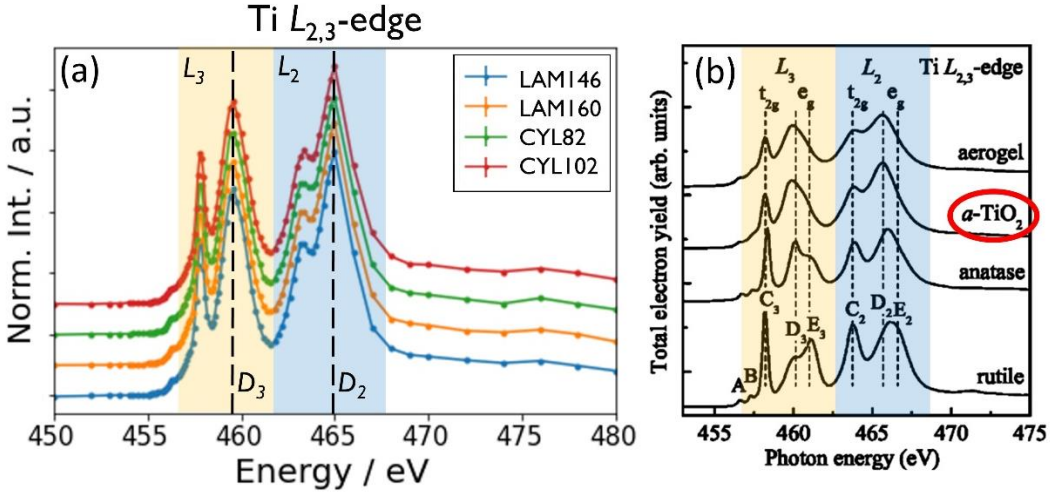

Figure 58**:** Ti $L_{2,3}$-edge spectra of (a) TiO_2 fabricated by sequential infiltration synthesis (LAM146, LAM160, CYL82 and CYL102) and (b) Ti $L_{2,3}$-edge spectra of rutile, anatase, amorphous TiO_2 (a-TiO_2), and a titania aerogel. (b) Adapted from [134].

A comparison of these spectra to those reported in literature [134] (Figure 58b) clearly suggests that the infiltrated TiO_2 is amorphous. Moreover, the absence of any peaks related to other Ti species indicates a complete oxidation of TiO_2, confirming the 1:2 stoichiometry of Ti and O. As a comparison to the samples fabricated by SIS, three TiO_2 thin films deposited by conventional ALD with three different thicknesses (10, 20 and 30 nm) were measured at the same experimental conditions. Figure 59 shows that, in TiO_2 thin layers fabricated by ALD, the peaks intensities, positions and widths follow a completely different evolution along the film thickness. In thicker ALD layers of 30 nm the C_2 and D_2 peaks in L_2-edge spectra show a different intensity ratio, typical of the anatase polymorph, confirmed also by the e_g related peaks of L_3-edge that split into two peaks, predominantly dominated by D_3. By reducing the TiO_2 to 20 and 10 nm, one can notice an overall progressive evolution of the peak intensities. The reduced film thickness induces variations of peak intensity ratios in the L_2 and L_3-edge regions with a progressive shift of D_2 and D_3 peaks to lower energies along with a substantial increase in intensity. This behavior can be attributed to a gradual amorphization of the anatase crystalline phase for reduced film thicknesses.

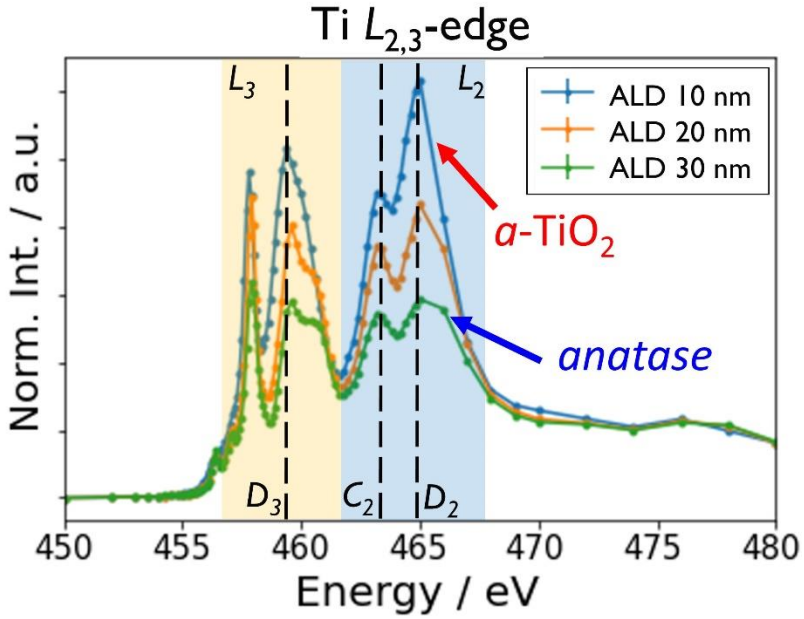

Figure 59**:** Ti $L_{2,3}$-edge spectra of TiO_2 thin films fabricated ALD with different thickness (10, 20 and 30 nm).

Confirmation of the amorphization process of TiO_2 thin films with reduced thickness is provided also by O *K*-edge NEXAFS spectra in Figure 60a,b. Here, the significant distance reduction between C_0 and E_0 peaks is caused by a shift of E_0 to lower energies accompanied by a broadening of all the peaks in the spectra.

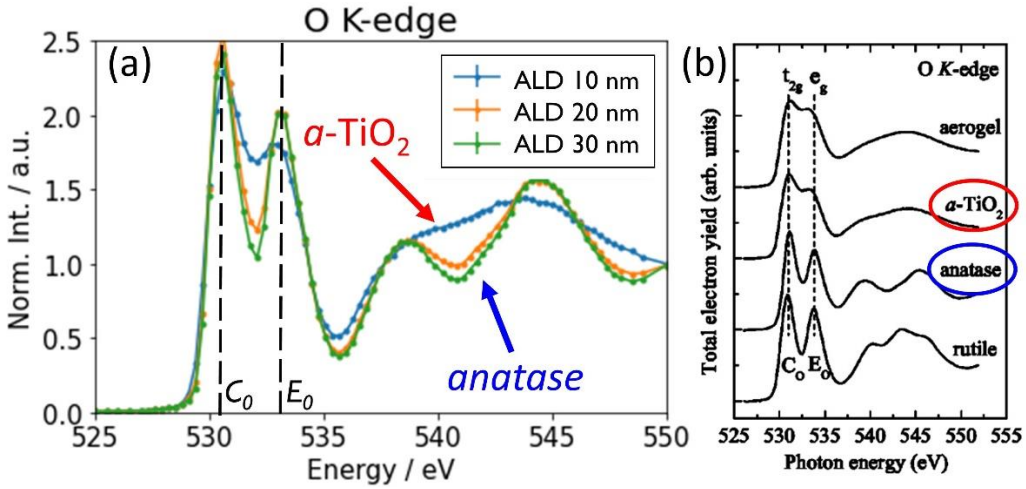

Figure 60**:** O *K*-edge spectra of (a) TiO_2 deposited by ALD with different thickness (10, 20 and 30 nm) and (b) rutile, anatase, amorphous TiO_2 (a-TiO_2), and a titania aerogel. (b) Adapted from [134].

2.4.3 Analytical and dimensional nanometrology and validation

The use of complementary X-ray spectrometry analytical tools, such as X-ray reflectometry (XRR) and GIXRF, in conjunction with radiometrically calibrated instrumentation of PTB at BESSY II, provide both reference-free quantification as well as the knowledge/reconstruction of the in-depth material composition [135]. When XRR is applied to nanometric thin layer samples, the angular oscillations reveal dimensional information such as the layer thickness (d) as well as the material density (ρ). In GIXRF, on the other hand, the angular and depth-dependent changes of the X-ray standing wave (XSW) intensity field distribution provides depth-dependent information on the material mass deposition (m_i/F_i). The direct relationship of the physical quantities that can be deduced by XRR and GIXRF, where $d\rho = m_i/F_i$, allows for a combined analysis of the data derived from the two analytical techniques. The implementation of an additional photodiode on a separate 2θ axis on the GIXRF measurement setup, described previously, allows for the in-parallel conduction of XRR and GIXRF measurements. In this combined GIXRF-XRR measurement methodology, one can take advantage of the elemental mass deposition information of each element provided by GIXRF and distribute them along the film thickness. This determines a significant reduction of the free parameters on the combined GIXRF-XRR modeling for an overall improved reliable data interpretation as compared to conventional modeling approaches.

For nanostructured materials however, the overall increased complexity of such systems requires additional combined GIXRF-XRR data modeling effort in comparison to thin films [136]. The increased modeling complexity of nanostructured materials extends that of continuous thin films, involving assumptions on additional geometrical information such as the nanofeatures height, width, diameter and pitch. The larger set of geometrical information required to describe the nanostructures, directly leads to a larger number of free modeling parameters that can easily suffer from cross correlation issues, interparameter dependencies or incomplete model assumption, yielding therefore to possible falsified results of derived physical quantities such as mass density and refractive index of the material of interest. This issue can be addressed by a validation scheme that relies on the intercomparison of results derived from different characterization techniques that aim at the same physical quantity. Although each characterization technique is related to a different measurand, the implementation of geometrical information obtained by complementary dimensional analytical techniques as modeling restrictions, allows for a more

reliable interpretation and mutual validation of the resulting data. To this end, the assessment of the geometrical information of infiltrated TiO_2 nanostructures is described in the previous section, where GISAXS, AFM and SEM investigations were performed to measure the pitch, width, diameter and height. The geometric parameters are summarized in Table 7.

Table 7: Geometric parameters and related dispersions of nanostructured infiltrated TiO_2 samples measured by GISAXS, AFM and SEM used for validation of GIXRF-XRR modeling.

Parameters	CYL82	CYL102	LAM146	LAM160
(GISAXS) pitch [nm]	44.1 (0.9)	48.8 (1.3)	68.2 (5.5)	67.4 (4.1)
(AFM) height [nm]	17.6 (2.1)	17.0 (2.2)	6.9 (2.6)	7.6 (2.0)
(SEM) diameter [nm]	23.0 (2.0)	24.5 (1.0)	/	/
(SEM) width [nm]	/	/	34.6 (0.9)	34.1 (0.5)
(SEM) covered area	20.3%	20.5%	36.1%	40.4%

The reference-free GIXRF, applied at incident angles above the critical angle of total reflection, provides absolute quantification of the mass deposition without requiring any modeling. Figure 61 illustrates the angle-dependent X-ray fluorescence profiles of Ti-K_α of the infiltrated TiO_2 nanostructures for grazing-incidence angles of a 6 keV beam energy in the range from 0.0° to 2.5°.

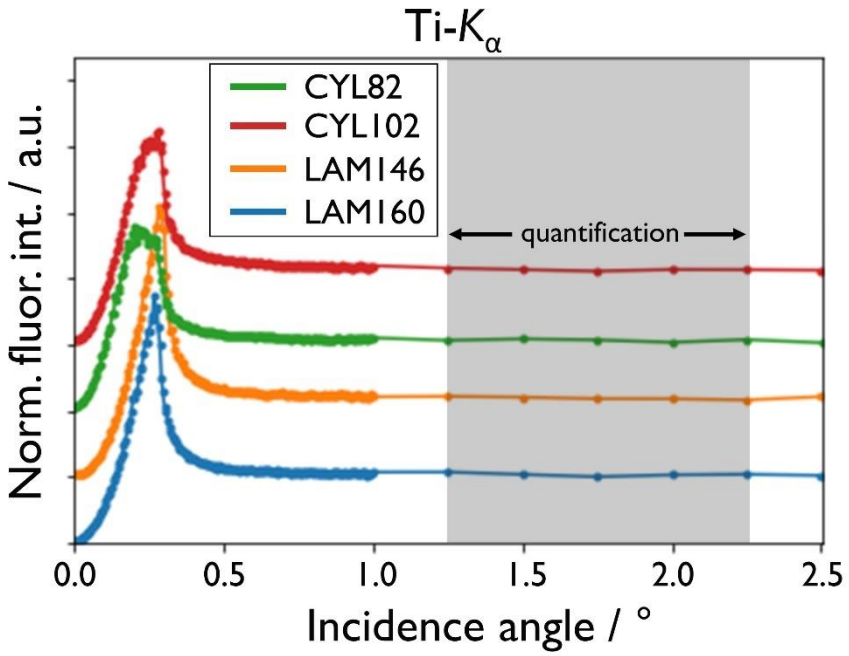

Figure 61: Ti-K_α GIXRF spectra for infiltrated TiO_2 nanostructures measured at FCM beamline with a 6 keV incident beam energy. The data in the angular range above the critical angle for total external reflection (highlighted in grey) can be used for the quantification of the element of interest.

The GIXRF spectra are characterized by modulations of the fluorescence intensity at incident angles in the range from 0.0° to 0.5° due to XSW field interactions with the nanostructures for all the analyzed samples. At incidence angles higher than the critical angle of total external reflection (from 1.25° to 2.25°) where no XSW is present, a traceable reference-free quantification of the mass deposition can be performed by a good knowledge of the uncertainty contributions of the instrumental parameters in terms of solid angle of detection (4%), incident photon flux (1.5%) and detector efficiency (1.5%), as well as of the fundamental parameters such as Ti-*K* shell fluorescence yield (3.4%) estimated by Krause *et al.* [125] and Ti-*K* shell photoionization cross-section (5%), for a total uncertainty of 8% (Table 7). Additional XRF measurements were performed for the quantification of residual C at the PGM beamline in the PTB laboratory at the BESSY II electron storage ring. The experiments were conducted at an incidence angle of 15° and incident photon energy of 520 eV, which is below the Si *K*-edge in order to suppress the contribution of the Si-*K* XRF lines [137]. The uncertainty made in the quantification of C depends on the uncertainties on the incident flux (1%), fluorescence yield (10%), photoionization cross-section, (7.5%), the

detector efficiency and spectral deconvolution (2.5%), the counting statistics and the solid angle of detection (15%) for a total uncertainty of 20% (Table 8).

Table 8: Absolute Ti and C mass depositions and related uncertainties.

Samples	Ti mass deposition [ng/cm^2]	*u* [%]	C mass deposition [ng/cm^2]	*u* [%]
LAM146	228.1	8	300.0	20
LAM160	259.8	8	365.0	20
CYL82	226.4	8	378.0	20
CYL102	238.7	8	354.0	20

The overall similar Ti mass depositions quantified by GIXRF, that vary in the range from 226.6 to 259.8 ng/cm^2 for both lamellar and cylindrical samples, indicate that no substantial differences occur on the mass uptake of TiO_2 upon sequential infiltration synthesis independently of the molecular weight (M_w) of the BCP template. The absolute quantification of Ti, performed through GIXRF, are consistent with the known infiltration mechanism in PS and PMMA. The comparable mass uptake of TiO_2 can also be confirmed by the differences on the nanostructure heights when comparing lamellar to cylindrical features. The significant increased height of the cylindrical nanostructures measured by AFM, of around 10 nm higher than lamellar structures, can be attributed to the lower volume fraction of the reactive polymeric phase in cylindrical BCP templates. As discussed in section 2.4.1, the lateral restrictions imposed by a reduced volume fraction of cylindrical BCP domains, directs the growth of TiO_2 along the polymeric film thickness, eventually resulting in an increased infiltrated nanostructures height. The simultaneous conduction of the GIXRF-XRR measurements allows for the combined modeling of the nanostructured samples taking advantage of the known nanostructure density and height obtained by the GIXRF quantification [135]. The resulting TiO_2 depth profiles of the infiltrated nanostructures of both lamellar samples (LAM146 and LAM160) cylindrical (CYL82 and CYL102) samples are shown in Figure 62 and Figure 63, respectively. The orange line indicates the variation of Ti concentration along the nanostructures' height. The comparable Ti mass uptakes, quantified by reference-

free GIXRF, for all the samples that underwent to the same infiltration processing parameters, however, result in a completely different distribution along the nanostructures' depth-profile. For lamellar samples LAM146 and LAM160, as illustrated in Figure 62, the Ti concentration is maximum on the top and on the lowest part of the nanostructures with a sharp Ti concentration decrease down to zero at about half-height along the z-axis. The inhomogeneous Ti in-depth distribution could be related to a low polymeric chain mobility associated to the high M_w of the relative BCP templates, hindering an efficient channeling of the metalorganic precursors in the deeper part of the PMMA nanodomain. This prevents a homogenous infiltration of the metalorganic precursor along the entire BCP template height, leading to a TiO_2 growth predominantly on the upper part of the nanostructures. On the other hand, a maximum Ti concentration revealed at the bottom, right above the substrate, can be associated to the infiltration of the random copolymer layer underneath the nanostructures. As reported by Caligiore *et al.*, [138], in SIS process, the underlying PS-*r*-PMMA brush layer is infiltrated too, creating a continuous metal oxide layer on top of the substrate's surface in which the total amount of infiltrated inorganic material is directly proportional to the MMA volume fraction of the RCP.

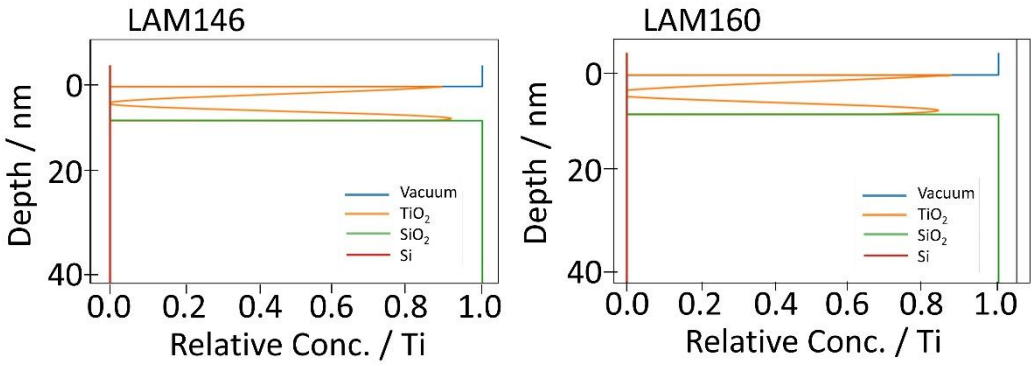

Figure 62: Ti concentration depth profiles determined using the hybrid GIXRF-XRR modeling of lamellar TiO_2 nanostructures.

On cylindrical sample CYL82 (Figure 63), the Ti concentration follows a similar distribution to the lamellar ones, with a maximum value on both the top and bottom of the depth-profile. In this case, however, a relative concentration increase can be noticed at about half-depth. The higher PS volume fraction in cylindrical BCPs results in a better diffusion of the metalorganic precursors inside the BCP thin film, with respect to high-M_w BCPs, thanks to its high free volume and chemical incompatibility with the $TiCl_4$ reactant. Cylindrical sample

CYL102, when compared to CYL82, shows a more homogenous distribution of the Ti concentration along the nanostructure height. In these samples, one can notice the absence of a Ti concentration maxima on the top, but instead the mass uptake is more evenly distributed resulting in gradient-like in-depth profile, while still revealing the infiltration of the random copolymer layer on the lower part. The overall Ti concentration distribution along the z-axis for all samples clearly indicates a porosity related to the infiltrated material that could be explained by the diffusive nature of the SIS. In this synthetic approach the metal oxide growth follows a nucleation process on specific nucleation sites inside the reactive polymeric domain [138]. The distribution of the reactive functional groups of the polar polymeric domain (PMMA) determines an inhomogeneous TiO_2 growth within the polymer which eventually results in a final amorphous structure, as validated by NEXAFS experiments (Figure 58).

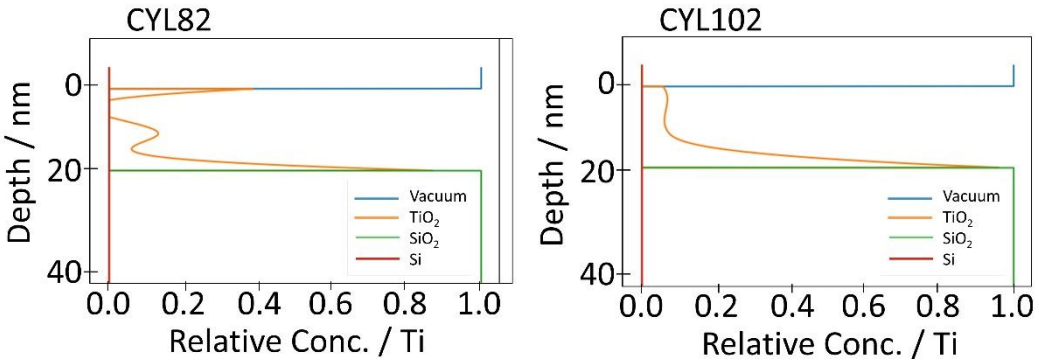

Figure 63**:** Ti concentration depth profiles determined using the hybrid GIXRF-XRR modeling of cylindrical TiO_2 nanostructures.

The validation of the XRR-GIXRF modeling results is represented by the good agreement on the determination of the TiO_2 nanostructures' heights calculated from the hybrid model in comparison to the experimental measurements obtained by AFM. As shown in Figure 64, the hybrid model data are consistent with those taken by AFM measurements within the confidence intervals [139].

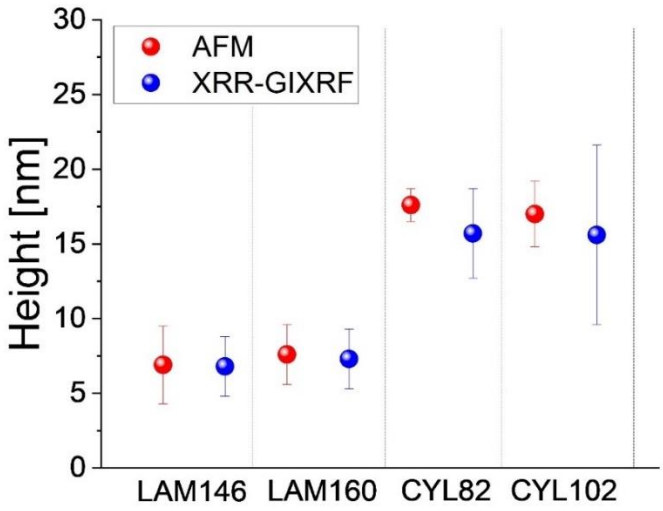

Figure 64: Comparison of the infiltrated TiO_2 height values obtained by AFM and XRR-GIXRF hybrid modeling. Confidence intervals (1σ) of the hybrid model derived from Markov chain Monte Carlo analysis [139].

The additional XRF measurements at lower incident beam energy (520 eV) reveal some noticeable amount of C, in the range from 300 to 378 ng/cm^2, much higher than the quantified Ti mass deposition. The overall high quantity of C still present on the nanostructures, as reported in Table 7, might be attributed to an incomplete removal of all the organic material infused with TiO_2 after subsequent Ar plasma treatment. Although being in isotropic conditions, Ar plasma does not chemically react with the polymeric matrix, thus the etching process is reduced to a physical sputtering that leads to a significant graphitization of the polymeric template with direct impact on the mass density and optical properties of the resulting organic/inorganic composite material. This issue might be overcome by O_2 plasma etching processes in which the additional chemical sputtering effects of O_2 to the physical one, determine a rapid oxidation and ion-induced desorption that would prevent the formation of residual C [140,141].

As shown in the previous section, NEXAFS analysis revealed a chemical binding state of the infiltrated TiO_2 that can be attributed to a stoichiometric amorphous phase. Assuming a 1:2 molar ratio of Ti:O and total quantification of Ti and C and given the geometrical parameters as nanostructures' height and surface covered area by GISAXS, SEM and AFM analysis, one can calculate the mass density of infiltrated nanostructures per unit area (Table 9). It should be noted that this assumption considers the total amount of Ti quantified by GIXRF,

including the Ti quantification associated to the infiltration of the RCP layer underneath the TiO_2 nanostructures. For a more correct calculation of the mass density, one should consider the mass deposition of the Ti infiltrated into the BCP template only. In the present measurements, the subtraction of the contribution of Ti infiltrated into the RCP layer, is prevented by the incapability to discriminate the Ti mass deposition associated to the infiltration of the RCP form the total Ti mass deposition. The relative refractive indices can be determined following the direct correlation between the mass density values calculated by XRF mass quantification and refractive index for TiO_2 established by Otterman and Bange [142]:

$$\rho = 2.83n - 3.27 \tag{2.7}$$

where ρ is the mass density and n the refractive index at 550 nm (Table 9).

Table 9: Calculated mass densities ($\boldsymbol{\rho}$) of infiltrated TiO_2 nanostructures using the reference-free XRF quantification of Ti and C and the nanostructures' volume extracted from GISAXS, SEM and AFM analysis and relative refractive indices n following eq. 2.7 [142].

Samples	ρ [g/cm^3]	n (550 nm)
LAM146	2.74	2.12
LAM160	2.59	2.07
CYL82	2.13	1.91
CYL102	2.21	1.94

A parallel assessment of the optical properties can be performed by spectroscopic ellipsometry analyses on the infiltrated samples by using an alpha-SE ellipsometer, J.A. Wollam Co with spectral range of 300-900 nm at a fixed angle of 70° to monitor the refractive index evolution. This method takes advantage of all the geometrical (pitch, height, width, diameter) and analytical (chemical speciation and stoichiometry) information obtained by complementary techniques and used to parameterize a Bruggeman EMA model using the COMPLETE EASE software. Specifically, the EMA model consists of a mixture of materials composed of amorphous TiO_2 and PMMA. The refractive indices of

the constituent TiO_2 were extracted at a wavelength of 550 nm by ellipsometry measurements of TiO_2 thin films fabricated by conventional ALD (Figure 65). The refractive indices exhibit a linear increase for increasing TiO_2 film thicknesses, validating therefore the NEXAFS measurements on the same set of ALD samples reported in the previous section (Figure 59), that illustrated a clear evolution of the crystalline phase of deposited TiO_2, from amorphous for 10 nm thin films to anatase polymorph for 30 nm thin films. For 30 nm thin films of TiO_2, a refractive index of 2.53 at 550 nm is in good agreement with the tabulated value of a bulk anatase polymorph (n = 2.65 at 550 nm) [143] and consistent with previous works by Aarik *et al.*, [144] where TiO_2 grown by $TiCl_4$-H_2O ALD process begins to crystallize at a growth temperature of approximately 150 °C and at a critical thickness of around 15 nm. On the other hand, the lower value of refractive index of a 10 nm thin film (n = 2.36 at 550 nm) corresponds to a lower density when compared to a crystalline TiO_2, therefore related to an amorphous TiO_2 phase. Another confirmation of the crystalline phase of the deposited TiO_2 is provided by the mass density values calculated from the direct correlation between refractive index measured by ellipsometry and mass density for TiO_2 following eq. 2.7. The mass density calculated by this correlation for a 30 nm thin TiO_2 layer is 3.9 g/cm^3, perfectly matching the reported mass density of bulk anatase [145]. The reduced refractive indices of 10 and 20 nm thin films result also in a lower mass density of 3.4 and 3.7 g/cm^3 respectively, in accordance with mass densities of amorphous TiO_2 that typically range from 2.9 to 3.9 g/cm^3 [146].

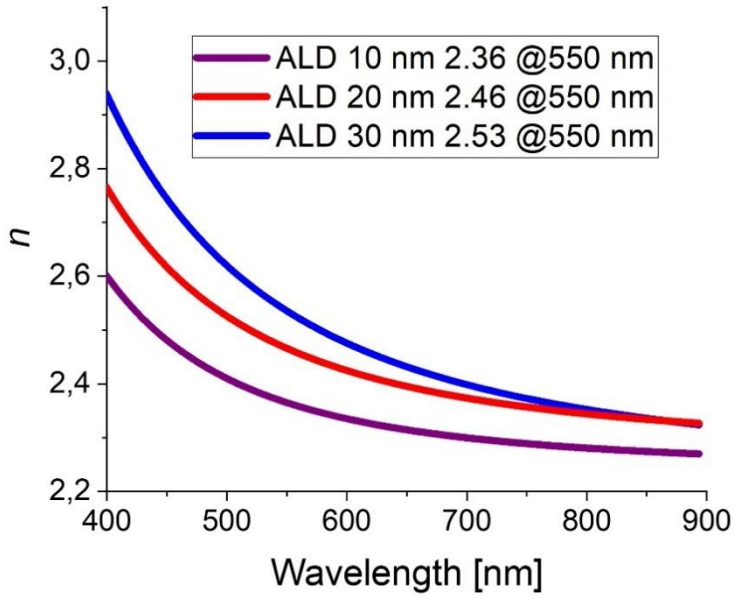

Figure 65**:** Refractive indices *n* extracted from ellipsometry measurements of thin films of TiO_2 deposited by ALD.

The chemical similarities on the binding states of infiltrated TiO_2 and 10 nm thin films deposited by ALD, as confirmed by NEXAFS analysis, allow for the implementation of the 10 nm thin film and its related optical constants as a starting material in the present EMA model with progressively reduced refractive index along with an increased PMMA volume fraction. Whereas the geometrical parameters as nanostructures' heights and surface covered area, were extracted by the GISAXS, SEM and AFM analyses and implemented in the model as fixed restrictions limiting, consequently, the number of free parameters. The ellipsometric data were fit to the model revealing an overall reduced *n* for all the infiltrated samples compared to a 10 nm thick TiO_2 deposited by ALD with a progressive decrease along with the M_w of the starting BCP template (Figure 66a). The linear dependency of the refractive index with respect to the PMMA volume fraction in the TiO_2/PMMA composite indicates the presence of high quantities of residual PMMA inside the amorphous infiltrated TiO_2 from ~20% up to around 50% in volume (Figure 66b).

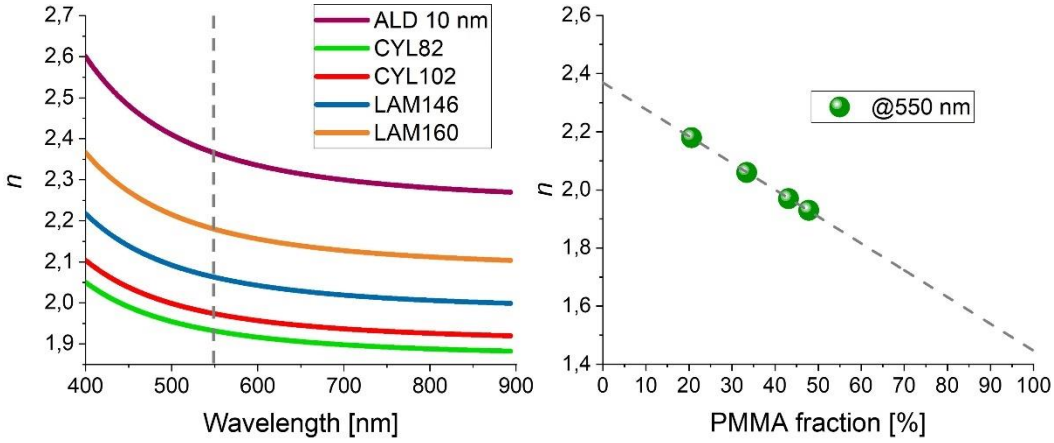

Figure 66: (a) Refractive indices *n* extracted from ellipsometry measurements of 10 nm thin TiO_2 films by ALD and infiltrated samples assuming an EMA model constituted by amorphous TiO_2 and PMMA. (b) Refractive indices *n* at 550 nm of infiltrated samples as a function of the volume fraction of residual PMMA.

As reported in Table 10, the direct comparison of the mass densities and refractive indices derived from the absolute XRF quantification and ellipsometric measurements reveal good consistency, showing low levels of mismatch around 3 to 7% for all the samples under consideration, clearly indicating that the ellipsometry modeling yields comparable results to those determined by reference-free XRF quantification.

Table 10: Comparison of mass densities ($\boldsymbol{\rho}_1$) and relative refractive indices (n_1) determined by reference-free XRF quantification of Ti and C and the nanostructures' volume extracted from SEM and AFM analysis with mass densities ($\boldsymbol{\rho}_2$) and relative refractive indices (n_2) at 550 nm determined by spectroscopic ellipsometry.

Samples	$\boldsymbol{\rho}_1$ [g/cm^3]	$\boldsymbol{n}_1$	$\boldsymbol{\rho}_2$ [g/cm^3]	$\boldsymbol{n}_2$
LAM146	2.74	2.12	2.81	2.15
LAM160	2.59	2.07	2.42	2.01
CYL82	2.13	1.91	2.13	1.91
CYL102	2.21	1.94	2.28	1.96

Chapter 3

Conclusions and Perspectives

In this dissertation, the fabrication of HMMs with an in-plane optical axis was achieved by exploiting the BCP/homopolymer blend instability. With the aim to fabricate highly ordered BCP nanostructures as templates for hybrid metal-dielectric HMMs, the morphological stability and ordering characteristics of the self-assembled BCP lamellae was performed on PS-*b*-PMMA, either alone or blended with low-molar-mass PS and PMMA homopolymers. The morphological assessment revealed an enhancement of one order of magnitude in the correlation length of the lamellar nanodomains of the blend BCP when compared to the neat BCP. Moreover, under specific thermal annealing conditions, micrometric-sized dewetting process of relatively thick films resulted from a morphological instability of the blend BCP, leading to the formation of perfectly ordered lamellar nanostructures in a single-grain configuration within the micrometric dewetted droplets. The control over the alignment and ordering of single-grain lamellar BCP nanostructures was achieved by inducing thermally activated dewetting process of blend BCP onto topographic periodic patterns, leading to highly ordered hierarchical structures that featured substantial thickness modulation. The hierarchically ordered nanostructures were then used as effective templates for the fabrication of Au/air HMM with hyperbolic dispersion in a broad wavelength range in the Vis frequencies assisted by a pattern transfer process. The experimental assessment of the optical properties of the HMM was conducted by luminescence lifetime dynamics measurements of the NV centers inside a nanodiamond that showed a clear enhancement of the spontaneous emission up to one order of magnitude, supported by numerical modeling that indicated a strong

Purcell factor in the same spectral range of the NV centers. Finite Element Method (FEM) calculations revealed that the spontaneous emission enhancement is strongly affected by even slight changes on the nanostructures' geometrical and morphological properties and on the proper choice of the metal/dielectric materials, with direct consequences on the Purcell factor's peak position and intensity. The control over Purcell factor profile can be exploited to match the emission spectral profile of a single-photon emitter determining its amplification on a specific frequency, representing therefore one of the key advantages towards the optimization of HMMs' optical performances. The strong dependency of the material's functionality over its chemical and physical quantities requires the implementation of different characterization techniques applied to the same area, in order to gain information on the whole set of compositional and dimensional parameters of such nanostructures. In this context, a hybrid metrology approach was applied, guaranteeing the integration of multiple complementary analysis for a comprehensive material characterization to associate the material properties to the device functionalities. To this purpose, nanostructured samples that could be employed as model systems for a reliable interpretation and correlation of materials' functionality to their underpinning physical and chemical properties were fabricated by exploiting vapor and liquid chemical processes as SIS and LPI. A validation scheme, that relies on the intercomparison of results derived from different characterization techniques that aim at the same physical quantity, was developed by correlating and combining complementary techniques as GISAXS, AFM and SEM with GIXRF and NEXAFS in a hybrid metrology approach, allowing for mutual validation and more complete, reliable and coherent description of the model system. The direct comparison of the mass densities and refractive indices of the model system under study revealed good consistency among the results determined by different characterization techniques, showing low levels of mismatch from 3 to 7%.

Concerning the future perspectives, the great flexibility offered by BCP self-assembly in combination with novel synthetic processes can be further exploited for the development of more complex photonic devices, paving the way for an easy fabrication of photonic hypercrystals, hyperbolic waveguides and providing an additional degree of freedom for the fabrication of graded index elements. The geometric characteristics of the self-assembled BCP can also be adjusted to tailor the optical environment by finely tuning the fill factor of the metallic nanodomains, the thickness and morphology of the nanopattern, and to modify the spectral range through the exploitation of different metals and dielectrics.

However, for some of the described application areas, extreme control over the intrinsic properties of the nanostructures (e.g., refractive index) is required, while maintaining unaltered geometric structures at the nanoscale. These properties strongly depend on the size and shape of the nanostructures and the chemical state of the materials infiltrated inside them. To control and optimize these characteristics, it is necessary to develop hybrid metrology protocols, able to reliably put together measurements operated with very different techniques (*e.g.*, scanning probe and electron microscopies and X-ray spectroscopy techniques), representing the most complex challenge that must be quickly overcome to fully exploit the capabilities of the SIS method. The correct interpretation of the chemical/physical mechanisms and precise characterization of the SIS-processed BCPs are fundamental characteristics that must meet the basic metrological requirements while proceeding towards absolute quantitative methods and interlaboratory comparability. The substantial knowledge on the physical relationship between the techniques' measurands and the particular physical or chemical quantities of interest will allow for mutual validation of quantification schemes and support experimental and theoretical work on SIS process parameters in order to develop photonic structures and electronic devices with improved functionalities and tailorable properties through a "materials by design" approach.

Reference

1. Ferrarese Lupi, F.; Murataj, I.; Celegato, F.; Angelini, A.; Frascella, F.; Chiarcos, R.; Antonioli, D.; Gianotti, V.; Tiberto, P.; Pirri, C.F.; et al. Tailored and Guided Dewetting of Block Copolymer/Homopolymer Blends. *Macromolecules* **2020**, *53*, doi:10.1021/acs.macromol.0c01126.

2. Murataj, I.; Channab, M.; Cara, E.; Pirri, C.F.; Boarino, L.; Angelini, A.; Lupi, F.F. Hyperbolic Metamaterials via Hierarchical Block Copolymer Nanostructures. **2021**, *2001933*, 1–9, doi:10.1002/adom.202001933.

3. Meinzer, N.; Barnes, W.L.; Hooper, I.R. Plasmonic meta-atoms and metasurfaces. *Nat. Photonics* **2014**, *8*, 889–898, doi:10.1038/nphoton.2014.247.

4. Sreekanth, K.V.; Alapan, Y.; Elkabbash, M.; Ilker, E.; Hinczewski, M.; Gurkan, U.A.; De Luca, A.; Strangi, G. Extreme sensitivity biosensing platform based on hyperbolic metamaterials. *Nat. Mater.* **2016**, *15*, 621–627, doi:10.1038/nmat4609.

5. High, A.A.; Devlin, R.C.; Dibos, A.; Polking, M.; Wild, D.S.; Perczel, J.; De Leon, N.P.; Lukin, M.D.; Park, H. Visible-frequency hyperbolic metasurface. *Nature* **2015**, *522*, 192–196, doi:10.1038/nature14477.

6. Roth, D.J.; Krasavin, A. V.; Wade, A.; Dickson, W.; Murphy, A.; Kéna-Cohen, S.; Pollard, R.; Wurtz, G.A.; Richards, D.; Maier, S.A.; et al. Spontaneous Emission inside a Hyperbolic Metamaterial Waveguide. *ACS Photonics* **2017**, *4*, 2513–2521, doi:10.1021/acsphotonics.7b00767.

7. Takayama, O.; Lavrinenko, A. V. Optics with hyperbolic materials [Invited]. *J. Opt. Soc. Am. B* **2019**, *36*, F38, doi:10.1364/josab.36.000f38.

8. Poddubny, A.; Iorsh, I.; Belov, P.; Kivshar, Y. Hyperbolic metamaterials. *Nat. Photonics* **2013**, *7*, 958–967, doi:10.1038/nphoton.2013.243.

9. Smith, D.R.; Schurig, D. Electromagnetic Wave Propagation in Media with Indefinite Permittivity and Permeability Tensors. *Phys. Rev. Lett.* **2003**, *90*, 4, doi:10.1103/PhysRevLett.90.077405.

10. Ginzburg, P.; Roth, D.J.; Nasir, M.E.; Segovia, P.; Krasavin, A. V.; Levitt, J.; Hirvonen, L.M.; Wells, B.; Suhling, K.; Richards, D.; et al. Spontaneous

emission in non-local materials. *Light Sci. Appl.* **2017**, *6*, doi:10.1038/lsa.2016.273.

11. Sun, J.; Litchinitser, N.M.; Zhou, J. Indefinite by Nature: From Ultraviolet to Terahertz. *ACS Photonics* **2014**, *1*, 293–303, doi:10.1021/ph4000983.

12. Narimanov, E.E.; Kildishev, A. V. Metamaterials: Naturally hyperbolic. *Nat. Photonics* **2015**, *9*, 214–216, doi:10.1038/nphoton.2015.56.

13. Vasilantonakis, N.; Nasir, M.E.; Dickson, W.; Wurtz, G.A.; Zayats, A. V. Bulk plasmon-polaritons in hyperbolic nanorod metamaterial waveguides. *Laser Photonics Rev.* **2015**, *9*, 345–353, doi:10.1002/lpor.201400457.

14. Takayama, O.; Shkondin, E.; Bodganov, A.; Aryaee Panah, M.E.; Golenitskii, K.; Dmitriev, P.; Repän, T.; Malureanu, R.; Belov, P.; Jensen, F.; et al. Midinfrared Surface Waves on a High Aspect Ratio Nanotrench Platform. *ACS Photonics* **2017**, *4*, 2899–2907, doi:10.1021/acsphotonics.7b00924.

15. Shkondin, E.; Repän, T.; Aryaee Panah, M.E.; Lavrinenko, A. V.; Takayama, O. High Aspect Ratio Plasmonic Nanotrench Structures with Large Active Surface Area for Label-Free Mid-Infrared Molecular Absorption Sensing. *ACS Appl. Nano Mater.* **2018**, *1*, 1212–1218, doi:10.1021/acsanm.7b00381.

16. Jacob, Z.; Smolyaninov, I.I.; Narimanov, E.E. Broadband Purcell effect: Radiative decay engineering with metamaterials. *Appl. Phys. Lett.* **2012**, *100*, 22734–22746, doi:10.1063/1.4710548.

17. Shekhar, P.; Atkinson, J.; Jacob, Z. Hyperbolic metamaterials: fundamentals and applications. *Nano Converg.* **2014**, *1*, 1–17, doi:10.1186/s40580-014-0014-6.

18. Ferrari, L.; Wu, C.; Lepage, D.; Zhang, X.; Liu, Z. Hyperbolic metamaterials and their applications. *Prog. Quantum Electron.* **2015**, *40*, 1–40, doi:10.1016/j.pquantelec.2014.10.001.

19. Hoffman, A.J.; Alekseyev, L.; Howard, S.S.; Franz, K.J.; Wasserman, D.; Podolskiy, V.A.; Narimanov, E.E.; Sivco, D.L.; Gmachl, C. Negative refraction in semiconductor metamaterials. *Nat. Mater.* **2007**, *6*, 946–950, doi:10.1038/nmat2033.

20. Kabashin, A. V.; Evans, P.; Pastkovsky, S.; Hendren, W.; Wurtz, G.A.; Atkinson, R.; Pollard, R.; Podolskiy, V.A.; Zayats, A. V. Plasmonic nanorod metamaterials for biosensing. *Nat. Mater.* **2009**, *8*, 867–871,

doi:10.1038/nmat2546.

21. Jacob, Z.; Kim, J.Y.; Naik, G. V.; Boltasseva, A.; Narimanov, E.E.; Shalaev, V.M. Engineering photonic density of states using metamaterials. *Appl. Phys. B Lasers Opt.* **2010**, *100*, 215–218, doi:10.1007/s00340-010-4096-5.

22. Popov, V.; Lavrinenko, A. V.; Novitsky, A. Surface waves on multilayer hyperbolic metamaterials: Operator approach to effective medium approximation. *Phys. Rev. B* **2018**, *97*, 1–10, doi:10.1103/PhysRevB.97.125428.

23. Kidwai, O.; Zhukovsky, S. V.; Sipe, J.E. Effective-medium approach to planar multilayer hyperbolic metamaterials: Strengths and limitations. *Phys. Rev. A - At. Mol. Opt. Phys.* **2012**, *85*, 1–12, doi:10.1103/PhysRevA.85.053842.

24. Chen, W.; Thoreson, M.D.; Ishii, S.; Kildishev, A. V.; Shalaev, V.M. Ultra-thin ultra-smooth and low-loss silver films on a germanium wetting layer. *Opt. Express* **2010**, *18*, 5124, doi:10.1364/oe.18.005124.

25. Nagpal, P.; Lindquist, N.C.; Oh, S.H.; Norris, D.J. Ultrasmooth patterned metals for plasmonics and metamaterials. *Science (80-.).* **2009**, *325*, 594–597, doi:10.1126/science.1174655.

26. Liu, H.; Wang, B.; Leong, E.S.P.; Yang, P.; Zong, Y.; Si, G.; Teng, J.; Maier, S.A. Enhanced surface plasmon resonance on a smooth silver film with a seed growth layer. *ACS Nano* **2010**, *4*, 3139–3146, doi:10.1021/nn100466p.

27. Krishnamoorthy, H.N.S.; Jacob, Z.; Narimanov, E.; Kretzschmar, I.; Menon, V.M. Topological transitions in metamaterials. *Opt. InfoBase Conf. Pap.* **2012**, 205–210.

28. Avrutsky, I.; Salakhutdinov, I.; Elser, J.; Podolskiy, V. Highly confined optical modes in nanoscale metal-dielectric multilayers. *Phys. Rev. B - Condens. Matter Mater. Phys.* **2007**, *75*, 2–5, doi:10.1103/PhysRevB.75.241402.

29. Lu, D.; Liu, Z. Hyperlenses and metalenses for far-field super-resolution imaging. *Nat. Commun.* **2012**, *3*, 1–9, doi:10.1038/ncomms2176.

30. Adams, D.C.; Inampudi, S.; Ribaudo, T.; Slocum, D.; Vangala, S.; Kuhta, N.A.; Goodhue, W.D.; Podolskiy, V.A.; Wasserman, D. Funneling light through a subwavelength aperture with epsilon-near-zero materials. *Phys.*

Rev. Lett. **2011**, *107*, 1090–1099, doi:10.1103/PhysRevLett.107.133901.

31. Naik, G. V.; Saha, B.; Liu, J.; Saber, S.M.; Stach, E.A.; Irudayaraj, J.M.K.; Sands, T.D.; Shalaev, V.M.; Boltasseva, A. Epitaxial superlattices with titanium nitride as a plasmonic component for optical hyperbolic metamaterials. *Proc. Natl. Acad. Sci. U. S. A.* **2014**, *111*, 7546–7551, doi:10.1073/pnas.1319446111.

32. Santiago, K.C.; Mundle, R.; White, C.; Bahoura, M.; Pradhan, A.K. Infrared metamaterial by RF magnetron sputtered ZnO/Al:ZnO multilayers. *AIP Adv.* **2018**, *8*, doi:10.1063/1.5024900.

33. Iorsh, I. V.; Mukhin, I.S.; Shadrivov, I. V.; Belov, P.A.; Kivshar, Y.S. Hyperbolic metamaterials based on multilayer graphene structures. *Phys. Rev. B - Condens. Matter Mater. Phys.* **2013**, *87*, doi:10.1103/PhysRevB.87.075416.

34. Pollard, R.J.; Murphy, A.; Hendren, W.R.; Evans, P.R.; Atkinson, R.; Wurtz, G.A.; Zayats, A. V.; Podolskiy, V.A. Optical nonlocalities and additional waves in epsilon-near-zero metamaterials. *Phys. Rev. Lett.* **2009**, *102*, 1–4, doi:10.1103/PhysRevLett.102.127405.

35. Guo, P.; Chang, R.P.H.; Schaller, R.D. Tunable infrared hyperbolic metamaterials with periodic indium-tin-oxide nanorods. *Appl. Phys. Lett.* **2017**, *111*, doi:10.1063/1.4993426.

36. Riley, C.T.; Smalley, J.S.T.; Post, K.W.; Basov, D.N.; Fainman, Y.; Wang, D.; Liu, Z.; Sirbuly, D.J. High-Quality, Ultraconformal Aluminum-Doped Zinc Oxide Nanoplasmonic and Hyperbolic Metamaterials. *Small* **2016**, *12*, 892–901, doi:10.1002/smll.201501797.

37. Lounis, B.; Orrit, M. Single-photon sources. *Reports Prog. Phys.* **2005**, *68*, 1129–1179, doi:10.1088/0034-4885/68/5/R04.

38. Huo, P.; Zhang, S.; Liang, Y.; Lu, Y.; Xu, T. Hyperbolic Metamaterials and Metasurfaces: Fundamentals and Applications. *Adv. Opt. Mater.* **2019**, *7*, 1–25, doi:10.1002/adom.201801616.

39. O'Brien, J.L.; Furusawa, A.; Vučković, J. Photonic quantum technologies. *Nat. Photonics* **2009**, *3*, 687–695, doi:10.1038/nphoton.2009.229.

40. Shen, L.; Lin, X.; Shalaginov, M.Y.; Low, T.; Zhang, X.; Zhang, B.; Chen, H. Broadband enhancement of on-chip single-photon extraction via tilted hyperbolic metamaterials. *Appl. Phys. Rev.* **2020**, *7*, doi:10.1063/1.5141275.

41. Whitesides, G.M.; Boncheva, M. Beyond molecules: Self-assembly of mesoscopic and macroscopic components. *Proc. Natl. Acad. Sci. U. S. A.* **2002**, *99*, 4769–4774, doi:10.1073/pnas.082065899.

42. Whitesides, G.M.; Grzybowski, B. Self-assembly at all scales. *Science (80-.).* **2002**, *295*, 2418–2421, doi:10.1126/science.1070821.

43. De La Olvera Cruz, M. Theory of microphase separation in block copolymer solutions. *J. Chem. Phys.* **1989**, *90*, 1995–2002, doi:10.1063/1.456042.

44. Epstein, I.R. Chemical Approach. **1992**, *89*, 3977–3979.

45. Förster, S.; Konrad, M. From self-organizing polymers to nano- and biomaterials. *J. Mater. Chem.* **2003**, *13*, 2671–2688, doi:10.1039/b307512p.

46. Fredrickson, G.H.; Helfand, E. Fluctuation effects in the theory of microphase separation in block copolymers. *J. Chem. Phys.* **1987**, *87*, 697–705, doi:10.1063/1.453566.

47. Lo, T.Y.; Chao, C.C.; Ho, R.M.; Georgopanos, P.; Avgeropoulos, A.; Thomas, E.L. Phase transitions of polystyrene-b-poly(dimethylsiloxane) in solvents of varying selectivity. *Macromolecules* **2013**, *46*, 7513–7524, doi:10.1021/ma4013863.

48. Kim, J.K.; Yang, S.Y.; Lee, Y.; Kim, Y. Functional nanomaterials based on block copolymer self-assembly. *Prog. Polym. Sci.* **2010**, *35*, 1325–1349, doi:10.1016/j.progpolymsci.2010.06.002.

49. Perego, M.; Seguini, G. Self-assembly strategies for the synthesis of functional nanostructured materials. *Riv. del Nuovo Cim.* **2016**, *39*, 279–312, doi:10.1393/ncr/i2016-10124-4.

50. Bates, F.S.; Fredrickson, G.H. Block copolymer thermodynamics: Theory and experiment. *Annu. Rev. Phys. Chem.* **1990**, *41*, 525–557, doi:10.1146/annurev.pc.41.100190.002521.

51. Simon, P.F.W.; Ulrich, R.; Spiess, H.W.; Wiesner, U. Block copolymer-ceramic hybrid materials from organically modified ceramic precursors. *Chem. Mater.* **2001**, *13*, 3464–3486, doi:10.1021/cm0110674.

52. Matsen, M.W.; Schick, M. Stable and unstable phases of a diblock copolymer melt. *Phys. Rev. Lett.* **1994**, *72*, 2660–2663, doi:10.1103/PhysRevLett.72.2660.

53. Schick, M. in Starblock Copolymer Melts. **1994**, *98195*, 6761–6767.

54. Winey, K.I.; Thomas, E.L.; Fetters, L.J. Ordered morphologies in binary blends of diblock copolymer and homopolymer and characterization of their intermaterial dividing surfaces. *J. Chem. Phys.* **1991**, *95*, 9367–9375, doi:10.1063/1.461164.

55. Ferrarese Lupi, F.; Giammaria, T.J.; Seguini, G.; Vita, F.; Francescangeli, O.; Sparnacci, K.; Antonioli, D.; Gianotti, V.; Laus, M.; Perego, M. Fine tuning of lithographic masks through thin films of PS-b -PMMA with different molar mass by rapid thermal processing. *ACS Appl. Mater. Interfaces* **2014**, *6*, 7180–7188, doi:10.1021/am5003074.

56. Ruiz, R.; Kang, H.; Detcheverry, F.A.; Dobisz, E.; Kercher, D.S.; Albrecht, T.R.; De Pablo, J.J.; Nealey, P.F. Density multiplication and improved lithography by directed block copolymer assembly. *Science (80-.).* **2008**, *321*, 936–939, doi:10.1126/science.1157626.

57. Kim, E.; Kim, W.; Lee, K.H.; Ross, C.A.; Son, J.G. A top coat with solvent annealing enables perpendicular orientation of sub-10 nm microdomains in Si-containing block copolymer thin films. *Adv. Funct. Mater.* **2014**, *24*, 6981–6988, doi:10.1002/adfm.201401678.

58. Tsai, H.; Pitera, J.W.; Miyazoe, H.; Bangsaruntip, S.; Engelmann, S.U.; Liu, C.C.; Cheng, J.Y.; Bucchignano, J.J.; Klaus, D.P.; Joseph, E.A.; et al. Two-dimensional pattern formation using graphoepitaxy of PS-b-PMMA block copolymers for advanced FinFET device and circuit fabrication. *ACS Nano* **2014**, *8*, 5227–5232, doi:10.1021/nn501300b.

59. Liu, C.C.; Han, E.; Onses, M.S.; Thode, C.J.; Ji, S.; Gopalan, P.; Nealey, P.F. Fabrication of lithographically defined chemically patterned polymer brushes and mats. *Macromolecules* **2011**, *44*, 1876–1885, doi:10.1021/ma102856t.

60. Gu, W.; Hong, S.W.; Russell, T.P. Orienting block copolymer microdomains with block copolymer brushes. *ACS Nano* **2012**, *6*, 10250–10257, doi:10.1021/nn304049w.

61. Black, C.T. Polymer self-assembly as a novel extension to optical lithography. *ACS Nano* **2007**, *1*, 147–150, doi:10.1021/nn7002663.

62. Fontana, S.M.; Dadmun, M.D.; Lowndes, D.H. Long-range order of cylinders in diblock copolymer thin films using graphoepitaxy. *Thin Solid Films* **2010**, *518*, 2783–2792, doi:10.1016/j.tsf.2009.10.161.

63. Gianotti, V.; Antonioli, D.; Sparnacci, K.; Laus, M.; Giammaria, T.J.; Ferrarese Lupi, F.; Seguini, G.; Perego, M. On the thermal stability of PS-b-PMMA block and P(S-r-MMA) random copolymers for nanopatterning applications. *Macromolecules* **2013**, *46*, 8224–8234, doi:10.1021/ma401023y.

64. Borah, D.; Rasappa, S.; Senthamaraikannan, R.; Shaw, M.T.; Holmes, J.D.; Morris, M.A. The sensitivity of random polymer brush-lamellar polystyrene-b-polymethylmethacrylate block copolymer systems to process conditions. *J. Colloid Interface Sci.* **2013**, *393*, 192–202, doi:10.1016/j.jcis.2012.10.070.

65. Stoykovich, M.P.; Müller, M.; Kim, S.O.; Solak, H.H.; Edwards, E.W.; De Pablo, J.J.; Nealey, P.F. Materials Science: Directed assembly of block copolymer blends into nonregular device-oriented structures. *Science (80-.).* **2005**, *308*, 1442–1446, doi:10.1126/science.1111041.

66. Farrell, R.A.; Fitzgerald, T.G.; Borah, D.; Holmes, J.D.; Morris, M.A. *Chemical interactions and their role in the microphase separation of block copolymer thin films*; 2009; Vol. 10; ISBN 3532142740.

67. Harrison, C.; Chaikin, P.M.; Huse, D.A.; Register, R.A.; Adamson, D.H.; Daniel, A.; Huang, E.; Mansky, P.; Russell, T.P.; Hawker, C.J.; et al. Reducing substrate pinning of block copolymer microdomains with a buffer layer of polymer brushes. *Macromolecules* **2000**, *33*, 857–865, doi:10.1021/ma991551g.

68. Yokojima, Y.; Shiwa, Y. Hydrodynamic interactions in ordering process of two-dimensional quenched block copolymers. *Phys. Rev. E - Stat. Physics, Plasmas, Fluids, Relat. Interdiscip. Top.* **2002**, *65*, 11, doi:10.1103/PhysRevE.65.056308.

69. Harrison, C.; Angelescu, D.E.; Trawick, M.; Cheng, Z.; Huse, D.A.; Chaikin, P.M.; Vega, D.A.; Sebastian, J.M.; Register, R.A.; Adamson, D.H. Pattern coarsening in a 2D hexagonal system. *Europhys. Lett.* **2004**, *67*, 800–806, doi:10.1209/epl/i2004-10126-5.

70. Vega, D.A.; Harrison, C.K.; Angelescu, D.E.; Trawick, M.L.; Huse, D.A.; Chaikin, P.M.; Register, R.A. Ordering mechanisms in two-dimensional sphere-forming block copolymers. *Phys. Rev. E - Stat. Nonlinear, Soft Matter Phys.* **2005**, *71*, 1–12, doi:10.1103/PhysRevE.71.061803.

71. Zhang, X.; Sushkov, A.B.; Metting, C.J.; Fackler, S.; Drew, H.D.; Briber, R.M. Silicon patterning using self-assembled PS-b-PAA diblock copolymer masks for black silicon fabrication via plasma etching. *Plasma Process.*

Polym. **2012**, *9*, 968–974, doi:10.1002/ppap.201100198.

72. Dolan, J.A.; Wilts, B.D.; Vignolini, S.; Baumberg, J.J.; Steiner, U.; Wilkinson, T.D. Optical Properties of Gyroid Structured Materials: From Photonic Crystals to Metamaterials. *Adv. Opt. Mater.* **2015**, *3*, 12–32, doi:10.1002/adom.201400333.

73. Salvatore, S.; Vignolini, S.; Philpott, J.; Stefik, M.; Wiesner, U.; Baumberg, J.J.; Steiner, U. A high transmission wave-guide wire network made by self-assembly. *Nanoscale* **2015**, *7*, 1032–1036, doi:10.1039/c4nr04485a.

74. Vukovic, I.; Brinke, G. Ten; Loos, K. Block copolymer template-directed synthesis of well-ordered metallic nanostructures. *Polymer (Guildf).* **2013**, *54*, 2591–2605, doi:10.1016/j.polymer.2013.03.013.

75. Choi, S.Y.; Lee, C.; Lee, J.W.; Park, C.; Kim, S.H. Dewetting-induced hierarchical patterns in block copolymer films. *Macromolecules* **2012**, *45*, 1492–1498, doi:10.1021/ma2019655.

76. Kim, T.H.; Hwang, J.; Hwang, W.S.; Huh, J.; Kim, H.C.; Kim, S.H.; Hong, J.M.; Thomas, E.L.; Park, C. Hierarchical ordering of block copolymer nanostructures by solvent annealing combined with controlled dewetting. *Adv. Mater.* **2008**, *20*, 522–527, doi:10.1002/adma.200700651.

77. Brassat, K.; Kool, D.; Bürger, J.; Lindner, J.K.N. Hierarchical nanopores formed by block copolymer lithography on the surfaces of different materials pre-patterned by nanosphere lithography. *Nanoscale* **2018**, *10*, 10005–10017, doi:10.1039/c8nr01397g.

78. Suh, H.S.; Kim, D.H.; Moni, P.; Xiong, S.; Ocola, L.E.; Zaluzec, N.J.; Gleason, K.K.; Nealey, P.F. Sub-10-nm patterning via directed self-assembly of block copolymer films with a vapour-phase deposited topcoat. *Nat. Nanotechnol.* **2017**, *12*, 575–581, doi:10.1038/nnano.2017.34.

79. Park, S.; Dong, H.L.; Xu, J.; Kim, B.; Sung, W.H.; Jeong, U.; Xu, T.; Russell, T.P. Macroscopic 10-terabit-per-square-inch arrays from block copolymers with lateral order. *Science (80-.).* **2009**, *323*, 1030–1033, doi:10.1126/science.1168108.

80. Onses, M.S.; Song, C.; Williamson, L.; Sutanto, E.; Ferreira, P.M.; Alleyne, A.G.; Nealey, P.F.; Ahn, H.; Rogers, J.A. Hierarchical patterns of three-dimensional block-copolymer films formed by electrohydrodynamic jet printing and self-assembly. *Nat. Nanotechnol.* **2013**, *8*, 667–675, doi:10.1038/nnano.2013.160.

81. Kim, B.H.; Shin, D.O.; Jeong, S.J.; Koo, C.M.; Jeon, S.C.; Hwang, W.J.; Lee, S.; Lee, M.G.; Kim, S.O. Hierarchical self-assembly of block copolymers for lithography-free nanopatterning. *Adv. Mater.* **2008**, *20*, 2303–2307, doi:10.1002/adma.200702285.

82. Kim, B.H.; Lee, H.M.; Lee, J.H.; Son, S.W.; Jeong, S.J.; Lee, S.; Lee, D.I.; Kwak, S.U.; Jeong, H.; Shin, H.; et al. Spontaneous lamellar alignment in thickness-modulated block copolymer films. *Adv. Funct. Mater.* **2009**, *19*, 2584–2591, doi:10.1002/adfm.200900121.

83. Kim, B.H.; Park, S.J.; Jin, H.M.; Kim, J.Y.; Son, S.W.; Kim, M.H.; Koo, C.M.; Shin, J.; Kim, J.U.; Kim, S.O. Anomalous rapid defect annihilation in self-assembled nanopatterns by defect melting. *Nano Lett.* **2015**, *15*, 1190–1196, doi:10.1021/nl5042935.

84. Cho, A.; La, Y.; Jeoung, S.; Moon, H.R.; Ryu, J.H.; Shin, T.J.; Kim, K.T. Mix-and-Match Assembly of Block Copolymer Blends in Solution. *Macromolecules* **2017**, *50*, 3234–3243, doi:10.1021/acs.macromol.7b00438.

85. Doerk, G.S.; Yager, K.G. Rapid Ordering in “wet Brush” Block Copolymer/Homopolymer Ternary Blends. *ACS Nano* **2017**, *11*, 12326–12336, doi:10.1021/acsnano.7b06154.

86. Stoykovich, M.P.; Edwards, E.W.; Solak, H.H.; Nealey, P.F. Phase behavior of symmetric ternary block copolymer-homopolymer blends in thin films and on chemically patterned surfaces. *Phys. Rev. Lett.* **2006**, *97*, 4–7, doi:10.1103/PhysRevLett.97.147802.

87. Ferrarese Lupi, F.; Giammaria, T.J.; Ceresoli, M.; Seguini, G.; Sparnacci, K.; Antonioli, D.; Gianotti, V.; Laus, M.; Perego, M. Rapid thermal processing of self-assembling block copolymer thin films. *Nanotechnology* **2013**, *24*, doi:10.1088/0957-4484/24/31/315601.

88. Ceresoli, M.; Volpe, F.G.; Seguini, G.; Antonioli, D.; Gianotti, V.; Sparnacci, K.; Laus, M.; Perego, M. Scaling of correlation length in lamellae forming PS-b-PMMA thin films upon high temperature rapid thermal treatments. *J. Mater. Chem. C* **2015**, *3*, 8618–8624, doi:10.1039/c5tc01473e.

89. Ceresoli, M.; Ferrarese Lupi, F.; Seguini, G.; Sparnacci, K.; Gianotti, V.; Antonioli, D.; Laus, M.; Boarino, L.; Perego, M. Evolution of lateral ordering in symmetric block copolymer thin films upon rapid thermal processing. *Nanotechnology* **2014**, *25*, doi:10.1088/0957-4484/25/27/275601.

90. Ferrarese Lupi, F.; Aprile, G.; Giammaria, T.J.; Seguini, G.; Zuccheri, G.; De Leo, N.; Boarino, L.; Laus, M.; Perego, M. Thickness and Microdomain Orientation of Asymmetric PS-b-PMMA Block Copolymer Films Inside Periodic Gratings. *ACS Appl. Mater. Interfaces* **2015**, *7*, 23615–23622, doi:10.1021/acsami.5b07127.

91. Aprile, G.; Ferrarese Lupi, F.; Fretto, M.; Enrico, E.; De Leo, N.; Boarino, L.; Volpe, F.G.; Seguini, G.; Sparnacci, K.; Gianotti, V.; et al. Toward Lateral Length Standards at the Nanoscale Based on Diblock Copolymers. *ACS Appl. Mater. Interfaces* **2017**, *9*, 15685–15697, doi:10.1021/acsami.7b00509.

92. Seemann, R.; Herminghaus, S.; Jacobs, K. Dewetting patterns and molecular forces: A reconciliation. *Phys. Rev. Lett.* **2001**, *86*, 5534–5537, doi:10.1103/PhysRevLett.86.5534.

93. Limary, R.; Green, P.F. Late-stage coarsening of an unstable structured liquid film. *Phys. Rev. E - Stat. Physics, Plasmas, Fluids, Relat. Interdiscip. Top.* **2002**, *66*, 2–7, doi:10.1103/PhysRevE.66.021601.

94. Müller-Buschbaum, P.; Bauer, E.; Wunnicke, O.; Stamm, M. The control of thin film morphology by the interplay of dewetting, phase separation and microphase separation. *J. Phys. Condens. Matter* **2005**, *17*, doi:10.1088/0953-8984/17/9/006.

95. Müller-Buschbaum, P.; Stamm, M. 'Film thickness dependence of the domain size in weakly incompatible thin polymer blend films. *Colloid Polym. Sci.* **2001**, *279*, 376–381, doi:10.1007/s003960000456.

96. Ferrarese Lupi, F.; Giammaria, T.J.; Miti, A.; Zuccheri, G.; Carignano, S.; Sparnacci, K.; Seguini, G.; De Leo, N.; Boarino, L.; Perego, M.; et al. Hierarchical Order in Dewetted Block Copolymer Thin Films on Chemically Patterned Surfaces. *ACS Nano* **2018**, *12*, 7076–7085, doi:10.1021/acsnano.8b02832.

97. Mukherjee, R.; Bandyopadhyay, D.; Sharma, A. Control of morphology in pattern directed dewetting of thin polymer films. *Soft Matter* **2008**, *4*, 2086–2097, doi:10.1039/b806925e.

98. Kim, T.H.; Huh, J.; Park, C. Micropatterns of hierarchical self-assembled block copolymer droplets with solvent-assisted wetting of brush monolayers. *Macromolecules* **2010**, *43*, 5352–5357, doi:10.1021/ma1005777.

99. Schirhagl, R.; Chang, K.; Loretz, M.; Degen, C.L. Nitrogen-vacancy

centers in diamond: Nanoscale sensors for physics and biology. *Annu. Rev. Phys. Chem.* **2014**, *65*, 83–105, doi:10.1146/annurev-physchem-040513-103659.

100. Majewski, P.W.; Rahman, A.; Black, C.T.; Yager, K.G. Arbitrary lattice symmetries via block copolymer nanomeshes. *Nat. Commun.* **2015**, *6*, 1–6, doi:10.1038/ncomms8448.

101. Leniart, A.A.; Pula, P.; Sitkiewicz, A.; Majewski, P.W. Macroscopic Alignment of Block Copolymers on Silicon Substrates by Laser Annealing. *ACS Nano* **2020**, *14*, 4805–4815, doi:10.1021/acsnano.0c00696.

102. Malafronte, A.; Emendato, A.; Auriemma, F.; Sasso, C.; Laus, M.; Murataj, I.; Lupi, F.F.; De Rosa, C. Tailored inclusion of semiconductor nanoparticles in nanoporous polystyrene-block-polymethyl methacrylate thin films. *Polymer (Guildf).* **2020**, *210*, doi:10.1016/j.polymer.2020.122983.

103. Murataj, I.; Cara, E.; Baglieri, N.; Pirri, C.F.; Leo, N. De; Lupi, F.F. Liquid Phase Infiltration of Block Copolymers. **2022**.

104. Cara, E.; Murataj, I.; Milano, G.; De Leo, N.; Boarino, L.; Lupi, F.F. Recent advances in sequential infiltration synthesis (Sis) of block copolymers (bcps). *Nanomaterials* **2021**, *11*, 1–26, doi:10.3390/nano11040994.

105. Chai, J.; Wang, D.; Fan, X.; Buriak, J.M. Assembly of aligned linear metallic patterns on silicon. *Nat. Nanotechnol.* **2007**, *2*, 500–506, doi:10.1038/nnano.2007.227.

106. Liu, R.; Huang, H.; Sun, Z.; Alexander-Katz, A.; Ross, C.A. Metallic Nanomeshes Fabricated by Multimechanism Directed Self-Assembly. *ACS Nano* **2021**, *15*, 16266–16276, doi:10.1021/acsnano.1c05315.

107. Haridas, M.; Basu, J.K. Controlled photoluminescence from self-assembled semiconductor-metal quantum dot hybrid array films. *Nanotechnology* **2010**, *21*, doi:10.1088/0957-4484/21/41/415202.

108. Alvarez-Fernandez, A.; Aissou, K.; Pécastaings, G.; Hadziioannou, G.; Fleury, G.; Ponsinet, V. High refractive index in low metal content nanoplasmonic surfaces from self-assembled block copolymer thin films. *Nanoscale Adv.* **2019**, *1*, 849–857, doi:10.1039/c8na00239h.

109. Shin, D.O.; Mun, J.H.; Hwang, G.T.; Yoon, J.M.; Kim, J.Y.; Yun, J.M.; Yang, Y.B.; Oh, Y.; Lee, J.Y.; Shin, J.; et al. Multicomponent nanopatterns

by directed block copolymer self-assembly. *ACS Nano* **2013**, *7*, 8899–8907, doi:10.1021/nn403379k.

110. Hill, G.T.; Lee, D.T.; Williams, P.S.; Needham, C.D.; Dandley, E.C.; Oldham, C.J.; Parsons, G.N. Insight on the Sequential Vapor Infiltration Mechanisms of Trimethylaluminum with Poly(methyl methacrylate), Poly(vinylpyrrolidone), and Poly(acrylic acid). *J. Phys. Chem. C* **2019**, *123*, 16146–16152, doi:10.1021/acs.jpcc.9b02153.

111. McGuinness, E.K.; Leng, C.Z.; Losego, M.D. Increased Chemical Stability of Vapor-Phase Infiltrated AlO x –Poly(methyl methacrylate) Hybrid Materials . *ACS Appl. Polym. Mater.* **2020**, *2*, 1335–1344, doi:10.1021/acsapm.9b01207.

112. Subramanian, A.; Doerk, G.; Kisslinger, K.; Yi, D.H.; Grubbs, R.B.; Nam, C.Y. Three-dimensional electroactive ZnO nanomesh directly derived from hierarchically self-assembled block copolymer thin films. *Nanoscale* **2019**, *11*, 9533–9546, doi:10.1039/c9nr00206e.

113. McGuinness, E.K.; Zhang, F.; Ma, Y.; Lively, R.P.; Losego, M.D. Vapor Phase Infiltration of Metal Oxides into Nanoporous Polymers for Organic Solvent Separation Membranes. *Chem. Mater.* **2019**, *31*, 5509–5518, doi:10.1021/acs.chemmater.9b01141.

114. Subramanian, A.; Doerk, G.; Kisslinger, K.; Yi, D.H.; Grubbs, R.B.; Nam, C.Y. Three-dimensional electroactive ZnO nanomesh directly derived from hierarchically self-assembled block copolymer thin films. *Nanoscale* **2019**, *11*, 9533–9546, doi:10.1039/c9nr00206e.

115. Biswas, M.; Libera, J.A.; Darling, S.B.; Elam, J.W. New insight into the mechanism of sequential infiltration synthesis from infrared spectroscopy. *Chem. Mater.* **2014**, *26*, 6135–6141, doi:10.1021/cm502427q.

116. Wan, Z.; Lee, H.J.; Kim, H.G.; Jo, G.C.; Park, W.I.; Ryu, S.W.; Lee, H.B.R.; Kwon, S.H. Circular Double-Patterning Lithography Using a Block Copolymer Template and Atomic Layer Deposition. *Adv. Mater. Interfaces* **2018**, *5*, 1–9, doi:10.1002/admi.201800054.

117. He, X.; Waldman, R.Z.; Mandia, D.J.; Jeon, N.; Zaluzec, N.J.; Borkiewicz, O.J.; Ruett, U.; Darling, S.B.; Martinson, A.B.F.; Tiede, D.M. Resolving the Atomic Structure of Sequential Infiltration Synthesis Derived Inorganic Clusters. *ACS Nano* **2020**, acsnano.0c03848, doi:10.1021/acsnano.0c03848.

118. Azoulay, R.; Shomrat, N.; Weisbord, I.; Atiya, G.; Segal-Peretz, T. Metal Oxide Heterostructure Array via Spatially Controlled–Growth within Block

Copolymer Templates. *Small* **2019**, *15*, 1–7, doi:10.1002/smll.201904657.

119. Lorenzoni, M.; Evangelio, L.; Fernández-Regúlez, M.; Nicolet, C.; Navarro, C.; Pérez-Murano, F. Sequential Infiltration of Self-Assembled Block Copolymers: A Study by Atomic Force Microscopy. *J. Phys. Chem. C* **2017**, *121*, 3078–3086, doi:10.1021/acs.jpcc.6b11233.

120. Crouzier, L.; Delvallée, A.; Ducourtieux, S.; Devoille, L.; Noircler, G.; Ulysse, C.; Taché, O.; Barruet, E.; Tromas, C.; Feltin, N. Development of a new hybrid approach combining AFM and SEM for the nanoparticle dimensional metrology. *Beilstein J. Nanotechnol.* **2019**, *10*, 1523–1536, doi:10.3762/bjnano.10.150.

121. Beckhoff, B. Traceable Characterization of Nanomaterials by X-ray Spectrometry Using Calibrated Instrumentation. *Nanomaterials* **2022**, *12*, doi:10.3390/nano12132255.

122. Wernecke, J.; Gollwitzer, C.; Müller, P.; Krumrey, M. Characterization of an in-vacuum PILATUS 1M detector. *J. Synchrotron Radiat.* **2014**, *21*, 529–536, doi:10.1107/S160057751400294X.

123. Scholze, F.; Haase, A.; Krumrey, M.; Soltwisch, V.; Wernecke, J. Investigation of Nanostructures Surfaces by Scattering Procedures. *PTB-Mitteilungen* **2014**, *124*, 48–52.

124. Müller, M.; Hönicke, P.; Detlefs, B.; Fleischmann, C. Characterization of high-k nanolayers by grazing incidence X-ray spectrometry. *Materials (Basel).* **2014**, *7*, 3147–3159, doi:10.3390/ma7043147.

125. Kolbe, M.; Hönicke, P. Fundamental parameters of Zr and Ti for a reliable quantitative X-ray fluorescence analysis. *X-Ray Spectrom.* **2015**, *44*, 217–220, doi:10.1002/xrs.2603.

126. Fernandez-Regu Lez, M.; Solano, E.; Evangelio, L.; Gottlieb, S.; Pinto-Gomez, C.; Rius, G.; Fraxedas, J.; Gutierrez-Fernandez, E.; Nogales, A.; Garcia-Gutierrez, M.C.; et al. Self-assembly of block copolymers under nonisothermal annealing conditions as revealed by grazing-incidence small-angle X-ray scattering. *J. Synchrotron Radiat.* **2020**, *27*, 1278–1288, doi:10.1107/S1600577520009820.

127. Sides, S.W.; Fredrickson, G.H. Continuous polydispersity in a self-consistent field theory for diblock copolymers. *J. Chem. Phys.* **2004**, *121*, 4974–4986, doi:10.1063/1.1776557.

128. Lynd, N.A.; Meuler, A.J.; Hillmyer, M.A. Polydispersity and block

copolymer self-assembly. *Prog. Polym. Sci.* **2008**, *33*, 875–893, doi:10.1016/j.progpolymsci.2008.07.003.

129. Wernecke, J.; Krumrey, M.; Hoell, A.; Kline, R.J.; Liu, H.K.; Wu, W.L. Traceable GISAXS measurements for pitch determination of a 25 nm self-assembled polymer grating. *J. Appl. Crystallogr.* **2014**, *47*, 1912–1920, doi:10.1107/S1600576714021050.

130. BIPM; IEC; IFCC; ILAC; ISO; IUPAC; IUPAP; OIML GUM modeling: Guide to the expression of uncertainty in measurement - Part 6: Developing and using measurement models. **2020**, *JCGM GUM-6*, 1–103.

131. Doerk, G.S.; Li, R.; Fukuto, M.; Rodriguez, A.; Yager, K.G. Thickness-Dependent Ordering Kinetics in Cylindrical Block Copolymer/Homopolymer Ternary Blends. *Macromolecules* **2018**, *51*, 10259–10270, doi:10.1021/acs.macromol.8b01773.

132. Soltwisch, V.; Fernández Herrero, A.; Pflüger, M.; Haase, A.; Probst, J.; Laubis, C.; Krumrey, M.; Scholze, F. Reconstructing detailed line profiles of lamellar gratings from GISAXS patterns with a Maxwell solver. *J. Appl. Crystallogr.* **2017**, *50*, 1524–1532, doi:10.1107/S1600576717012742.

133. Müller, M.; Gerlach, M.; Holfelder, I.; Hönicke, P.; Lubeck, J.; Nutsch, A.; Pollakowski, B.; Streeck, C.; Unterumsberger, R.; Weser, J.; et al. X-ray spectrometry with synchrotron radiation. *PTB - Mitteilungen Forschen und Prufen* **2014**, *124*, 17–23.

134. Kucheyev, S.O.; Van Buuren, T.; Baumann, T.F.; Satcher, J.H.; Willey, T.M.; Meulenberg, R.W.; Felter, T.E.; Poco, J.F.; Gammon, S.A.; Terminello, L.J. Electronic structure of titania aerogels from soft x-ray absorption spectroscopy. *Phys. Rev. B - Condens. Matter Mater. Phys.* **2004**, *69*, 1–7, doi:10.1103/PhysRevB.69.245102.

135. Hönicke, P.; Detlefs, B.; Nolot, E.; Kayser, Y.; Mühle, U.; Pollakowski, B.; Beckhoff, B. Reference-free grazing incidence x-ray fluorescence and reflectometry as a methodology for independent validation of x-ray reflectometry on ultrathin layer stacks and a depth-dependent characterization. *J. Vac. Sci. Technol. A* **2019**, *37*, 041502, doi:10.1116/1.5094891.

136. Hönicke, P.; Kayser, Y.; Nikolaev, K. V.; Soltwisch, V.; Scheerder, J.E.; Fleischmann, C.; Siefke, T.; Andrle, A.; Gwalt, G.; Siewert, F.; et al. Simultaneous Dimensional and Analytical Characterization of Ordered Nanostructures. *Small* **2021**, *2105776*, doi:10.1002/smll.202105776.

137. Kayser, Y.; Osán, J.; Hönicke, P.; Beckhoff, B. Reliable compositional analysis of airborne particulate matter beyond the quantification limits of total reflection X-ray fluorescence. *Anal. Chim. Acta* **2022**, *1192*, doi:10.1016/j.aca.2021.339367.

138. Caligiore, F.E.; Nazzari, D.; Cianci, E.; Sparnacci, K.; Laus, M.; Perego, M.; Seguini, G. Effect of the Density of Reactive Sites in P(S-r-MMA) Film during Al2O3 Growth by Sequential Infiltration Synthesis. *Adv. Mater. Interfaces* **2019**, *6*, 1–10, doi:10.1002/admi.201900503.

139. Andrle, A.; Hönicke, P.; Gwalt, G.; Schneider, P.I.; Kayser, Y.; Siewert, F.; Soltwisch, V. Shape-and element-sensitive reconstruction of periodic nanostructures with grazing incidence x-ray fluorescence analysis and machine learning. *Nanomaterials* **2021**, *11*, 1–15, doi:10.3390/nano11071647.

140. Joubert, O.; Fiori, C.; Oberlin, J.C.; Paniez, P.; Pelletier, J.; Pons, M.; Vachette, T.; Weill, A. Resist degradation under plasma exposure: Synergistic effects of ion bombardment. *J. Appl. Phys.* **1991**, *69*, 1697–1702, doi:10.1063/1.347214.

141. Bès, A.; Koo, M.; Phan, T.L.; Lacoste, A.; Pelletier, J. Oxygen plasma etching of hydrocarbon-like polymers: Part I Modeling. *Plasma Process. Polym.* **2018**, *15*, doi:10.1002/ppap.201800038.

142. Ottermann, C.R.; Bange, K. Correlation between the density of TiO2 films and their properties. *Thin Solid Films* **1996**, *286*, 32–34, doi:10.1016/S0040-6090(96)08848-7.

143. Bendavid, A.; Martin, P.J. Review of thin film materials deposition by the filtered cathodic vacuum arc process at CSIRO. *J. Aust. Ceram. Soc.* **2014**, *50*, 86–101.

144. Niilisk, A.; Moppel, M.; Pärs, M.; Sildos, I.; Jantson, T.; Avarmaa, T.; Jaaniso, R.; Aarik, J. Structural study of TiO2 thin films by micro-Raman spectroscopy. *Cent. Eur. J. Phys.* **2006**, *4*, 105–116, doi:10.1007/s11534-005-0009-3.

145. Busani, T.; Devine, R.A.B. Dielectric and infrared properties of TiO2 films containing anatase and rutile. *Semicond. Sci. Technol.* **2005**, *20*, 870–875, doi:10.1088/0268-1242/20/8/043.

146. Anderson, O.; Ottermann, C.R.; Kuschnereit, R.; Hess, P.; Bange, K. Density and Young's modulus of thin TiO2 films. *Fresenius. J. Anal. Chem.* **1997**, *358*, 315–318, doi:10.1007/s002160050416.